TECHNISCHE UNIVERSITÄT MÜNCHEN
Max-Planck-Institut für Quantenoptik

Distribution of quantum information between an atom and two photons

Bernhard Weber

Vollständiger Abdruck der von der Fakultät für Physik der Technischen Universität München zur Erlangung des akademischen Grades eines

Doktors der Naturwissenschaften (Dr. rer. nat.)

genehmigten Dissertation.

Vorsitzender:		Univ.-Prof. Dr. W. Zwerger
Prüfer der Dissertation:	1.	Hon.-Prof. Dr. G. Rempe
	2.	Univ.-Prof. J. J. Finley, Ph.D.

Die Dissertation wurde am 30.09.2008 bei der Technischen Universität München eingereicht und durch die Fakultät für Physik am 03.11.2008 angenommen.

Abstract

The construction of networks consisting of optically interconnected processing units is a promising way to scale up quantum information processing systems. To store quantum information, single trapped atoms are among the most proven candidates. By placing them in high finesse optical resonators, a bidirectional information exchange between the atoms and photons becomes possible with, in principle, unit efficiency. Such an interface between stationary and flying qubits constitutes a possible node of a future quantum network.

The results presented in this thesis demonstrate the prospects of a quantum interface consisting of a single atom trapped within the mode of a high-finesse optical cavity. In a two-step process, we distribute entanglement between the stored atom and two subsequently emitted single photons. The long atom trapping times achieved in the system together with the high photon collection efficiency of the cavity make the applied protocol in principle deterministic, allowing for the creation of an entangled state at the push of a button. Running the protocol on this quasi-stationary quantum interface, the internal state of the atom is entangled with the polarization state of a single emitted photon. The entanglement is generated by driving a vacuum-stimulated Raman adiabatic passage between states of the coupled atom-cavity system. In a second process, the atomic part of the entangled state is mapped onto a second emitted photon using a similar technique and resulting in a polarization-entangled two-photon state. To verify and characterize the photon-photon entanglement, we measured a violation of a Bell inequality and performed a full quantum state tomography. The results prove the prior atom-photon entanglement and demonstrate a quantum information transfer between the atom and the two emitted photons. This reflects the advantages of a high-finesse cavity as a quantum interface in future quantum networks.

Kurzfassung

Ein vielversprechender Ansatz zur Skalierung von Systemen zur Quanteninformationsverarbeitung besteht in der Konstruktion von Netzwerken aus optisch miteinander verbundenen Prozessoreinheiten. Bezüglich der Speicherung von Quanteninformation gehören einzelne, in Fallen gefangene Atome zu den bisher bestuntersuchten Kandidaten. Positioniert man sie in optischen Resonatoren hoher Finesse, so ermöglicht dies im Prinzip einen vollständigen bidirektionalen Informationsaustausch zwischen Atomen und Photonen. Eine derartige Schnittstelle zwischen stationären und fliegenden Quanten-Bits stellt einen denkbaren Knoten eines zukünftigen Quantennetzwerks dar.

Die in dieser Dissertation vorgestellten Ergebnisse demonstrieren die Möglichkeiten einer solchen Quantenschnittstelle, bestehend aus einem optischen Resonator und einem darin gespeicherten einzelnen Atom. In einem zweistufigen Prozess wird ein im System erzeugter verschränkter Zustand zwischen dem stationären Atom und zwei nacheinander emittierten Photonen verteilt. Die in unserem System erreichten langen Speicherzeiten für das Atom und die hohe Effizienz, mit der der Resonator die emittierten Photonen sammelt, machen das verwendete Verschränkungsprotokoll im Prinzip deterministisch. Dies ermöglicht die Erzeugung verschränkter Zustände auf Knopfdruck. Angewandt auf unsere quasi-stationäre Quantenschnittstelle wird zunächst mittels eines vakuum-stimulierten, adiabatischen Ramantransfers der interne atomare Zustand mit der Polarisation eines einzelnen emittierten Photons verschränkt. Ein zweiter derartiger Prozess überträgt den atomaren Teil des erzeugten Zustands auf ein zweites emittiertes Photon und man erhält einen polarisations-verschränkten Zwei-Photonen-Zustand.
Um die Verschränkung nachzuweisen und zu charakterisieren, wurde sowohl die Verletzung einer Bell-Ungleichung gemessen, als auch eine vollständige Zustandstomographie durchgeführt. Die Ergebnisse dieser Messungen sind nur über eine vorangehende Atom-Photon Verschränkung erklärbar und demonstrieren damit einen erfolgreichen Quanten-Informationstransfer zwischen dem Atom und den zwei emittierten Photonen. Dies reflektiert die Vorteile des optischen Resonators als Quanten-Schnittstelle in zukünftigen Quantennetzwerken.

Contents

1 Introduction

In the context of quantum information processing, networks of local stationary processing units exchanging information via optical connections are one of the top issues of interest. A basic requirement of such a network is a quantum interface allowing highly efficient conversion from stationary to mobile qubits and vice versa. The results presented in this thesis constitute a demonstration of a prototype of such an interface. They show a distribution of entanglement between a stationary and two flying qubits.

There has been a lot of progress over the past decades producing "engineered" entangled states. Experiments with photons from atomic radiative cascades were among the first to study the properties of such states [1; 2]. Together with later experiments using parametric down-conversion techniques [3; 4], they could provide important tests of non-locality in quantum mechanics [5] with the violation of Bell inequalities [6]. Feynman and Deutsch came up with ideas, that it might be possible to carry out certain computations or quantum simulations efficiently using quantum systems [7; 8; 9]. Based on these ideas, and with the proposal of quantum algorithms by Shor [10] and Grover [11], research on the realization of quantum computers became of widespread interest. Knill, Laflamme and Milburn presented a scheme for all-optical quantum computing with single photons [12], stimulating a series of experiments on creating entangled photon states [13; 14; 15] and photonic quantum gates [16; 17; 18]. Quantum computation with photons can obviously be very fast and even quantum memories for photonic states were successfully demonstrated using atomic ensembles [19]. The major drawback of computation with linear optics lies in the difficulty of scaling it to larger systems as this requires immense numbers of deterministically created single photons.

Focusing on stationary qubits, one finds that ions and neutral atoms are among the most proven candidates for quantum computing to date. While neutral atoms in optical dipole traps or lattices [20; 21; 22] show promise for scalable computation units, currently, the most advanced systems for deterministic entanglement are using trapped ions. About ten years ago, the first quantum gates between two trapped ions were implemented [23; 24; 25; 26]. More recent experiments have shown that atomic systems can also provide coherence times up to 20 seconds for entangled states [27; 28]. In electric traps, chains of single ions can deterministically be entangled using common motional excitation modes [29; 30]. The group of Blatt in Innsbruck demonstrated a fully addressable quantum-byte consisting of eight single-ion qubits [28]. However, the extension to even more qubits is limited by the increasingly time-consuming tomography of the states. To scale up these systems, one attempt currently pursued is to have an extended array of ion traps implemented on a chip [31; 32; 33]. Such trap arrays consist of separated processing units and data storage parts. Like in a conventional computer, the ion qubits are brought from the memory section to the processing unit and back whenever they are needed. While there has been recent progress concerning the basic requirements of this kind of architecture [34; 35; 36], problems arise with the rather time-consuming transport between the individual sections

of the trap and the challenge of preserving coherence of the ions [37; 38].

A fast and direct link between local processing units with a series of atomic qubits could be provided via the exchange of photons [39]. First experiments demonstrating this possibility produced bipartite entanglement between an ion or atom and a single photon emitted into free space [40; 41; 42]. With two identical traps separated by one meter, two ions were remotely entangled using single photons [43]. The creation of such states naturally has to be probabilistic, as only a fraction of the emitted photons can be collected and detected. A realistic scenario for distributed quantum information processing however requires an efficient [44] interface between stationary and flying qubits. A high-finesse cavity could constitute such a mediating element [45]. At this point, neutral atoms can play out their advantages. Without the need of electric fields for trapping, they can be placed in, and strongly coupled to cavities with very small mode volume. The power of cavity quantum-electrodynamics (CQED) was demonstrated in an impressive series of experiments with such systems. For instance, cavities were used as single-atom detectors [46], for cooling atoms in a trap [47; 48; 49; 50], the realization of single-photon sources [51; 52] and to create entangled states [53]. A single atom strongly coupled to a cavity, makes it not only possible to deterministically create single photons with almost unit efficiency [52], but also allows to control every property of the emitted photon. While this is obvious for its emission direction, one can additionally define the emission frequency [54], shape its wave-packet using STIRAP techniques or fast excitations in combination with a cavity detuning [55]. Other CQED experiments demonstrated a source of single photons with alternating polarization [53], and a single-atom laser [56].

All these results are evidence for the versatility of atom-cavity systems. But even though first experiments with ions in a cavity successfully have also shown application as a single-photon source [57], it is difficult to position dielectric mirrors close enough to ions in an electric trap to achieve strong coupling. Neutral atom experiments, on the other hand, suffered for a long time from short trapping and interaction times. At this point, our experiment entered the arena. With our apparatus, we were able to position and store single atoms in a cavity for several ten seconds [58]. By now, this has also been achieved by other groups [59; 60]. The long interaction times then let us take the single-photon source with neutral atoms to a new level. We were able to verify the sub-Poissonian statistics of the emitted light within a fraction of the atom trapping time [61].

The new results published in this thesis present the apparatus as a near-permanent quantum interface. They successfully demonstrate a quantum information transfer between a single atom trapped within the cavity and two emitted photons. In two subsequent steps, the atom is first entangled with the polarization of a single photon, and later, the atomic part of the atom-photon entanglement is mapped onto a second photon. This results in a polarization-entangled two-photon state. The applied protocol is intrinsically deterministic and reversible. In principle, it allows for the creation of entanglement at the push of a button [62]. The created entanglement is verified by measuring the polarization state of the two photons. The results show a clear violation of a Bell inequality. To reveal more details about the created state, an additional full quantum state tomography was performed.

In this thesis, I first introduce the apparatus and the concept of atom-cavity coupling (chapter 2). Next, I summarize the trapping and cooling mechanisms in chapter 3, which were first described in [63; 58; 48]. Chapter 4 is dedicated to the first application of our system, a single-photon server emitting streams of up to 300 000 photons with one trapped atom [61; 64]. The improvements concerning control and observation of the atom-cavity system recently achieved with a camera system is the topic of chapter 5.

The main focus of this thesis, however, is the generation of the entangled states. In chapter 6, I first introduce the applied protocol and the theoretical background of the performed measurements. Subsequent to this theoretical part, a description of the technical implementation of the scheme and the calibration of the system is given. Finally, I discuss the results obtained from the measurements on the entangled states in a detailed analysis.

2 Cold atoms in a high-finesse cavity

The major aim of our experimental setup is to amplify the interaction between single atoms and a single mode light field by means of a high-finesse optical cavity. With such a cavity one can enhance single-atom single-photon interaction such that the coupling between the two quantum objects exceeds both the decay rate of the photon field and the decay of the atomic excitation. One differentiates between "good" cavities with strong atom-photon coupling and "bad" cavities where the individual decays dominate. A system in the strong coupling regime allows, for example, quantum state mapping between atoms and photons or, in terms of quantum information processing, information transfer between a flying photon-qubit and a stationary atomic qubit. The first thing to be described in this chapter is therefore the mechanism of strong coupling between atoms and a light field. I will introduce a theoretical description based on a simple two-level atom, the *Jaynes-Cummings model* [65]. From the experimentalist's point of view, the big challenge, besides building a nice high finesse resonator, is to store exactly one atom in the cavity mode for as long as possible. In our case, this is achieved with a combination of two optical dipole-force traps. I will discuss this loading mechanism and illustrate the coupling of individual atoms to the cavity mode with typical cavity transmission data.

2.1 Atom-cavity coupling - the Jaynes-Cummings model

We consider a simple two-level atom sitting in the center of a single-mode quantized light field. In the case of our experiment, this light field would be defined as one of the modes of our optical resonator. The quantum-mechanical state is then no longer just the product of the two undisturbed states, i.e.

$$\Psi_{\mathrm{sys}} \overset{\text{i.A.}}{\neq} \Psi_{\mathrm{atom}} \otimes \Psi_{\mathrm{rad}}.$$

Rather, there will be a coupling between the two components of the system which leads to new eigenstates and eigenenergies. The theoretical model we use to analyse this coupling mechanism is commonly called the *Jaynes-Cummings model*. To get a useful Hamiltonian, we change to the interaction picture by transforming the system into a frame rotating at the frequency of the light field ω_l. We now make use of the dipole approximation and the rotating wave approximation, neglecting all terms oscillating at $2 \times \omega_l$. The Hamiltonian describing the system then reads

$$H_{\mathrm{JC}} = \hbar\omega_{\mathrm{a}}\sigma^+\sigma^- + \hbar\omega_{\mathrm{c}}a^\dagger a + \hbar g\left(a\sigma^+ + \sigma^- a^\dagger\right), \tag{2.1}$$

where $\hbar\omega_{\mathrm{a}}$ is the energy difference between the two atomic states $|g\rangle$ and $|e\rangle$, and $\sigma^+ = |e\rangle\langle g|$ and $\sigma^- = |g\rangle\langle e|$ are the pseudo-spin operators of the two-level atom. They follow the commutation-relation $[\sigma^+, \sigma^-] = \sigma_z$ with $\sigma_z = |e\rangle\langle e| - |g\rangle\langle g|$ being a measure for the excitation of the atom. The second term in equation 2.1 describes the light mode

occupation, with ω_c being the frequency of the light mode. As in this thesis we consider this to be the light field of a high finesse resonator, we add the suffix "c" already at this point. $a^\dagger$ and a are the photon creation and annihilation operators of this light field and obey the commutation-relation $\left[a, a^\dagger\right] = 1$.
The third term of equation 2.1 describes the coupling and exchange between the two parts. The coupling constant g_0 is given by the product of the light mode properties with the dipole matrix element μ_{ge} of the atomic transition:

$$g_0 = \sqrt{\frac{\omega_{\mathrm{c}}}{2\epsilon_0 V\hbar}} \cdot \mu_{\mathrm{ge}}. \tag{2.2}$$

As you can see, the main adjustable parameter for a large value for g_0 is the mode volume V. The smaller the mode volume, the larger the coupling. To get the effective coupling of an atom at a certain position within the considered light mode, we have to weigh g_0 with the mode function Ψ_{mode} such that

$$g\left(\mathbf{r}\right) = \Psi_{\mathrm{mode}}(\mathbf{r}) \cdot g_0. \tag{2.3}$$

Dressed states

When we diagonalize H_{JC}, we obtain the coupled system's eigenstates and eigenenergies. They follow out of a rotation of the original states in Hilbert space and are called *dressed states*:

$$\{|e,n\rangle, |g,n+1\rangle\} \quad \rightarrow \quad \{|+,n\rangle, |-,n\rangle\} \tag{2.4}$$

with the number of photons in the light field n and

$$\begin{aligned} |+,n\rangle &= \cos\theta_n |e,n\rangle + \sin\theta_n |g,n+1\rangle \\ |-,n\rangle &= \sin\theta_n |e,n\rangle - \cos\theta_n |g,n+1\rangle. \end{aligned}$$

The rotation angle is given by

$$\theta_n = \arctan \frac{\Omega_n}{\sqrt{\Delta^2 + \Omega_n^2} - \Delta}, \tag{2.5}$$

with $\Omega_n = 2g\sqrt{n+1}$ being the n-photon Rabi frequency and $\Delta = \omega_a - \omega_c$ the detuning between the atomic transition and frequency of the light field. The eigenenergies of the dressed states

$$E_{\pm,n} = \hbar\omega_c\left(n+1\right) - \hbar\frac{\Delta}{2} \pm \frac{\hbar}{2}\sqrt{\Delta^2 + \Omega_n^2} \tag{2.6}$$

now show an energy splitting of the doublets $\{|\pm,n\rangle\}$ by an amount of $\Delta E = \hbar\sqrt{\Delta^2 + \Omega_n^2}$. In the language of the *Jaynes-Cummings model* the energy splitting of $\Delta E(\Delta = 0) = 2\hbar g$ of the lowest doublet with photon number $n = 0$ is called the *normal-mode splitting*. We see, that due to the coupling between the atom and the light mode, the original resonance frequency is split up by an amount $\sqrt{n+1}g\left(\mathbf{r}\right)$, according to the number of photons in the light field. This is illustrated in figure 2.1.

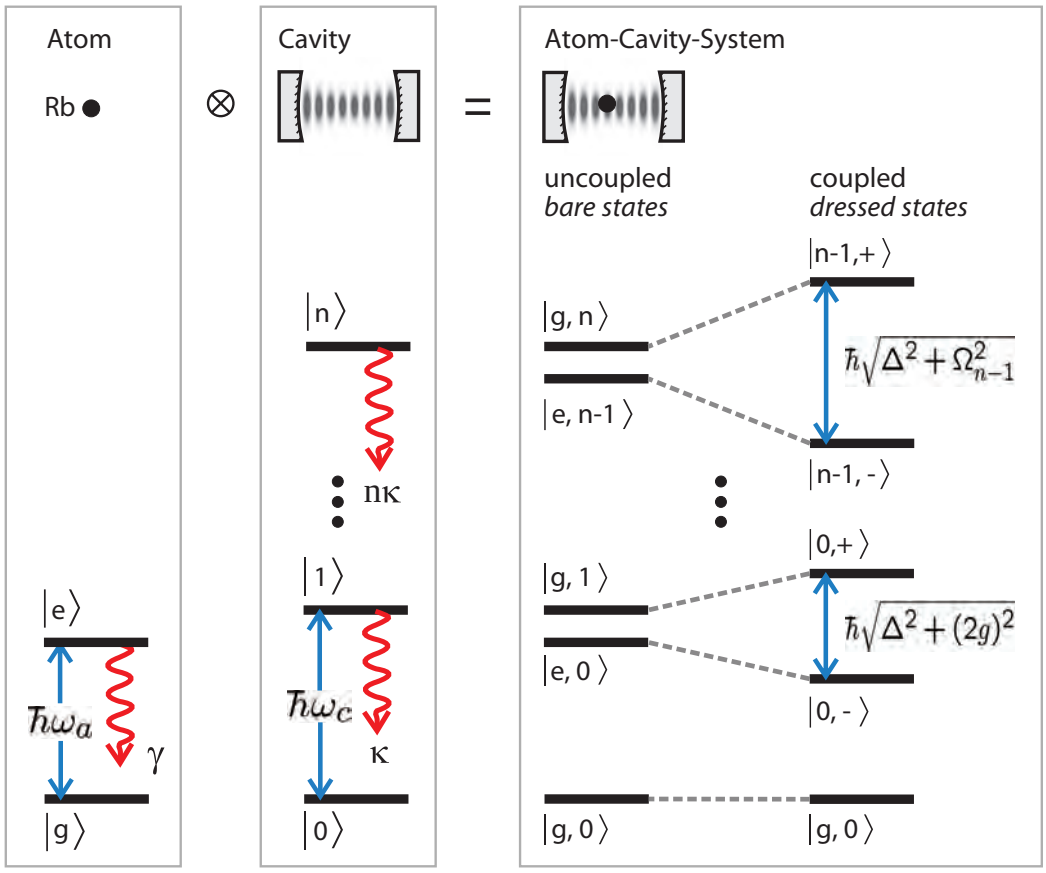

Figure 2.1: The *Jaynes-Cummings-model* describes the coupling between a quantized light field and a two-level atom. The coupled system has doublets of eigenstates with eigenenergies split up by $\Delta E = \hbar\sqrt{\Delta^2 + \Omega_n^2}$. In the experiments described in this thesis, the light field is defined by the mode of a high-finesse resonator. If the cavity resonance frequency is kept fixed, an atom coupled to the mode will shift the system's resonance with respect to the resonator.

Cooperativity, weak and strong coupling

The essential effect in cavity quantum-electrodynamics is the strong interaction between the atom and the light field. The atom-cavity coupling g has to be seen in relation to loss mechanisms in the system. In an atom-cavity system, these are the decay of the atomic excited state γ and the decay of the cavity κ as a result of mirror transmission and absorption losses. To make use of the strong interaction effects, one should aim for a system reaching the so-called *strong coupling regime* which is defined as $g \gg \gamma, \kappa$. Systems where one of the decay processes is dominating are usually said to operate in the *bad cavity limit* while systems with a dominating g are in the *good cavity limit*. The essential difference is that for a good cavity, the lifetime of a photon that the atom emits into the cavity is long enough for backactions of the photon field on the atom. Many of the theoretical proposals concerning quantum information processing with single atoms

are based on a strong coupling of the atom to a cavity. A useful parameter for judging the atom-cavity interaction strength is the so-called *cooperativity* defined as

$$C = \frac{g^2}{2\kappa\gamma} \tag{2.7}$$

For values $C < 1$ the coupling is only weak, while with values larger than 1 we reach the strong coupling regime. As you will see later in this chapter, for the cavity we use in the experiments we achieve cooperativity values of about $C = 1$, which means that we are not really strongly coupled, but in an intermediate coupling regime. This is because of our rather large κ, which was intentionally chosen such that photons emitted into the cavity get coupled out at a reasonable rate.

2.2 Working with Rubidium atoms

The atom species we use for the experiments is Rubidium. There are several good arguments for the use of this alkali atom, but the main reason is that its transition frequencies for the D-lines at 780 nm and 795 nm are easily accessible with rather cheap and simple diode-laser systems. Therefore, since the invention of laser cooling, a lot of experiments where run on Rubidium and its properties are nowadays well known. When the design of this experimental apparatus was planned, ^{85}Rb seemed to be the more attractive isotope because of the smaller hyperfine-splitting which is easier to access with standard acousto-optical modulators (AOMs). So the first experiments described in chapter 3 on trapping single atoms in the cavity and in chapter 4 about a single-atom single-photon source were performed with ^{85}Rb. For the new experiments with an atom-photon entanglement scheme it was evident that we needed a less complex level structure. As ^{87}Rb (I=3/2) has a lower nuclear spin than ^{85}Rb (I=5/2), we switched to ^{87}Rb for the entanglement measurements described in chapter 6. Both isotopes can be accessed with the same lasers.

The basic configuration of the laser setup is illustrated in figure 2.2. We use a Ti:Sa laser system (Model *MBR-110* by *Coherent*) to serve all transitions starting from the upper ground state with $F = 3$ (^{85}Rb) and $F = 2$ (^{87}Rb) respectively. The laser was originally chosen for its nice Gaussian mode profile and the narrow linewidth to set up a good stabilization for the cavity. All atomic lines starting from the lower ground state are addressed with a diode laser (*DL100* series by *Toptica*). The lasers are frequency-stabilized using the *Pound-Drever & Hall* locking technique and a Doppler-free saturation spectroscopy to obtain an error signal. In the D2-line spectroscopy, the so-called crossover lines half-way between the actual transition lines are the most pronounced, so we lock the lasers to these lines. Taking ^{87}Rb for example, we use the crossover-line between the upper $F' = 1$ and $F' = 3$ states for the Ti:Sa laser lock and the one between $F' = 1$ and $F' = 2$ for the diode laser. All transition frequencies needed for the experiments are derived from these lasers using acousto-optical modulators to shift the light exactly to the needed frequencies. The active frequency stabilization of the lasers reduces the laser linewidth to less than 100 kHz for the Ti:Sa laser and 1 MHz for the diode laser. These values are upper limits of the laser linewidths as the optics and electronics of the lock drift over the years and have to be readjusted from time to time.

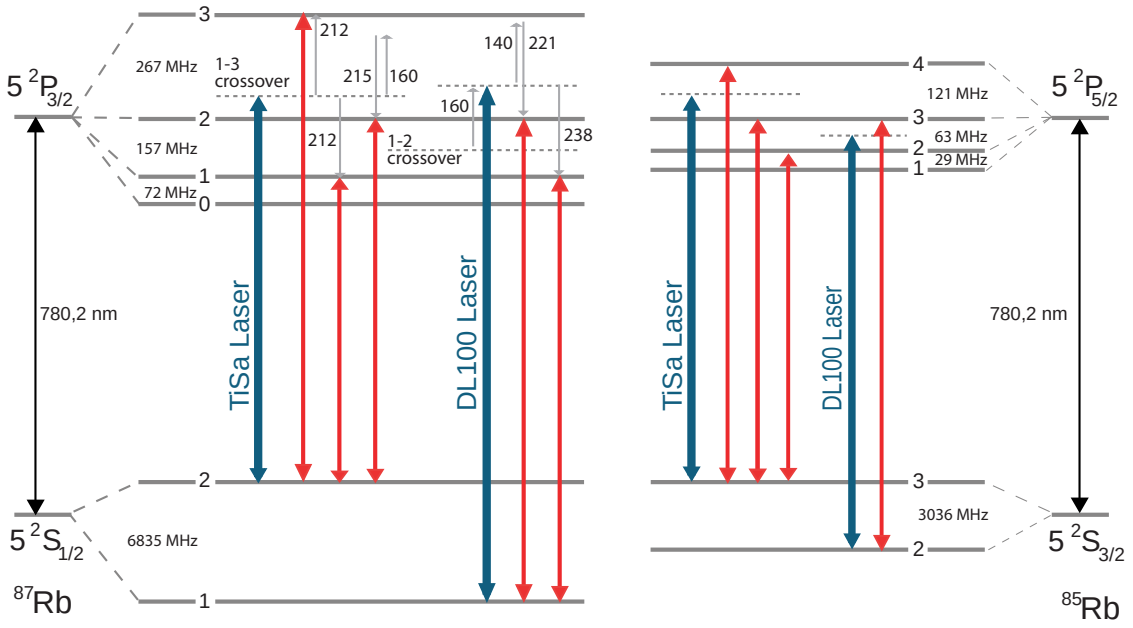

Figure 2.2: Energy-level schemes of the relevant atomic transitions used in the experiments. The left side shows the $D_2(5\,^2S_{1/2} \rightarrow 5\,^2P_{3/2})$ line of ^{87}Rb. Transitions starting from the lower F=2 level are accessed by a Ti:Sa laser system and a series of AOMs for frequency fine-tuning. The laser frequency is locked on the cross-over resonance between the upper F'=1 and F'=3 levels. A diode laser serves all atomic transitions starting from the lower F=1 level. An AOM in the stabilization light path shifts the locking frequency $2 \times 90\,\text{MHz}$ above the cross-over resonance between F=1 and F=2. The right part of the schematic shows the laser access to the $D_2(5\,^2S_{3/2} \rightarrow 5\,^2P_{5/2})$ line of ^{85}Rb respectively.

The experiment takes place in an ultra-high vacuum chamber in octagon shape, providing as many optical access ports as possible. To get atoms in the vacuum chamber, we installed a Rubidium dispenser where atoms can be heated out by applying an appropriate current. These atoms are caught by the beams of a magneto-optical trap (MOT) to Doppler-cool them to about $100 - 150\,\mu$K and collect them at the center of the MOT's quadrupole magnetic field. Details on the vacuum system, the atom dispenser and the MOT can be found in [66; 63]. These cold atoms are the starting point for all our experiments. The next step is to place them within the mode of our high-finesse cavity.

2.3 Properties of the cavity

The high-finesse optical cavity used in our experiment was designed as a compromise of different desired qualities. On the one hand, one would like to reach the strong atom-cavity coupling regime where $g \gg \gamma, \kappa$. This means the cavity mode should be as small as possible for a large coupling g and the transmission losses of the two cavity mirrors should be as low as possible to keep the photon decay κ low. On the other hand, we are interested

in a directed photon emission through one of the mirrors at a reasonably high rate. With this we can couple out the single photons produced by an atom in a controlled way. The transmission of an "outcoupling" mirror therefore has to be significantly larger than that of the other mirror, which leads, of course, to an increase of κ. Our choice was therefore a cavity with two different mirrors having transmission factors of about 100 ppm and 2 ppm respectively. With this setup, 98% of all photons should leave the cavity on the 100 ppm side where we can set up our photon detectors. For the choice of the mirror distance, a trade-off had to be made between a short cavity to obtain a large g and a sufficiently large mirror spacing to fit a high-power optical dipole trap between the mirrors. Scattering to much light on the mirror substrates would significantly heat the cavity such that its length stabilization becomes difficult. As our dipole trap was planned to have a waist of about 100 μm, we decided that a distance of half a millimeter between the mirrors should be sufficient. As the mirror surfaces are curved with a radius of 5 mm, the mirror substrates were additionally cone-shaped such that the remaining mirror diameter is just 1.5 mm. This gives a much better optical access to the cavity for perpendicular laser beams as the constrictions due to the curved mirrors are reduced. With all these parameters, we end up with a cavity with a finesse of about 60 000. This includes absorption losses of about 2 ppm for each mirror. Unfortunately, a few months after the cavity was placed in the vacuum chamber, a dust particle settled at the center of the cavity's TEM_{00} mode. This doubled the cavity's round-trip losses resulting in reduced finesse of about 30 000 for this mode. As the particle is sitting exactly in the center of the TEM_{00}, all higher modes with a central node are not affected. All important properties of the cavity are summarized in the following table.

mirror transmission	$T_1 = 1.96 \pm 0.03\,\mathrm{ppm};\ \ T_2 = (92.4 \pm 0.2)\,\mathrm{ppm}$
mirror distance	$d = 492.8 \pm 0.3\,\mu\mathrm{m}$
cavity finesse	$\mathcal{F} = 30\,000\,(\mathrm{TEM}_{00});\ 62\,200\,(\mathrm{TEM}_{01})$
free spectral range	304 GHz
total round-trip losses	$L = 6.57 \pm 0.20\,\mathrm{ppm}$
average coupling	$\overline{g}_0 = 2\pi \cdot 5.1\,\mathrm{MHz}\,(\mathrm{TEM}_{00});\ 2\pi \cdot 4.4\,\mathrm{MHz}\,(\mathrm{TEM}_{01})$
cavity decay	$\kappa = 2\pi \cdot 5.0\,\mathrm{MHz}\,(\mathrm{TEM}_{00});\ 2\pi \cdot 2.4\,\mathrm{MHz}\,(\mathrm{TEM}_{01})$

As you can see from the table, the value for the coupling g is about the same (for the TEM_{01} mode twice as high) as the cavity decay κ. If you also compare this to the natural linewidth of the D2-line of our Rubidium atoms of about 6 MHz we calculate an average cooperativity value for our system of $C = 0.9 - 1.3$, depending on the used cavity mode. This means we are at the edge of the strong coupling regime. As the cavity was assembled and tested by Felix Rohde and Stefan Nußmann, further details can be found in [67; 63].

Cavity stabilization

It is very crucial for all experiments with the cavity that the mirror distance can be very precisely fine-tuned to exactly the desired atomic transition frequency. This is achieved by mounting the two mirror substrates within a hollow piezo-crystal tube. The piezo has

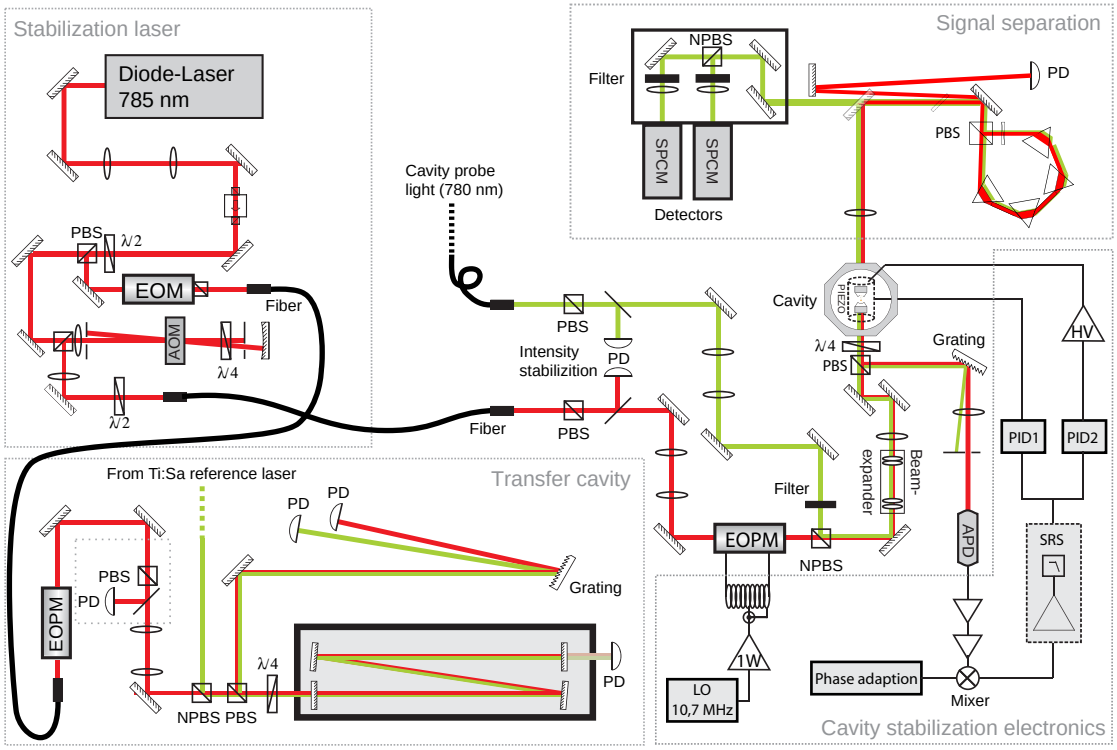

Figure 2.3: Cavity stabilization via a transfer resonator. Both the atomic transition at 780 nm and the stabilization light at 785 nm have to be simultaneously resonant with the cavity. To achieve this, two beams are derived from the stabilization laser. One is coupled into a transfer cavity which is stabilized to a Rb-line via the Ti:Sa laser. It defines a stable frequency reference with a line spacing of FSR $\approx$ 100 MHz. Locking the stabilization laser to the appropriate mode of the transfer cavity and closing the remaining frequency gap with an AOM, we can achieve the overlap of the transmission line of the second beam with that of the 780 nm probe light. Now locking the experiment cavity to the 785 nm light also ensures the probe beam to be resonant. At the output of the cavity, the two frequencies have to be separated again. After first experiments with gratings, this was done with a set of dispersive prims (as shown here), or later, for the entanglement measurements, simply with a set of spectral filters.

drilled holes at eight positions to provide the necessary optical access. By applying a control voltage of up to 150 V to the piezo, we can scan the cavity frequency by more than one free spectral range.

For the stabilization of the cavity frequency to an atomic transition, we couple laser light into the cavity at two different frequencies. The first one is, of course, a laser at 780.24 nm at or near resonant with the atomic transition. We could use this light to generate an electronic error signal to actively regulate the mirror distance for perfect transmission, but as soon as we have an atom in the cavity, we would like to switch off the laser in order to not permanently excite the atom. To solve this problem, we use a different laser for the stabilization running at about 785.24 nm. It is resonant to a cavity mode that is detuned by exactly 8 free spectral ranges from the 780.24 nm mode. To lock the

cavity to the atomic resonance, we just have to tune the 785 nm laser frequency such that the transmission lines of the two laser beams overlap perfectly. Then we lock the cavity using an error signal derived from the reflection of the 785 nm laser beam from the cavity mirror. As the stabilization light is off-resonant to the Rubidium lines, we can keep the cavity stable without exciting the atoms in the cavity mode. The stabilization laser is frequency-stabilized via a transfer resonator, which is itself locked to the stabilized Ti:Sa laser. It provides a stable comb of resonance lines with a free spectral range of ≈ 100 MHz. Therefore we can always lock the stabilization laser to it such that the remaining frequency difference to the desired experiment cavity mode is small enough to be bridged with an AOM. In other words, the cavity stabilization scheme consists of a chain of three separate stabilizations. The pretty complex optical setup for this stabilization is illustrated in figure 2.3 and a more detailed description of it can be found in [63].

A side-effect of this off-resonant light at 785 nm in the cavity is that it provides a pattern of dipole traps along the cavity axis, where atoms can be trapped in the antinodes of the standing-wave light field (see section 2.4). As the separation of the two used cavity modes is an even number of free spectral ranges, they overlap in phase in a width of about 50μm at the center of the cavity. For the experiments, we want to simultaneously store the atoms in the intra-cavity trap and have them well-coupled to the 780 nm cavity mode. We therefore need to focus our optical dipole trap within this central region. To give a better idea of the geometry and the scales of cavity mode and dipole trap, they are shown to scale in figure 2.4.

Cavity signal detection

The main data signal in the experiment is of course the light coupled out of the cavity. We are interested in recording this light on a single-photon detection level and with sub-microsecond time resolution. In our setup, for most of the experiments (except for the entanglement, see chapter 6) two single-photon counting modules (SPCM, *Perkin & Elmer*, Model *AQR-16*) were used in a *Hanbury-Brown & Twiss* configuration. This means, a 50/50 beamsplitter distributes the signal equally on the detectors, which allows for two-photon correlation measurements without detector-deadtime gap. The detectors each have a dark-click rate of less than 25 Hz and a measured quantum efficiency for light at 780 nm of about 44%. The biggest challenge in the detection is to separate the 785 nm light of the cavity stabilization from the atom signal at 785 nm. As the stabilization light is much more intense, we have to suppress its detection by a factor of $10^{10} - 10^{12}$. This can be achieved with a combination of dispersive elements for the separation and spectral and spacial filtering. Figure 2.3 shows the setup we used: the cavity light is directed through a polarizing beam cube and a set of four dispersive prisms (uncoated SF11-glass), which will spatially separate the two wavelengths by about 10 beam waists. The cube directs the two polarization components in contrary sense of rotation through the prisms and a half-wave plate adapts the polarization axis such that all light hits the prism surfaces at the Brewster's angle, which reduces reflection losses to a minimum. The two parts are recombined again and leave the system at the entrance port of the cube. To separate the output from the input, everything is aligned in a slight downward spiral. The 785 nm light

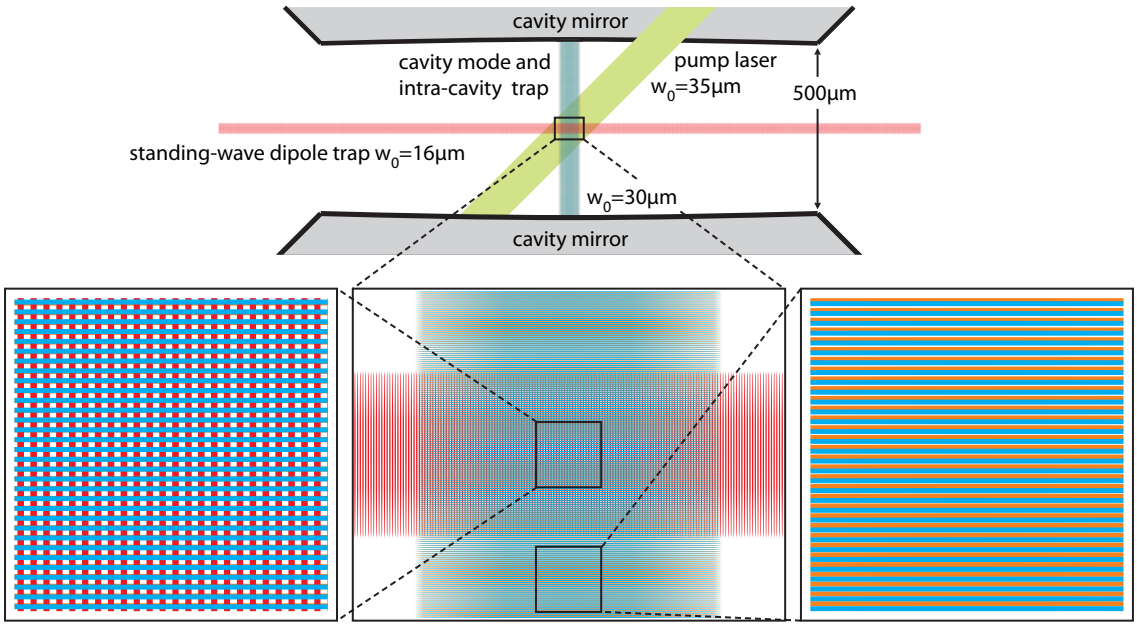

Figure 2.4: Geometry of the system. The schematic shows cavity mode and dipole trap to scale, revealing about 120 potential wells of the trap within the FWHM-width of the cavity mode. Together with the intra-cavity trap from the stabilization, we find ≈ 9000 possible trapping spots for a single atom coupled to the cavity mode. The intra-cavity trap and the 780 nm mode of the cavity have a frequency difference of 8 free spectral ranges of the cavity. Therefore, both overlap in phase in the center region (see left detail). 50 μm off the center, simultaneous trapping and coupling to the cavity is not possible as the two standing-wave structures have a relative phase shift of $\pi/2$.

can now be sent to a photodiode while the 780 nm signal passes a bandpass- and a spatial filter and is focused onto the SPCMs. With transmission factors of $T = 0.85$ for the prism setup, $T = 0.7$ for the spatial filter and $T = 0.9$ for each of the two bandpass-filters, the total signal losses from the cavity to the detectors sum up to 53%.

2.4 Trapping atoms in an optical dipole trap

To keep the atom within the mode of our cavity as long as possible, we need a trapping potential meeting two basic requirements. The first is that the potential should provide a three-dimensional confinement of the atomic motion to a volume that is small compared to the cavity mode. Second, the trap has to fit between the two mirrors of our resonator without disturbing the cavity stabilization. In our experimental approach, we make use of a high power laser with an emission line far off-resonant to the atomic transition frequencies to build a standing-wave dipole-force trap. The trapping is based on the dynamic Stark effect. The electric field $\mathbf{E}$ of the laser impinging on an atom with polarizability α induces a dipole moment in the atom $\mathbf{P} \propto \alpha\mathbf{E}$. As the atom is polarized, its potential energy

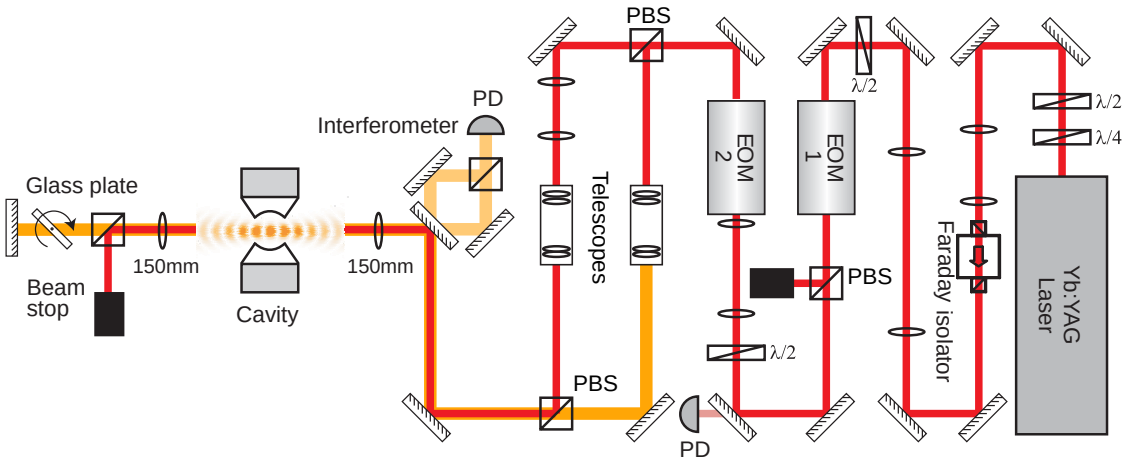

Figure 2.5: Setup for the optical dipole traps. The first EOM in the optical path is used to control the laser beam intensity. With a following second EOM allowing to switch between linear horizontal and vertical polarization, two optical paths can be chosen at the polarizing beam cube (PBS). The telescopes in these paths define the parameters of the two traps used in the experiment. Focused into the cavity and recollimated afterwards, the beam is either dumped in a beam stop or retroreflected in itself at a mirror to build the standing-wave trap.

now is depending on the field intensity $U = -\alpha|\mathbf{E}|^2$. The sign of α decides, whether this potential energy is positive or negative. For an atom in the ground state, α is positive if we address it with a red-detuned laser beam [68]. For an excited atom we get the opposite sign for α and thus also for the dipole potential $U_{\mathrm{dip}}(\mathbf{r})$. Atoms that are mainly in the ground state (meaning at low excitation rates) will therefore be attracted by high intensities and experience a force proportional to the intensity gradient:

$$\mathbf{F} = -\nabla U = 2\alpha \mathbf{E} \cdot \nabla \mathbf{E} \tag{2.8}$$

For our Rubidium atoms, two excitation lines give the major contributions to the dipole-force, the D_1-line with frequency ω_{D_1} and the D_2-line with ω_{D_2}. For linear polarized light, the dipole potential is given by [68]:

$$U_{\mathrm{dip}}(\mathbf{r}) = \frac{\pi c^2 \Gamma}{2\omega_a^3} \left(\frac{2}{\omega_s - \omega_{D_2}} + \frac{2}{\omega_s + \omega_{D_2}} + \frac{1}{\omega_s - \omega_{D_1}} + \frac{1}{\omega_s + \omega_{D_1}} \right) I(\mathbf{r}) \,, \tag{2.9}$$

with Γ being the natural linewidth of the atomic transition, ω_a the atomic transition and ω_s the trap laser frequency. While the trapping potential is $U_{\mathrm{dip}}(\mathbf{r})$, the atomic transition frequency is increased by the dynamic Stark shift $\Delta_s = 2U_{\mathrm{dip}}/\hbar$, as the excited state is also shifted by the trap light.

As the potential scales as $U_{\mathrm{dip}} \propto I/\Delta_{as}$, one would prefer small detunings $\Delta_{as} = \omega_a - \omega_s$ combined with high intensities to get a deep trapping potential. But the atom will be heated by photon scattering from the trapping laser if its frequency is too close to the atomic transition. This scattering rate scales as $R_{\mathrm{scat}} \propto I/\Delta_{as}^2$. Considering this, we find

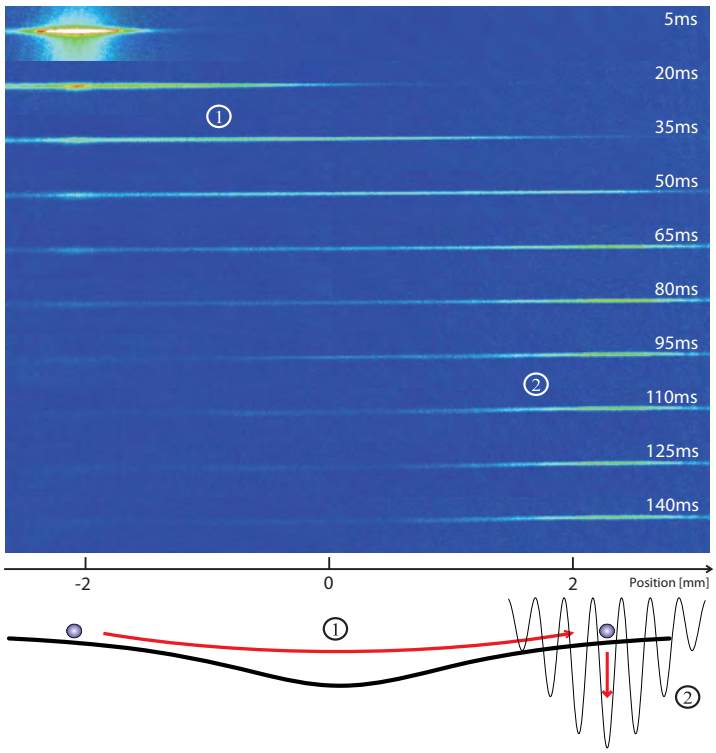

Figure 2.6: Atom transport in a dipole trap. The sequence of absorption images shows how atoms released from the MOT start oscillating in the dipole trap (1). At the time they arrive at the other turning point, switching the trap to a standing-wave configuration freezes the atom positions (2). To be able to observe this with the camera, this test measurement was performed outside the cavity over a distance of 4 mm.

that a trapping potential with a depth in the order of a few Millikelvin can be achieved with a far detuned laser with high intensity. This kind of trap is often referred to as a *far off-resonant trap*, in short *FORT*.

The traps in the experiment

In the experiment, we use a single-mode, single-frequency Yt-YAG disk laser running at a wavelength of 1030 nm, which is far off-resonant to the Rubidium D_1 and D_2 lines at 794.98 and 780.24 nm respectively. We create a standing-wave light pattern by focusing the beam into the cavity and refocusing and retroreflecting it back after passing the vacuum chamber as shown in figure 2.5. This standing wave provides three-dimensional confinement for atoms at its antinodes with a potential of about 2.5 mK when 2 W of light are used.

To transfer atoms from the MOT to the cavity, we use a second trap configuration with a simple running-wave Gaussian beam. This one is focused half-way between cavity and MOT such that the trap has equal potential energy at the MOT and cavity positions

while there is a potential minimum just in between them. The atoms thus start oscillating along the trap axis (see figure 2.6) and after half an oscillation period, at the turning point, the atoms arrive in the cavity. This is the point where we switch to the standing wave configuration to trap the atoms. As you can see in figure 2.5, we use two optical paths to create the two individual traps and we can switch between them by changing the polarization of the trap light with an electro-optical modulator (EOM). The characteristics of our dipole traps are summarized in the following table.

	transportation trap	standing-wave trap
Rayleigh length	4.6 mm	0.6 mm
focus $r(1/e^2)$	43 μm	16 μm
trap depth	188 μK @ 4 W	2.5 mK @ 2 $\times$ 2 W
Stark shift	8 MHz @ 4 W	103 MHz @ 2 $\times$ 2 W

Additional to the far off-resonant trap at 1030 nm, we have an orthogonal standing-wave potential along the cavity axis given by the stabilization laser. This laser at 785 nm produces a shallow trapping potential of $\approx 30\,\mu$K depth. The stabilization light frequency was chosen such that the distance to the 780 nm atomic transition is an even number of 8 free spectral ranges of the cavity. This ensures a perfect overlap of the trap's potential minima with the antinodes of the 780 nm mode in the center region of the cavity. Therefore the atoms are automatically well-coupled when they are trapped in the 785 nm intra-cavity potential.

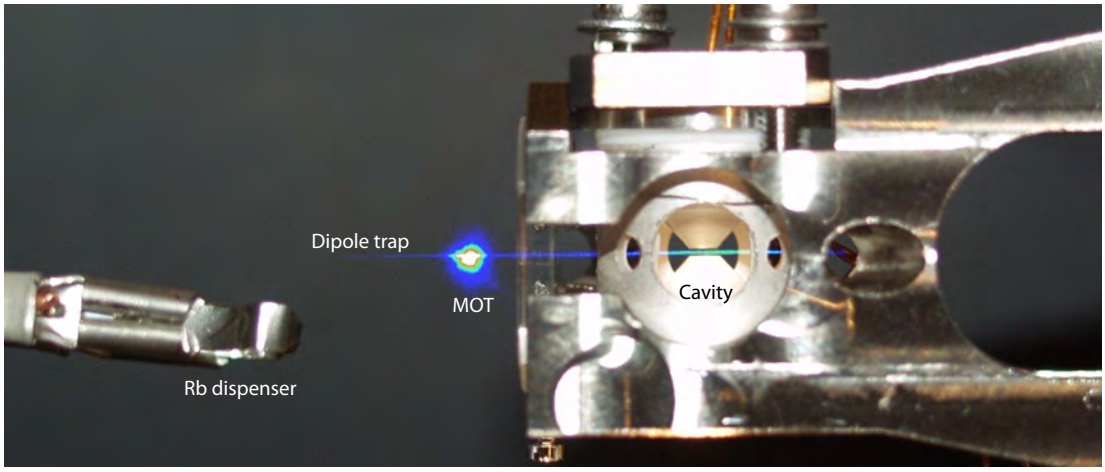

Figure 2.7: Loading atoms into the cavity. The overlay of three pictures on top illustrates how cold atoms are transported from a MOT prepared in front of a mirror into the cavity. Released from the MOT, the atoms start oscillating in a running-wave optical dipole trap, passing the mirror trough a hole. At the time they arrive in the cavity, the dipole trap is switched to a standing-wave configuration to trap the atoms there.

Loading cold atoms into the cavity

To perform our single-atom experiments in the cavity, we now combine what has been discussed in this and the previous sections to obtain a single atom loading and preparation scheme. We start our sequence heating atoms out of the dispenser while shining in the Doppler-cooling laser beams and applying the quadrupole magnetic field to load about 10^6 cold atoms into a MOT. For reasons of optical access this happens in front of the cavity holder at a distance to the cavity mode of approximately 14 mm. We now load these atoms into the transportation trap as discussed above and wait until they arrive in the center of the cavity. If we want to have the atoms trapped now, we can switch to the standing wave trap configuration. This will "freeze" the atom distribution along the trap axis and some of the atoms trapped in the standing-wave antinodes are typically right in the center of our cavity mode. Figure 2.7 illustrates this process in an overlay of three pictures: one real photograph shot through the top viewport into the vacuum chamber showing the Rubidium dispenser and the cavity-holder with the cone-shaped cavity mirrors visible in its center, one false-color absorption image of the MOT and another absorbtion-image taken when the atoms were traveling along the transportation trap. As you will see in the next chapter, we developed methods for distinguishing and selecting single atom events from those with multiple atoms such that real single-atom experiments can be performed.

2.5 Observation of atom transits in the cavity transmission

One of the first experimental results we had is a nice demonstration of the cavity's useability as a single-atom detector. It also shows the discussed normal-mode splitting induced by the atom coupling to the cavity mode. For the experiment, we couple a probe laser beam into the cavity and lock the cavity frequency such that cavity and probe light are in resonance with the atomic transition $F{=}3 \rightarrow F{=}4$, which is a closed cycling transition. The intra-cavity light field intensity is chosen to be at a level of one single photon on average. We load atoms into the MOT and transport them in our running-wave transportation trap to the cavity, where we expect them to slowly traverse the light field. The transmission through the cavity was observed using an avalanche photo diode. As soon as an atom comes in, we see a drop in the transmission signal by up to 70% in the center of the cavity mode. This can be explained by the increase of the atom-cavity coupling g causing the normal modes to split as described in section 2.1. This tunes the system out of resonance.

Figure 2.8 shows transmission signals for different transverse cavity modes (TEM_{00}, TEM_{01} and TEM_{03}). As it is flying through the mode, the atom is exactly probing the field distribution, showing one, two, and four transmission dips respectively. The fact that higher order modes can be mapped this way can also be considered as a proof that we are really detecting single atoms. For such signals a very low atom density in the trap is indispensable and so it becomes very unlikely that two atoms traverse the cavity at the same time and the same speed. From the cavity mode (TEM_{00}) width of $2 \times 30\,\mu$m and the dip width of about $500\,\mu$s one finds the atom's speed along the trap axis to be 1.2 cm/s.

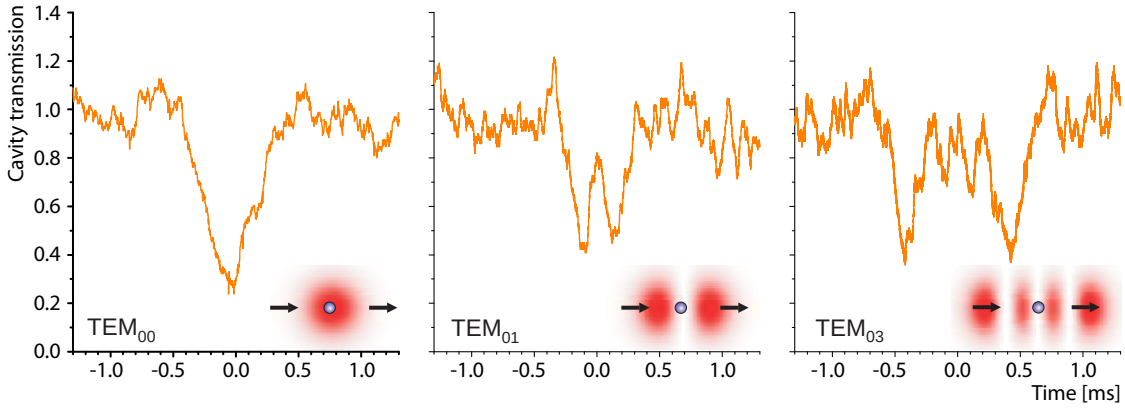

Figure 2.8: Single-atom transits through the cavity observed in the transmission signal. Single atoms in the running-wave transportation trap arrive at and pass through the cavity mode. As the coupling $g(r)$ increases we see the normal-mode splitting as a decrease in the transmitted light. The atoms can therefore probe the light field of different transversal modes of the cavity while at the same time the clearly resolved modes prove that there is only one single atom in the cavity.

3 Cooling and trapping single atoms in the cavity mode

One of the key features of our experimental setup is the possibility of trapping single atoms in an optical dipole trap within the mode of the high-finesse optical resonator. Compared to previous experiments performed in our group [69; 70; 71] where the atoms crossed the cavity mode in free fall, this has two remarkable consequences. First, we gain a high degree of control over the coupling between the atom and the cavity light field as the trap provides full three-dimensional confinement of the atom to a fraction of the cavity mode. Second, the average atom-cavity interaction time is enhanced by a large factor of up to 10^6 to several tens of seconds. This is achieved with cooling mechanisms keeping the atoms cold in the trap. The cavity Doppler-cooling forces and the Sisyphus-like cooling force described in this chapter were found while trying to catch single atoms in the dipole trap. The atoms wee adressed with a pump laser on a separate axis, perpendicular to the cavity mode and under 45 degrees to the dipole trap. We found that we can induce cooling forces on all three axes − cavity, trap and pump −, if we slightly detune the cavity resonance and pump light frequencies from each other. This results in trapping times of up to a minute. The cooling forces are only present within the intersection of the cavity mode with the pump and trap lasers. We therefore additionally obtain a method to trap atoms preferentially in the center of the cavity mode, where they are well-coupled to the cavity light field. I will now introduce the theoretical background of the cooling forces in the system and then show some experimental results on trapping single atoms inside our cavity.

3.1 Three-dimensional cavity-cooling forces

To understand the origins of the forces discovered in our system, Karim Murr developed a theoretical model based on a two-level atom interacting with the cavity which I will briefly discuss now. Readers interested in a more detailed description are referred to the original publication [49] and the PhD-Thesis of Stefan Nußmann [63].

Master equation

As in the previous chapter we consider a two-level atom placed inside the mode of a high-finesse resonator. To achieve long atom-cavity interaction times, we add our standing-wave dipole trap potential as defined in equation 2.9 and a laser beam perpendicular to the cavity-axis to excite the atom. To obtain cooling forces on the atom we need an energy-dissipating mechanism in the system. We therefore include loss mechanisms due to the atom's spontaneous emission and due to cavity decay and write up the Master equation

for our system:

$$\dot{\rho} = -\frac{i}{\hbar}[H, \rho] + \kappa \mathcal{L}_{\text{cav}}\rho + \gamma \mathcal{L}_{\text{spont}}\rho \tag{3.1}$$

with the Lindblad operators

$$\mathcal{L}_{\text{cav}}\rho = 2a\rho a^\dagger - \rho a^\dagger a - a^\dagger a\rho \tag{3.2}$$

describing the photon loss from the cavity and

$$\mathcal{L}_{\text{spont}}\rho = 2\int d^2\hat{\boldsymbol{k}} N(\hat{\boldsymbol{k}}) \mathrm{e}^{-i\boldsymbol{k}\cdot\boldsymbol{r}}|g\rangle\langle e|\rho|e\rangle\langle g|\mathrm{e}^{+i\boldsymbol{k}\cdot\boldsymbol{r}} - \rho|e\rangle\langle e| - |g\rangle\langle g|\rho \tag{3.3}$$

which integrates the atom's spontaneous emission distribution $N(\hat{\boldsymbol{k}})$ with $\hat{\boldsymbol{k}} = \boldsymbol{k}/|\boldsymbol{k}|$ over all directions.

The Hamiltonian for our model now consists of three parts, the Jaynes-Cummings part, the excitation with the pump beam and the dipole-trap potential:

$$\begin{aligned} H/\hbar = \quad & \Delta_a(\boldsymbol{r})|e\rangle\langle e| + \Delta_c\hat{a}^\dagger\hat{a} + g(\boldsymbol{r})(\hat{a}|e\rangle\langle g| + \hat{a}^\dagger|g\rangle\langle e|) \\ - \quad & \Omega(\boldsymbol{r})|e\rangle\langle g| - \Omega^*(\boldsymbol{r})|g\rangle\langle e| \\ + \quad & U(\boldsymbol{r}). \end{aligned} \tag{3.4}$$

In the first part, the first term is the product of the atomic excitation and the detuning between the atomic resonance and the pump laser, given by $\Delta_a(\boldsymbol{r}) = \omega_a - \omega_l + \Delta_s(\boldsymbol{r})$. The new component Δ_s accounts for the atomic energy-level shift coming from the AC Stark effect induced by the trap laser. The second term is the photon number in the cavity field weighted with the detuning between the cavity resonance and the excitation laser $\Delta_c = \omega_c - \omega_l$. The last term addresses the coupling between atom and cavity field. Note that all detuning definitions use the pump laser frequency as reference.

In the second part of the Hamiltonian, the excitation of the atom by the pump laser beam is expressed in terms of the Rabi frequency $2|\Omega(\boldsymbol{r})|$ and in the third part we include the dipole potential $U(\boldsymbol{r})$ from the trapping laser:

$$U(\boldsymbol{r}) = -\frac{\hbar\Gamma^2}{8\Delta_{as}}\frac{I(\boldsymbol{r})}{I_{sat}} \tag{3.5}$$

As described before, the potential mainly depends on two parameters, the trap laser intensity profile $I(\boldsymbol{r})$ and the detuning to the atom's transition line $\Delta_{at} = \omega_a - \omega_t$.

Three cavity Doppler-cooling forces

We are now interested in the time evolution of our model system and the forces acting on the trapped atoms. To find expressions for the light forces we use the Heisenberg equation of motion

$$\boldsymbol{F} = \frac{\boldsymbol{d}\hat{\boldsymbol{p}}}{\boldsymbol{dt}} = \frac{i}{\hbar}[H, \hat{\boldsymbol{p}}] = -\nabla H \tag{3.6}$$

where $\hat{\boldsymbol{p}} = -i\hbar\nabla$ is the momentum operator. To find an expression for the mean force $F = \langle \digamma \rangle$, we first calculate the steady state expectation values for the operators acting on cavity field and atom using the Master equation formalism. The atom is hereby approximated in the limit of low saturation by an harmonic oscillator. The resulting expressions are then substituted into the above equation describing the mean force. We arrive at a series of expressions for forces which act along different axes defined by the geometry of the system [49]. As we are interested in friction forces, we expand the general expressions up to the first order in the velocity. We find three expressions for dissipative forces where the detuning $\Delta_c = \omega_c - \omega_l$ between cavity and excitation laser decides whether the atom is cooled or heated. They read:

$$\boldsymbol{F}_P = -4\hbar\boldsymbol{k}_P(\boldsymbol{k}_P \cdot \boldsymbol{v})\frac{\kappa\Delta_c}{(\Delta_c^2+\kappa^2)^2}g^2 P_e \tag{3.7}$$

$$\boldsymbol{F}_C = -4\hbar\nabla g(\nabla g \cdot \boldsymbol{v})\frac{\kappa\Delta_c}{(\Delta_c^2+\kappa^2)^2}P_e \tag{3.8}$$

$$\boldsymbol{F}_S^{Cav} = -4\hbar\nabla\Delta_s(\nabla\Delta_s \cdot \boldsymbol{v})\frac{\kappa\Delta_c}{(\Delta_c^2+\kappa^2)^2}\frac{g^2 P_e}{\Delta_a^2+\gamma^2}. \tag{3.9}$$

All three expressions show the same structure with a Lorentz resonance term times the excitation probability P_e. The detuning Δ_c determines the sign of the forces. If the cavity is blue detuned to the pump laser ($\Delta_c > 0$) the friction forces will cool the atom, otherwise it will be heated. If we look at the first part of each of the expressions, we see that the direction of the individual forces points along the three main axes of our system: the pump laser axis (given by $\boldsymbol{k}_P$), the cavity axis (expressed by ∇g) and the axis along the dipole trap ($\nabla\Delta_s$). To get a better understanding of the forces let us have a look at the three illustrations in figure 3.1.

The first picture illustrates equation 3.7 describing a cooling force along the pump axis based on the Doppler effect. For an atom at rest the two driving fields of the Raman transition (cavity and pump laser) are detuned to each other by Δ_c. If the atom is now moving towards the incident laser beam, it will see the light Doppler-shifted to the blue and thus the Raman process is tuned into resonance. For an atomic motion with the propagation direction of the pump beam the Doppler effect shifts the laser frequency seen by the atom to the red and the detuning between cavity- and laser frequency is even increased. Like with the well-known Doppler-cooling used for the MOT, we here have a motion-selective scattering probability. The atom prefers a photon absorption when it is moving towards the laser beam and thus gets a momentum kick opposite to its direction of motion. Averaged over many scattering processes, the atom's momentum along the pump axis is reduced while there is no momentum change along the cavity-axis as the photon emission is balanced to both sides. The result is a cooling effect on the atom if the cavity frequency is larger than that of the pump laser. Like in a MOT, the pump laser is applied as a pair of counter-propagating beams to have the cooling force acting in both directions (for simplicity reasons, this is not shown in figure 3.1).

The second picture shows that the second force (equation 3.8) is based on the same mechanism and takes effect when the atom is moving along the cavity axis. In this case the

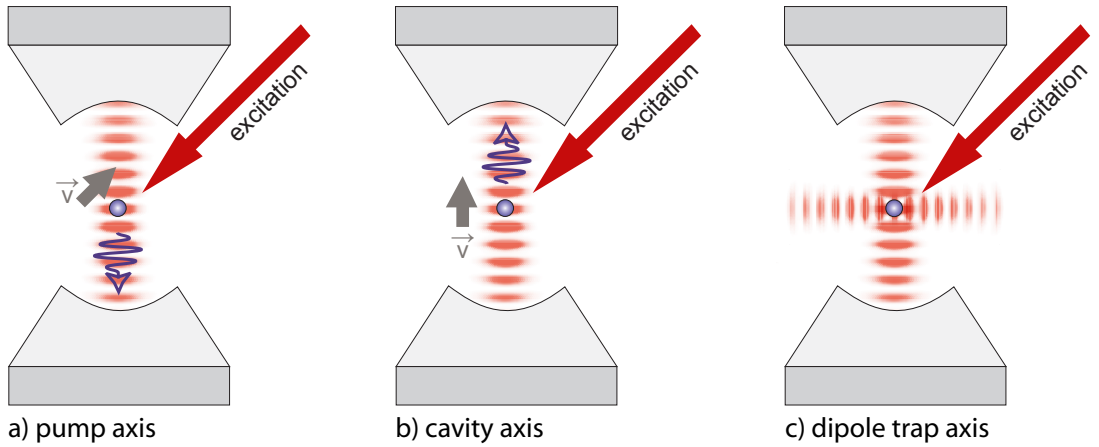

Figure 3.1: Three-dimensional cavity-cooling forces. With the cavity being blue detuned with respect to the pump laser frequency, we obtain cavity-induced Doppler-cooling forces in the system: a) An atom moving towards the pump laser will see its frequency Doppler-shifted into resonance with the cavity. Therefore we find a preferred direction of the momentum transfer in the scattering process, cooling the atom along the laser axis. b) For a movement along the cavity axis, the Doppler effect shifts the cavity frequency seen by the atom, leading to a preferred emission into the direction of motion and thus cooling the atom. c) The same type of effect cools the atom along the trap axis, based on the Stark shift gradients in the standing-wave.

Doppler effect now will cool the atom in the photon emission process into the cavity while there is no net momentum transfer from the pump laser beams, as they are a pair of balanced beams. For a blue detuned cavity, the atom will preferentially emit the photon in the direction of its motion. To understand this, we can separate the standing-wave field of the cavity into two counter-propagating modes, if we average the force over half a wavelength to eliminate the interference pattern. Now the Doppler effect will tune the pump laser into resonance with the cavity mode that is co-propagating with the atom. Thus, the photon emission occurs preferentially into the atom's direction of motion and will reduce its momentum. Again, by tuning the cavity frequency to the blue compared to the pump laser, we gain a net force which will cool the atom along the cavity axis.

The third force is not as easy to put into a simple picture as the other two. As you see in equation 3.9, the force depends on the gradient of the Stark shift which is induced in the atom by the presence of the trap. As the atom is trapped within one of the antinodes of the standing wave pattern, any atomic motion will lead to a time-varying value of the Stark shift. Thus the atom's detuning to the cavity and with it the atom-cavity coupling will fluctuate. The dissipative effect results now from the delayed adaption of the cavity light field to these fluctuations induced by the atomic motion. As the confinement by the trap is strongest along the standing-wave axis, this force mainly acts along the dipole trap beam.

Considering the configuration of our setup with the cavity axis being orthogonal to the trap and the pump lasers applied under 45 degrees, we find that the forces along these three axes add to a full three-dimensional cooling mechanism. The discovery of this mechanism

turned out to be the basis of all following experiments with long trapping times. The theoretical model also contains an additional fourth cooling force acting in our system, which is independent of the cavity and can thus be used even when cavity cooling is not applicable for an experiment.

3.2 Another cooling force: a Sisyphus-like mechanism

If we remove the cavity from our system, we are left with an atom in the standing wave trap driven by the pump laser on one of its transitions. When we tune the pump laser to the unperturbed atomic resonance, a cold atom sitting on the bottom of one of the antinodes of the standing-wave pattern will experience a large Stark shift $\Delta_s(\boldsymbol{r})$ and thus be off-resonant to the pump laser. A hot, but yet trapped atom is able to move close to the standing-wave nodes where it is close to resonance with the excitation laser. Hot atoms will therefore be excited preferentially when they are at the turning point of their intra-trap oscillation. The emission process takes place a little later when the atom is on average closer to the antinode again and therefore the Stark-shifted transition frequency is a little larger now. This means that in the whole process, kinetic energy of the atom is transferred into a higher frequency of the emitted photon. The mathematical description of this fourth cooling force looks very similar to the cavity cooling forces from above, but with a Lorentz resonance defined by Δ_a and γ:

$$\boldsymbol{F}_S^{Sis} = -4\hbar\nabla\Delta_s(\nabla\Delta_s\cdot\boldsymbol{v})\frac{\Delta_a}{2\gamma(\Delta_a^2+\gamma^2)}P_e^2. \tag{3.10}$$

The background of this force is essentially that of Sisyphus cooling with a blue detuned

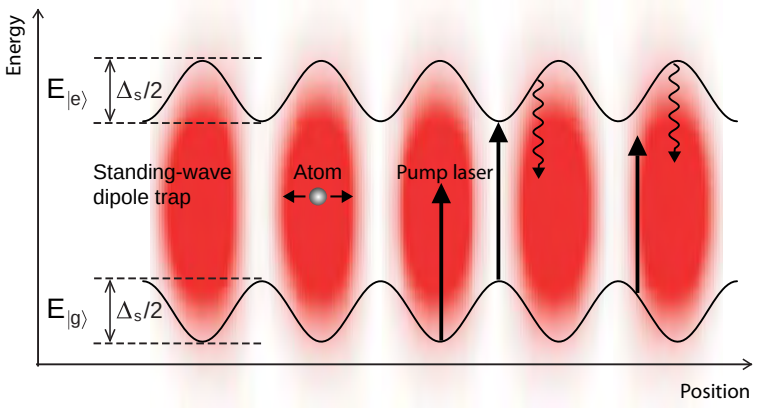

Figure 3.2: Sisyphus-like cooling mechanism. The standing-wave trap periodically modulates the atomic transition frequency along the trap axis. With the excitation laser tuned to the unshifted resonance (the minimum transition frequency), the probability to actually drive the transition depends on the atom's temperature and position in the trap. It is preferentially excited to the potential minimum of the upper state. Any movement of the atom will cost potential energy before the spontaneous decay to the ground state occurs. The atom is cooled corresponding to the energy difference between excitation and decay process.

laser [72; 73], with the difference that now trapping and optical pumping is done by two separate lasers. The analogy to Sisyphus rolling the stone up the hill becomes clear, when we look at the illustration in figure 3.2. If we draw the Stark shift between ground state and excited state along the standing-wave pattern of the trap, the atom is preferentially excited into one of the "valleys" of the excited state. It then has to "roll uphill" before it falls down to the ground state again and the cycle starts over. This cooling force is extremely useful in our experiment as it allows for trapping times on the order of $10-20\,\mathrm{s}$. Compared to cavity Doppler-cooling, the strengths of the two forces are on the same scale. I will document this with experimental results later in this chapter.

3.3 Trapping of single atoms using a closed transition

We discovered the cooling forces in our system with our early attempts to trap a single atom in the cavity. The original plan was to trigger on a cavity transmission breakdown when an atom coming along in the transportation trap enters the cavity mode. Right with the trigger event, we wanted to switch on the standing wave to get the atom trapped before it leaves the cavity again. This did not really work for two reasons. First, to trap the atom, one needs to ramp up the standing-wave trap power adiabatically, otherwise the atom will not stay cold in the trap. In the experiment, this meant that trapping an atom required a power ramp duration longer than the atom transit time of $0.5\,\mathrm{ms}$ and in the end we eventually had a trapped atom nearby, but not within the cavity. The second reason was that when we had a trapped atom, we were not able to probe its presence using the transmission signal anymore, because the large AC Stark shift of about $100\,\mathrm{MHz}$ induced by the trap tuned the atom out of resonance with the cavity. This was the point when we installed an excitation laser beam orthogonal the the cavity axis and started looking for atom emission signals.

First signals

The idea was to drive Raman-type transitions in the system using a pump laser as one part of the process while the cavity replaces the usual second laser. This process works even if the shared upper level of the two transitions is not resonant with an atomic excited state. To start with, we chose the ${}^2S_{3/2}, F{=}3 \rightarrow 5\,{}^2P_{5/2}, F'{=}4$ transition of ${}^{85}\mathrm{Rb}$ for the pump laser as well as for the cavity frequency. As we do not compensate for level shifts in the atom caused by the trap, the upper energy level of the Raman transition should be detuned from the excited state of the trapped atom by the amount of the AC Stark shift. The choice of a closed transition keeps the system cycling between two states and so it constantly emits photons into the cavity. For the case the atom is lost in the lower $F{=}2$ state, we apply an additional repumping laser on $F{=}2 \rightarrow F{=}3$. Typical signals of our first trapping events are reproduced in figure 3.3. Having switched to the standing-wave trap configuration after the atom transport, we apply the two counter-propagating excitation lasers. They have orthogonal linear polarization to avoid spatial interference patterns in the pump light and to address all π- and σ transitions. As the standing-wave

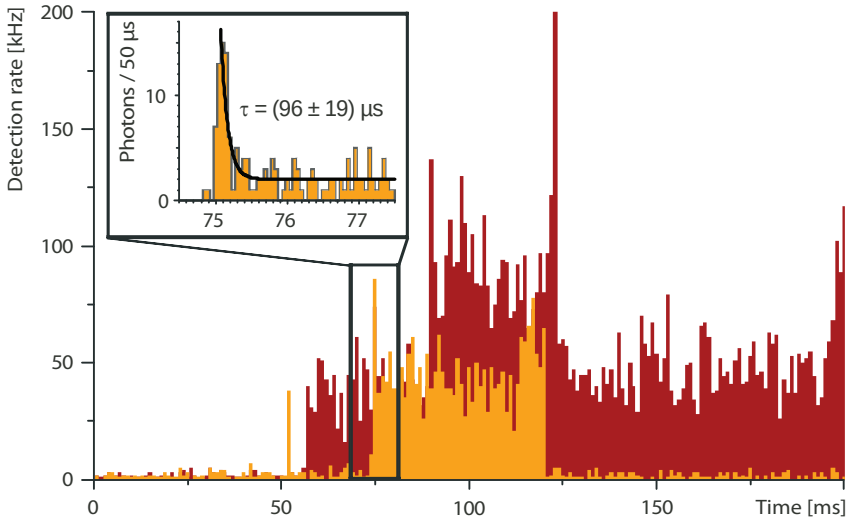

Figure 3.3: First trapping events. On these first signals with the atoms being addressed with a pump laser orthogonal to the cavity axis, spikes at the beginning and the end of the trapping period reveal details on the cooling and heating processes leading to a capture in, or loss from the trap. The typical timescale seems to be $\approx 0.1\,\mathrm{ms}$.

is just switched on, we expect a number of atoms with enough kinetic energy to hop along the trap's node pattern. As soon as they arrive at the intersection of pump laser an cavity mode, the photon scattering process starts and we get a signal at the photon detectors watching the cavity output. So when an atom gets trapped, we see a sudden rise in the detected photon number to a level characteristic to a single atom. As long as there is no change in the atoms position, temperature in the trap and coupling to the cavity, the signal stays constant. We soon found, that the trapping works best when the cavity is detuned a few megahertz to the blue compared to the pump laser frequency, just as discussed in the theoretical model above (see section 3.1). If we look at the details of such a trapping event, we see that it often starts with a high photon scattering rate which is rapidly decaying down to the steady-state value. This can be interpreted as the cooling process. In our system, the scattering rate decreases with rising detuning of the upper energy level of our Raman transition from the real atomic excited state. As the AC Stark shift detunes the atom more and more when it is cooled down into the trap, we get a drop in the detected scattering signal. Looking at the zoom-in of figure 3.3, we can fit an exponential decay with $\tau \approx 0.1\,\mathrm{ms}$ to the signal. This seems to be the timescale on which the cooling and trapping process takes place. With the same type of signature, we can see that the atoms in the shown traces are heated up and show an increasing scattering rate before getting lost from the trap. The mechanisms that produce this type of atom loss are not well understood, it might be mode hops of the trapping laser or intensity fluctuations in the pump lasers beams.

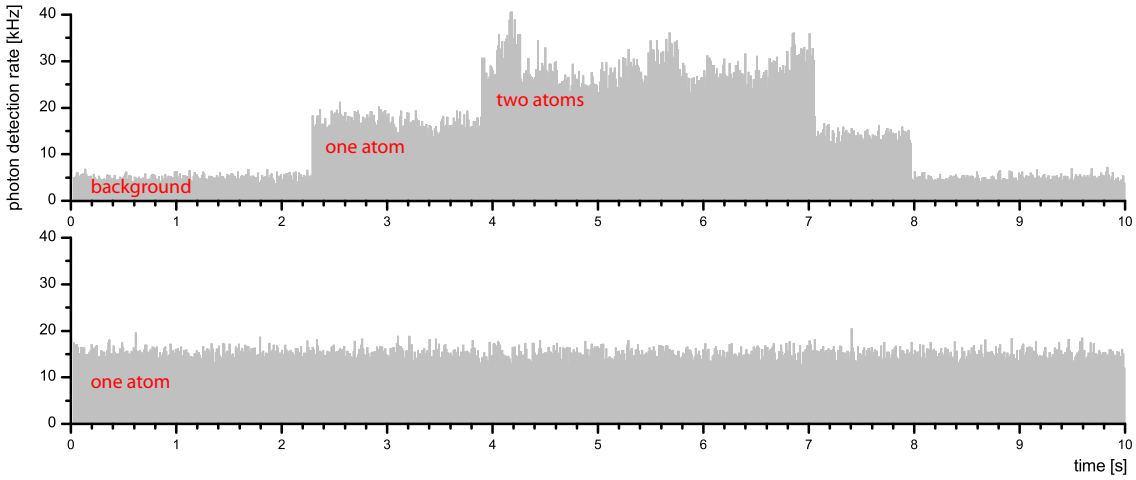

Figure 3.4: Example trapping events. The signal detected at the output of the cavity typically shows a constant scattering rate characteristic for one trapped atom, indicating a constant coupling to the cavity on timescales > 1 ms. Sudden steps in the signal occur when an additional atom gets trapped via the cooling forces or one is lost from the trap.

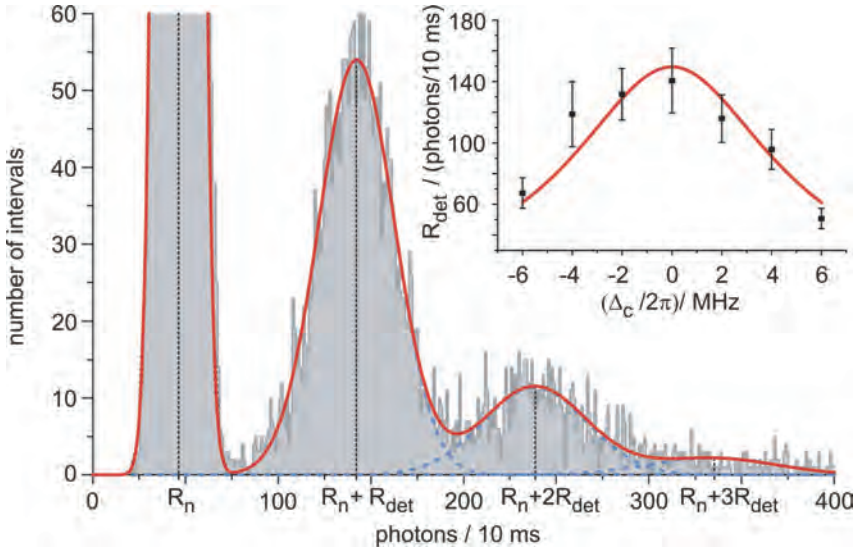

Figure 3.5: Characteristic cavity signals. Binning the detected photon signal of the cavity on a timescale of 10 ms reveals several peaks attribute to characteristic count rates for different atom numbers. The peaks are explained by adding N times the detection rate for a single atom R_{det} to the background count rate for an empty cavity R_n, with N being the number of trapped atoms. We can clearly resolve zero-, one- and two-atom events from the photon detection rate.

Characteristic signal steps in the cavity output

Fine-tuning of the alignment of the standing-wave trap, the pump laser positions and the light-pressure balance makes it possible to increase the lifetime of the atoms in the trap up to several seconds. This made it possible to start with detailed systematic parameter scans and signal analysis. Figure 3.4 gives examples of such traces of trapped atoms. It shows that the signal level of two trapped atoms is roughly twice the signal of a single atom. Furthermore, an atom loss from the trap typically shows a sudden step in the signal level. The visibility of these steps indicates, that most of the atoms are trapped within a small region of the cavity mode such that they all have almost the same coupling to the cavity mode. If we analyze the relative frequencies of the photon numbers per bin, we can plot the histogram shown in figure 3.5. This analysis of the data of several hundred experimental runs like the ones of figure 3.4 shows that the distribution of the photon number per 10 ms time-bin has several clearly separated maxima. The first (cut off at the top) represents the background signal level of (at the time this data was taken) about 4.5 kHz. The second peak is the signal of a single trapped atom which gives an additional 10 kHz count rate. Adding another atom with an additional 10 kHz gives peak number three. From now on the different couplings of the individual atoms start to wash out the steps in the signal and the maxima for 3 and more atoms are hardly visible. Nevertheless, by just looking at the photon detection rate, the system allows to distinguish between no atom, one, two and many atoms trapped in the cavity. This is possible within only 10 ms at a high success rate of estimated 90%.

Atom lifetimes in the trap

To get an idea of the efficiency of the cooling forces we compared the atom storage times with and without application of the pump laser. First, the lifetime in the trap without any cooling was measured using two short pump laser intervals to probe the presence of the atom and a variable dark period between them. For each trapping time we measured the probability to still find the atom trapped. An exponential decay fit gave a lifetime of 2.7 s. This lifetime is mainly ruled by fluctuations of the trap laser. Even though there is an optical isolator in the beam, the retroreflection of the beam to create the standing-wave couples a small fraction of the light back into the laser resonator. This causes intensity fluctuations of the laser output. When we built in a second isolator, the lifetime increased to about 5 s. To determine the lifetime in the trap with applied pump lights, we took a set of traces with 6 s of recorded signal each and evaluated it with a software looking for matching one-atom signals level and a falling edge when the atom gets lost from the trap. We can then fit an exponential decay to the plot of the number of remaining atoms versus trapping time, as shown in figure 3.6. For a setting with $\Delta_c = \omega_c - \omega_l = 0$ MHz the only active cooling force is the Sisyphus-like force and the lifetime turned out to be 17 s, which means an extension by more than a factor of six.

As it is not completely convincing when the measured lifetimes are longer than the measurement interval, we thought of a way to artificially reduce the lifetime in a controlled

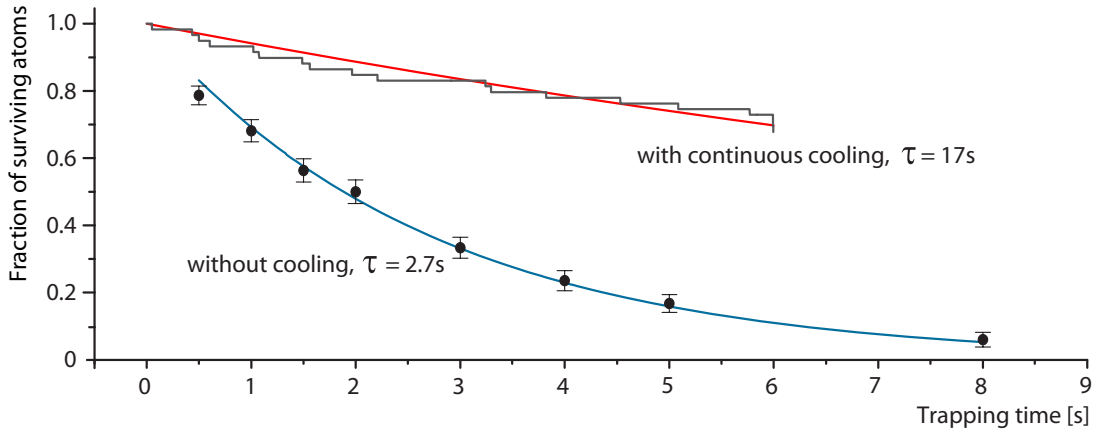

Figure 3.6: Atom lifetimes with and without cooling lasers. The continuous application of the counterpropagating pair of cooling lasers increases the lifetime of the atoms in the trap by more than a factor of six.

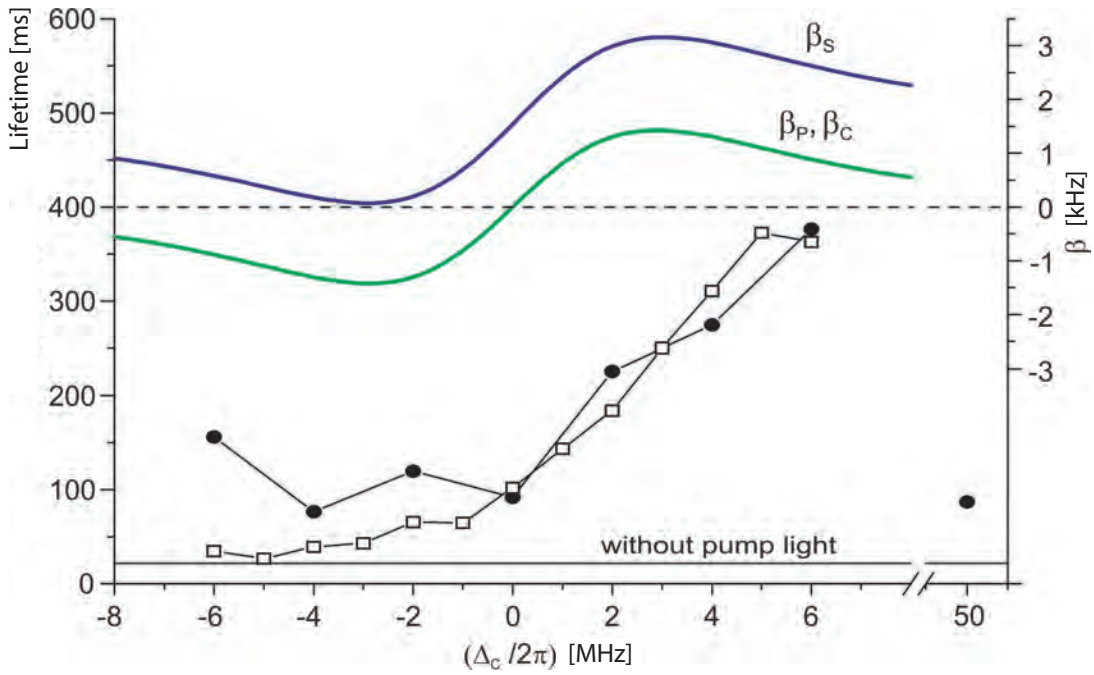

Figure 3.7: Atom lifetimes as a function of the cavity-pump detuning Δ_c. The two data sets are taken scanning the cavity frequency (circles) and the pump laser frequency (squares) respectively. Both show, in addition to the overall lifetime increase due to the Sisyphus-like force, an enhancement of the trapping time for positive Δ_c, which means the cavity is blue detuned with respect to the laser. These results are consistent with the expected behavior when comparing to the friction coefficients $\beta = -F/mv$ from the theory.

manner. As long as the atoms are not in the ground state of the trapping potential, they will oscillate in the trap at characteristic frequencies defined by the shape and depth of the trapping potential. By periodically modulating the trap intensity at twice the frequency of one of these trap oscillations, one can implement a parametric heating force acting on the atoms in the trap. If the strength of this force compares to the cooling forces in the system, the lifetime in the trap is significantly shortened. In our experiment, we applied a 7 kHz intensity modulation with an amplitude of 30% of the trap potential to reduce the 17 s from above to about 100 ms for the case of just the Sisyphus-like force being active. The lifetime without cooling lasers is now measured to be 25 ms instead of the original 3 s. To explore the effect of the cavity-cooling forces we did a scan of the detuning Δ_c between pump laser and cavity resonance, measuring the lifetime of the atom with a series of trapping events at each point. The results are shown in figure 3.7.

Two complete sets of data were taken, each with lifetime-measurements for a series of cavity-pump detunings Δ_c. In one of them, the cavity frequency was kept fixed at $\omega_c = \omega_a$ and the laser frequency was scanned. Its results are represented in the figure by the square symbols. In the other set, displayed as circles, the cavity was scanned with the laser tuned to the atomic resonance. Both curves show an overall enhancement of the atom lifetime in the trap compared to the value of 25 ms when no pump light is applied. The Sisyphus force lifts the curve independent of the detuning Δ_c, which can be seen from the additional data point at $\Delta_c = 50$ MHz, where the cavity is so far detuned, that it should have no influence on the lifetime any more. The additional rise of the curves on the positive detuning side, where the cavity has a higher frequency than the pump laser, can be attributed to the cavity-cooling forces. These forces should theoretically reach their maximum at $\Delta_c = \kappa$. This is not really visible in the graph, as there was no data taken for sufficiently large detunings to see the lifetime decreasing again. Compared to the level achieved by Sisyphus cooling alone, the cavity-cooling forces increase the lifetime by a factor of four. The total enhancement from 25 ms to ≈ 380 ms at $\Delta_c = 6$ MHz as a result off all four forces being active, correspond to an enhancement factor of ≈ 15. These numbers indicate that the cavity forces should have similar magnitude as the Sisyphus-like force.

3.4 Filtering well-coupled atoms

As mentioned earlier, our attempts on triggering on a transmission breakdown signal in order to trap a single atom in the cavity mode, were not successful. With the discovery of the cooling forces we found that, for a well aligned overlap of pump laser, dipole trap and cavity mode, the atoms will automatically be trapped such that they are well-coupled to the cavity. This is because the cooling forces also depend on the coupling to the cavity.

In the experiment sequence, we switch from the running-wave transportation trap to the standing wave configuration when the atoms from the MOT are expected to arrive in the cavity region. This will trap some atoms in the standing wave at random positions, but at the same time many atoms will still be hot enough such that they will randomly walk between the antinodes of the trap. As soon as these atoms get into the intersection of pump

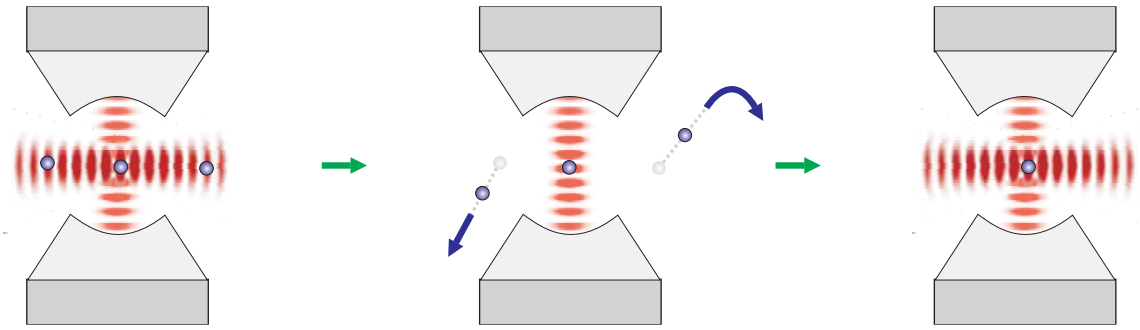

Figure 3.8: Filtering well-coupled atoms. To remove atoms which are not trapped within the cavity mode, the main dipole trap is switched off for a certain time interval. During this time, well-coupled cold atoms can be kept in the shallow trap provided by the cavity stabilization laser, while all other atoms are removed.

laser and cavity mode, they will experience the cooling forces. This leads to probability distribution for the trapping position peaked at the center of the cavity mode. So after a waiting period of typically 40 ms, there is a high probability of having at least one atom trapped within the cavity mode. But as there are still other atoms around which will occasionally enter the cavity region and also be cooled into the trap, the number of atoms in the cavity is not constant. To ensure a well-defined atom number for the whole trapping time, we developed a procedure to filter the well-coupled atoms from others remaining in the trap.

With the cavity stabilization light at 785 nm also red-detuned to our atomic transitions, it provides a trapping potential on the cavity axis, as mentioned in section 2.4. In this potential of approximately 30 μK depth, well-coupled cold atoms can be trapped for a while even without the deep trap at 1030 nm. We make use of this in our "filter phase" as illustrated in figure 3.8. First, we wait for atoms to get trapped in the cavity as described above. Then we switch of the standing wave for typically 10 ms. This will release all atoms from the system which are not at the right position and cold enough to survive in the small trap provided by the cavity stabilization laser. The remaining atoms are then recaptured in the main trap by adiabatically ramping up its intensity within another 10 ms. This procedure has been proven to be very efficient, leading to preferential trapping in the center of the cavity mode. Trapping position statistics show an atom distribution along the trap axis with a FWHM width of only 15 μm. [63].

3.5 Extension of the scheme for other transitions

The observed long trapping times were hard to achieve in the beginning as the system alignment was drifting on the timescale of single days. But along with technical improvements bringing more stability, the cooling scheme on the closed transition $F{=}3 \leftrightarrow F'{=}4$ turned out to be very reproducible, and even easy to align compared to the variations we tried later. For this reason, it can still be useful to do the basic adjustment of dipole traps

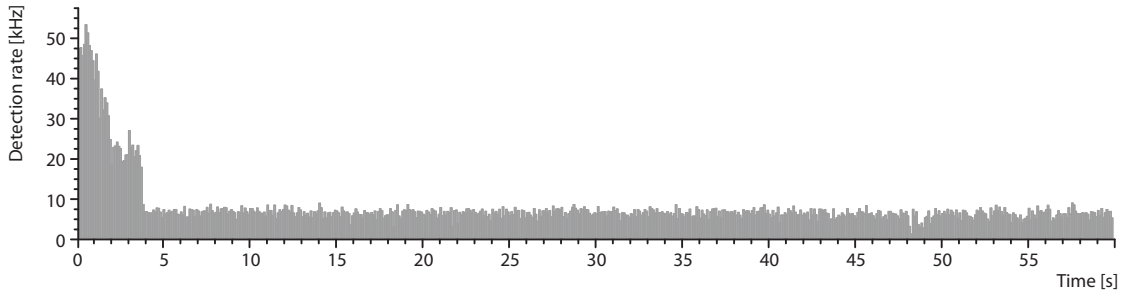

Figure 3.9: Trapping on an open transition for up to one minute. Technical improvements allow the recording of data up to a minute with nanosecond time resolution. This example trace demonstrates that such long trapping times can be achieved even with cooling on an open transition, where the relative contribution of the cooling forces is weakened by a larger number of necessary repumping processes.

and pump lasers on the closed transition, before starting with the fine-tuning on the more complicated schemes.

As I will describe in chapter 4, the implementation of a single photon protocol required a cooling scheme with the cavity tuned to the frequency of an open transition, namely to $F{=}2 \leftrightarrow F'{=}3$ in the case of the data that were published [61]. The open transition has the drawback, that the atom has to be frequently repumped back into the cooling process. This repumping normally does not contribute to the cooling of the atom and therefore the ratio between scattering events into the cavity and repumping determines the effective strength of the cooling forces.

With a pump laser and the cavity resonant with the unshifted $F{=}2 \leftrightarrow F'{=}3$ transition and an additional repump laser on $F{=}3 \leftrightarrow F'{=}3$, we were able to achieve trapping times comparable to those from the previous sections. The alignment for this needs a lot more fine-tuning than with the scheme using a closed transition, as the effective cooling force strength is reduced by the large number of recycling processes. Especially the balance of the two counter-propagating components of the pump light is important. It influences the momentum transfer distribution in the scattering processes and leads to heating for the case of an imbalanced light pressure. With additional technical improvements concerning the data acquisition, we were able to record trapping events with a duration of more than a minute, as demonstrated in figure 3.9. Typical lifetimes observed for this cooling scheme were $\approx 20\,\mathrm{s}$.

3.6 A new isotope: new trapping approaches

The experiments described in the later chapters 5 and 6 were carried out after we changed the Rubidium isotope from ^{85}Rb to ^{87}Rb. The first thing to try with the new isotope was

the cooling scheme with pump laser and cavity on the closed transition $F{=}2 \leftrightarrow F'{=}3$ and an additional repump laser on $F{=}1 \leftrightarrow F'{=}2$. As expected, the performance of the system was very similar to the results we had with ^{85}Rb. We could achieve trapping times of several ten seconds and almost the same characteristic signal levels. In combination with images of the trapped atoms obtained with a new camera system (see chapter 5), we could also get new insights on the absolute and relative positions of pump lasers, dipole trap and cavity mode of a particular system alignment.

For the entanglement measurements of chapter 6, we again had to use the cavity on an open transition, this time with full Stark shift compensation. While the cavity-cooling forces are still available in this situation, the Sisyphus mechanism will counteract with heating. With the excitation laser tuned to the potential maximum of the excited state (compare to figure 3.2), the effect of the Sisyphus force is opposite to what is intended. The emitted photon will have on average a lower energy than the one absorbed from the laser before, and thus increase the kinetic energy of the atom. With this Stark shift compensating laser configuration we did not find stable trapping conditions. The solution to the problem was to do without the cavity cooling and rely on the cooling force provided by a laser resonant with the unshifted closed transition $F{=}2 \leftrightarrow F'{=}3$. This laser is, due to the Stark shift, far detuned from the atomic resonance and therefore meets the requirements for efficient cooling. The results of this scheme are discussed in chapter 6 on the results of the entanglement measurements.

4 A single atom as a single-photon server

A single photon source using cold single atoms in free fall coupled to a high-finesse cavity was successfully demonstrated in our group in 2003 [69]. It featured a number of nice properties such as highly efficient photon collection by the cavity, a directed emission into a single spatial light mode, and emitted photons with well-defined frequency and wave-packet shape. To show that these photons are indistinguishable, experiments revealing the characteristic Hong-Ou-Mandel-dip [74; 4] when two photons interfere at a beam splitter were performed [75]. Even more exciting, two subsequently emitted single photons with a frequency difference tuned to a few megahertz revealed a quantum beat signal when the photons were brought to interfere [54; 70]. A different protocol tested with the apparatus showed the emission of single photons with alternating polarization [53], making the single photon source more deterministic, as a main property of the photon, the polarization, is well-defined. The major drawback of all these experiments was always the short interaction time between the atom and the cavity, limited by the freely falling atoms to only a few ten microseconds. With the trap configuration of our apparatus, we already demonstrated interaction times of several ten seconds, making use of the discovered cooling forces as discussed in the previous chapter 3. So the next step was to implement a pulsed scheme for single photon emission, including the cooling mechanisms to keep the long trapping times. With this upgrade to a "quasi-permanent" single photon source, we were able to characterize the non-classical statistics of the emitted photons even with one single trapped atom. With this new feature, allowing to test the emitted photon stream in real time, the system could act as a single-photon server with verified single-photon statistics [61].

4.1 Single-photon creation using vSTIRAP

The scheme for creating single photons applied in our system is derived from the well-known Raman process transferring the population between two atomic ground states with the use of two lasers in Raman resonance. In the case of our system, these two driving fields are given by a trigger laser pulse and, instead of a second laser, the vacuum mode provided by our cavity. As we will see in the following, the combination of the Rabi oscillation induced by the laser and the coupling g to the cavity allows a controlled population transfer between the atomic states while emitting a single photon into, and then from the cavity. The theory of this scheme was described in detail in [69; 70]. For this reason, I only give a brief introduction here.

We consider a system as illustrated in figure 4.1, consisting of two atomic ground states $|u\rangle$ and $|g\rangle$ and an excited state $|e\rangle$. While a laser drives the transition $|u\rangle \rightarrow |e\rangle$ with Rabi-Frequency Ω_l and detuning Δ_l, the other ground state $|g\rangle$ is coupled to the exited state $|e\rangle$ via the cavity with coupling strength $2g$ and detuning Δ_c. Raman resonance

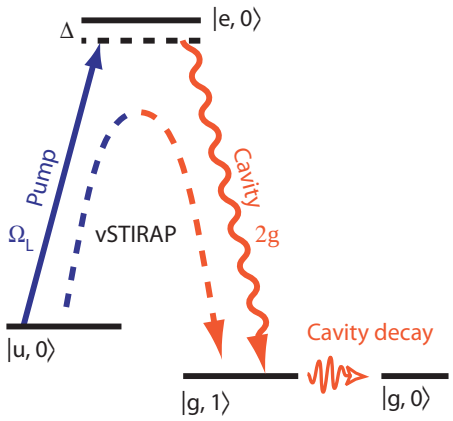

Figure 4.1: Single photon emission from a vSTIRAP process. With a trigger laser and the cavity mode as the two driving fields of a Raman transition, the population of the state $|u\rangle$ is transferred to another state $|g\rangle$ creating a single photon in the cavity.

conditions are fulfilled for $\Delta \equiv \Delta_l = \Delta_c$. This system is described by a Hamiltonian

$$\hat{H} = \hat{H}_c + \hat{H}_a + \hat{H}_{ue} + \hat{H}_{ge}, \tag{4.1}$$

composed of the cavity part, the atomic part and the interactions induced by the two couplings Ω_l and g. Assuming a lossless cavity described by a harmonic oscillator, we simply have

$$\hat{H}_c = \hbar\omega_c \left(\hat{a}^\dagger \hat{a} + \frac{1}{2}\right), \tag{4.2}$$

counting the photons with the creation and annihilation operators $\hat{a}^\dagger$ and $\hat{a}$. For the atomic part, we include the three states with

$$\hat{H}_a = \hbar \left[\omega_g |g\rangle\langle g| + \omega_e |e\rangle\langle e| + \omega_u |u\rangle\langle u|\right]. \tag{4.3}$$

The pump laser now adds an interaction between $|u\rangle$ and $|e\rangle$ described by

$$\hat{H}_{ue} = \frac{\hbar}{2}\left(\frac{\mu_{ue} E_l(t)}{\hbar}\right) \left[|e\rangle\langle u| + |u\rangle\langle e|\right], \tag{4.4}$$

with the transition dipole moment μ_{ue} and the time-dependent field amplitude $E_l(t)$. For the second interaction given by the cavity we have

$$\hat{H}_{ge} = \frac{\hbar}{2}(2g) \left[|e\rangle\langle g|\hat{a} + \hat{a}^\dagger |g\rangle\langle e|\right], \tag{4.5}$$

describing the creation or annihilation of a photon in the cavity while the atomic state alternates between $|g\rangle$ and $|e\rangle$. Taking these four components, the full Hamiltonian can be simplified using several assumptions and approximations. We transform $\hat{H}$ into the interaction picture rotating with Ω_l of the pump laser. This results in slowly rotating terms which describe the state evolution and fast terms oscillating at twice the optical

frequency. In the *rotating-wave approximation*, these fast terms are now neglected as small disturbances. The Hamiltonian in the interaction picture is then given by

$$\hat{H}_{int} = \frac{\hbar}{2}\left[-2\Delta|u\rangle\langle u| - 2\Delta\hat{a}^\dagger\hat{a} - 2g\left(|e\rangle\langle g|\hat{a} + \hat{a}^\dagger|g\rangle\langle e|\right) - \Omega_l\left(|e\rangle\langle u| + |u\rangle\langle e|\right)\right]. \quad (4.6)$$

Now we are interested in the eigenstates of this Hamiltonian and we find

$$\begin{aligned} |\phi^0\rangle &= \cos\Theta\,|u,0\rangle - \sin\Theta\,|g,1\rangle, \\ |\phi^+\rangle &= \sin\Phi\sin\Theta\,|u,0\rangle - \cos\Phi\,|e,0\rangle + \sin\Phi\cos\Theta\,|g,1\rangle, \\ |\phi^-\rangle &= \cos\Phi\sin\Theta\,|u,0\rangle + \sin\Phi\,|e,0\rangle + \cos\Phi\cos\Theta\,|g,1\rangle, \end{aligned} \quad (4.7)$$

with mixing angles Θ and Φ defined as

$$\tan\Theta = \frac{\Omega_l}{2g} \quad \text{and} \quad \tan\Phi = \frac{\sqrt{4g^2+\Omega_l^2}}{\sqrt{4g^2+\Omega_l^2+\Delta^2}+\Delta}. \quad (4.8)$$

The state description $|x,n\rangle$ combines the atomic state x and the number of photons in the cavity n. There is one remarkable aspect about these states, which is the key to the technique we want to apply called *vacuum-stimulated Raman adiabatic passage* (vSTIRAP). You may have noticed, that the eigenstate $|\phi^0\rangle$ only contains the two ground states $|u\rangle$ and $|g\rangle$, and not the excited state $|e\rangle$. With the system prepared in this *dark state*, we can arbitrarily distribute the ground state population by changing the mixing angle Φ without ever populating the excited state, therefore suppressing spontaneous decay processes. Without applying the pump laser, i.e. $\Omega_l = 0$, we have $\Theta = 0$ and inserting this into the state $|\phi^0\rangle$, we find our system to be in $|u,0\rangle$. Ramping up the pump laser intensity until it is large compared to the cavity coupling g will now transfer the atom to the other ground state and generate one photon in the cavity. The remaining step to a single photon source is that the photon has to be coupled out of the resonator, which is, until now, assumed to be lossless.

For a useful description, we have to include the cavity decay κ. Additionally, we also need to consider the case where our system does not completely follow the evolution of the dark state. Contributions of the other eigenstates of the system can then lead to the possibility of a spontaneous decay of the excited state with the characteristic rate γ. Including these loss mechanisms, we need to solve the Master equation

$$\frac{d}{dt}\hat{\rho} = -\frac{i}{\hbar}[\hat{H_{int}}, \hat{\rho}] + \hat{\mathcal{L}}[\hat{\rho}]. \quad (4.9)$$

In this differential equation, the lossless atom-cavity system is complemented adding the Liouville operator $\hat{\mathcal{L}}$. It contains two terms describing the decay losses from the excited state to the two ground states and one term accounting for the losses of the cavity. In Lindblad form it can be written as:

$$\begin{aligned} \hat{\mathcal{L}}[\hat{\rho}] = {} & \gamma_{eu}((2|u\rangle\langle e|\hat{\rho}|e\rangle\langle u| - |e\rangle\langle e|\hat{\rho} - \hat{\rho}|e\rangle\langle e|) \\ & + \gamma_{eg}(2|g\rangle\langle e|\hat{\rho}|e\rangle\langle g| - |e\rangle\langle e|\hat{\rho} - \hat{\rho}|e\rangle\langle e|) \\ & + \kappa(2\hat{a}\hat{\rho}\hat{a}^\dagger - \hat{a}^\dagger\hat{a}\hat{\rho} - \hat{\rho}\hat{a}^\dagger\hat{a}) \end{aligned} \quad (4.10)$$

A detailed analysis of these equations [e.g. in [76; 77; 78] reveals that the loss processes set some restraints to the parameters Ω_l, g, κ and γ if we would like to keep the system in the $|\phi_n^0\rangle$ state during the whole process. More specific, the state transfer has to occur adiabatically, meaning that the angle Θ varies only slowly with time, and κ and γ have to be small perturbations to the system. Therefore strong coupling with $g \gg (\kappa, \gamma)$ is required for an efficient process. Summarized into one condition, we call this process a *vacuum-stimulated Raman adiabatic passage* (vSTIRAP) if

$$\frac{g^2}{\gamma} \gg \frac{d\Theta}{dt} + \frac{\kappa}{2} \tag{4.11}$$

is fulfilled. In the experiment, apart from decisions made during the design process of the apparatus, obviously only one of the critical parameters, namely the pump intensity Ω_l, is freely accessible. This of course limits the efficiency of the vSTIRAP processes used in the experiments presented here and in chapter 6.

4.2 A single-photon scheme for our system

To incorporate the single-photon scheme into our system with a single trapped atom, we have to consider two main aspects. First, to repeatedly run the process, we must add an efficient repumping mechanism to transfer the atom back to the initial state once it has emitted the photon. Second, we have to ensure that the single photon production will not heat the atom and reduce its lifetime in the trap. As a solution, we found a way to include the cooling forces from chapter 3 into the repumping process. The only drawback is that this phase now has to be applied for a little bit longer as we need to scatter a few photons into the cavity for cooling purposes.

Transferred to our ^{85}Rb atom, the single photon production scheme works as illustrated in figure 4.2. Starting with the atom in the F=3 ground state, a vSTIRAP is driven via a pump laser pulse resonant with the unperturbed F=3 $\rightarrow$ F'=3 transition and the cavity tuned to Raman resonance with the transition F=2 $\rightarrow$ F'=3. With the laser Rabi frequency ramped up linearly over a period of 4 μs, we transfer the atomic state to F=2 while emitting a single photon into the cavity. As the photon build-up in the cavity is determined by the vSTIRAP process, the shape of the photon wavepacket leaking out of the cavity mirrors reflects the applied pulse shape. This means that the length of the photon is defined by the vSTIRAP process and not by the cavity decay.

We now need to transfer the atom back to the initial state in combination with a cooling process. Exciting the atom to the F'=2 or the F'=3 state are two possible repump transitions, but as the cavity is tuned to F'=3, we prefer a transfer via this state. Applying the laser with a detuning of a few megahertz to the red with respect to the cavity frequency activates the cavity Doppler-cooling forces while the system is cycling on F=2 $\leftrightarrow$ F'=3. With the pump laser being detuned to the actual atomic state by the Stark shift from the trap, the atoms get additionally cooled via the Sisyphus mechanism. As a cooling process involving the cavity does not end in the desired state, the enhanced emission into the cavity also lowers the repumping rate. However, from the photon histogram in figure 4.2

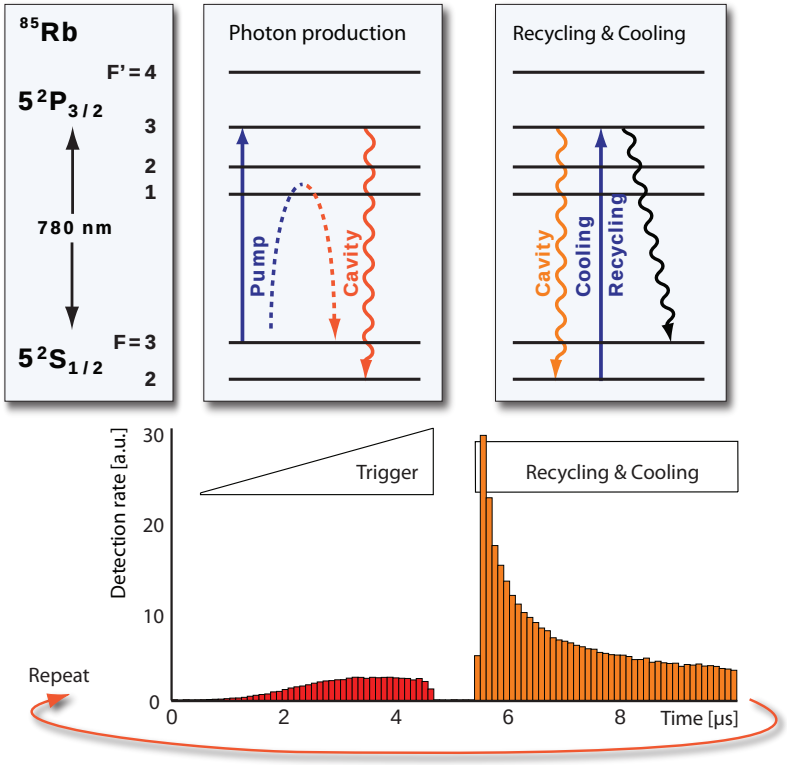

Figure 4.2: The scheme for single photon production with our system. The repump process is implemented such that it includes scattering processes into the cavity. This way we can make use of the cavity-cooling forces, albeit with the need of an extension of the repumping phase.

we can see that within $\approx 4.5\,\mu$s the repumping process is almost complete. As the atom trapping results showed, this cooling duty cycle of ≈ 0.45 is sufficient for lifetimes in the trap exceeding ten seconds. Closing the cycle with the repump process, the single-photon scheme is repeated with 100 kHz to emit a photon stream as long as the atom trapping time.

4.3 Properties of the single-photon source

The photons emitted from the cavity are detected with two single-photon counting modules (SPCMs) arranged in a *Hanbury-Brown & Twiss* configuration as seen in figure 4.6. Splitting the signal onto the two detectors allows simultaneous detection of two photons. A pulsed single photon source is characterized by the absence of correlations between the two detectors within the same pulse. An ideal two-photon correlation function should therefore show a constant correlation level for any temporal separation $\Delta\tau \neq 0$ between the photons and a gap at $\Delta\tau = 0$. A typical result for our system obtained from a single-atom trapping event is reproduced in figure 4.3, showing the characteristic signature of "photon antibunching". It is remarkable that even this single example data trace gives enough statistics to clearly reveal this non-classical property of the emitted light. In

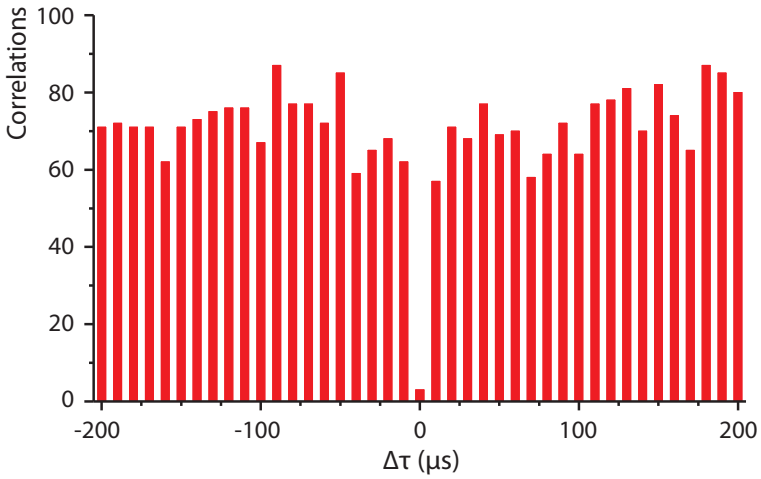

Figure 4.3: Correlation signal obtained from a single trapped atom. The missing correlations at $\Delta\tau = 0$ verify the emission of single photons. This signature is referred to as "photon antibunching", in contrast to classical light sources showing a flat (coherent light source) or "bunching" (thermal light sources) signal in the correlation function.

other experiments with neutral atoms one usually had to average over many single-atom observation intervals to collect enough data to observe antibunching [51; 52; 79].

For a systematic investigation of the properties of the single-photon source we need a large set of data to accumulate statistics. With our atom loading scheme using the filter phase and variable MOT loading times, we can approximately set the system to load on average one atom. As the atom number follows a Poisson distribution, also trapping events with two or more atoms will occur. In chapter 3 we found that the photon detection rate can be mapped onto the number of emitting atoms (see figure 3.5). Making use of this, our evaluation software decides on the signal level obtained on a 100 ms timescale whether the signal from a data trace can be attributed to a single atom. Specific for the system alignment we had for these measurements, we often found several trapped atoms in the beginning of a sequence. However, typically all but one escaped from the trap within a few seconds. The mechanism behind this observation is not clear, but we accepted this phenomenon and adapted our data selection rules such that we would scan the data trace until the first occurrence of a single-atom signature.

With this method, a set of 526 single-atom traces was selected from a full measurement series. These atoms show a $1/e$ lifetime in the trap of 10.3 ± 0.1 s. This lifetime reduces to 8.3 ± 0.2 s with the requirement that only one atom is trapped, meaning that we count the trapping time from the first point in the trace showing just a single-atom signal level. The reduction of the lifetime compared to the results from chapter 3 should be due to the reduced duty-cycle for the cooling in our pulsed scheme.
In total, the set of data contains 4397 s of single-photon production, in which 4.2×10^6 photons were detected. With a repetition rate of the pulsed scheme of 100 kHz we find that this corresponds to a probability to detect a photon from a specific pulse of 0.93%. With a overall detection efficiency of 10.5%, the photon-generation probability is therefore

9%. This includes the efficiencies of the detectors ($\approx 40\%$), losses in the optical path and a $\approx 50\%$ loss at the cavity mirror due to a dust particle in the center of the TEM_{00} mode. Although we do not expect unit production efficiency for the vSTIRAP process, the efficiency here is even lower than the ones observed in the single-photon experiments performed with the preceding apparatus. These efficiencies of up to 41% [53; 71] were conditioned on a photon emission in the previous pulse. Compared to an overall average, this usually gives larger values as we already know that the atom is well-coupled. In addition, the atoms were optically pumped into states giving the largest possible coupling g. Nevertheless, we think that there is a difference in the efficiency coming from the dynamics of the atomic motion in the trap, resulting in a dynamic Stark shift of the atomic states.

4.4 Data selection with a correlation test

With the investigation of various data sets we saw that the visibility of the antibunching for a full data set often failed to meet our expectations. With the data selection relying only on the detection of characteristic signal levels, we estimate the probability that a two-atom trapping event enters the evaluation to be about 5%. For example, two atoms trapped in the outer wings of the cavity mode can mimic the signal of a well-coupled single atom in the center of the mode. Assuming a rather long trapping time with several thousand detected photons, a small number of such traces could completely hide the antibunching signature in the correlation function.

In search for a more efficient way of detecting single atoms, we recognized that the correlation function of just one trapped atom already reaches an average level of ≈ 20 correlations per point. It should therefore be possible to use the photon signal detected during a small fraction of the total trapping time to test the signal on antibunching criteria. The implementation of such a test led to the following data selection rules. From each data trace verified to contain at least 3 s of signal at the characteristic single-atom signal level, the photons from the first 1.5 s are selected for an antibunching test. If the average number of correlations for non-zero time difference is larger than 1.5 and the number of correlations at $\Delta\tau = 0$ is less than 30% of this average, the coincidence test proves that single photons are produced and thus just one atom is present in the trap. The minimum correlation level ensures a rather good atom-cavity coupling, leading to a reasonable photon emission rate. The seemingly large tolerance concerning the antibunching visibility relies on the observation that two atoms usually show a signal at $\Delta\tau = 0$ of at least the average correlation level. On the other hand, the probability to get a coincidence at $\Delta\tau = 0$ via background signal detection is about 10% per second of recorded data. The parameters were therefore chosen such that multi-atom data is efficiently suppressed and at the same time single-atom events are not unintendedly discarded due to background noise.
One could of course object that we are selecting on a signal that we use to show the actual effect. We are considering this as a test to predict the performance of photon source for the next few seconds. For the evaluation, we therefore exclude photons from the 1.5 s test interval.

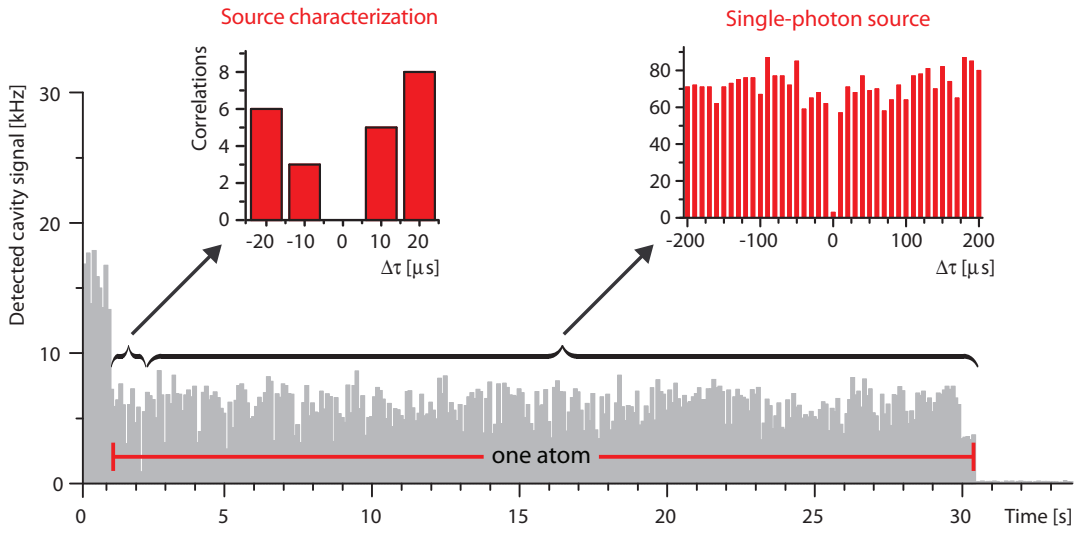

Figure 4.4: Real-time verification of the single-photon source. Starting with the first detection of a single-atom signal level, we test the correlations detected during 1.5 s for an anti-bunching signature to predict the properties of the photon stream emitted in the following. This can be evaluated in real-time and one can decide online whether the photons are suitable for a possible user.

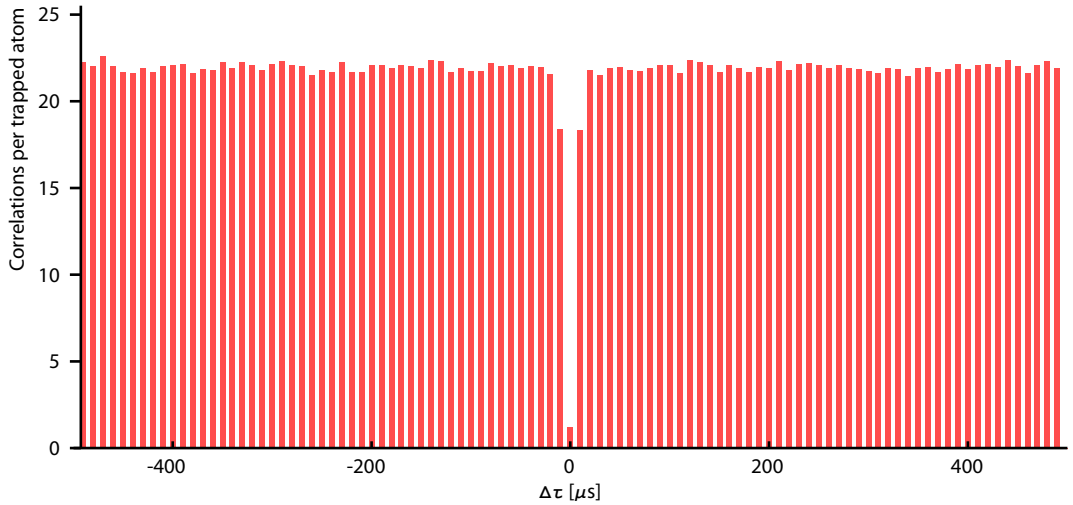

Figure 4.5: Average correlation signal obtained from one trapped atom. The remaining correlations limiting the antibunching visibility to 94% can be completely explained by background signal from the detectors.

Applying these selection rules to the data and calculating the correlation function for the complete set, we find the average antibunching visibility to be 94%. This result is displayed in figure 4.5. While the correlation level of ≈ 22 is flat within the statistics, the two bars right next to $\Delta\tau = 0$, reflecting the probability to emit photons in two subsequent pulses, are smaller by about 15%. This (and also the incomplete repump pulse in figure 4.2) indicates that the repump process is not efficient enough, which could also be one of the reasons for the limited photon production efficiency.

4.5 A single-photon server

The ability to diagnose the properties of the photon source within a small fraction of the atom's lifetime in the trap opens possibilities for applications for the system. The signal level detection and the correlation test can be performed in real time. On a decision based on this test, either the system has to be reloaded, or the cavity output could be directed to a user for the remaining time the atom is in the trap. Such a possible application of the system as a single-photon server is illustrated in figure 4.6.

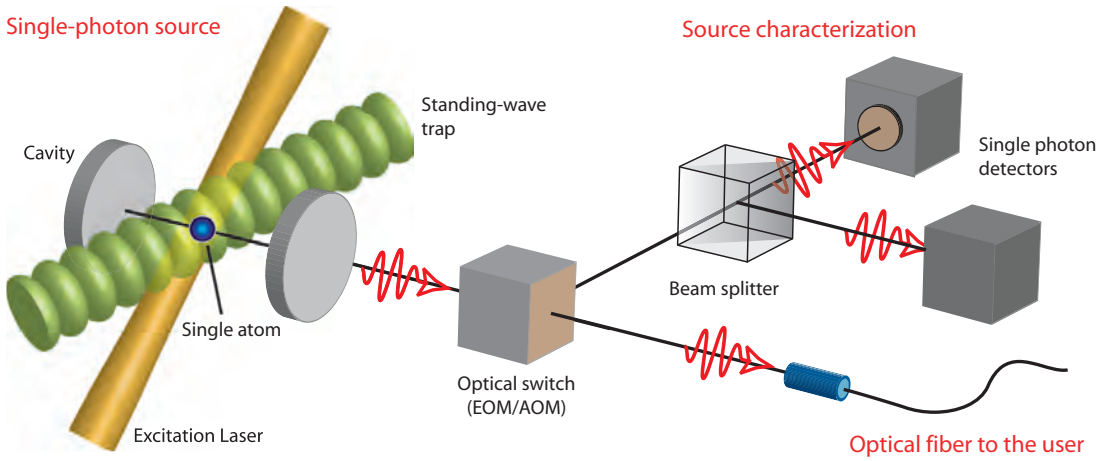

Figure 4.6: Scheme for an application as a single-photon server. With the characterization performed online within a fraction of the trapping time, one could direct the photons emitted in the following to a user via an optical switch. With our current system, such a photon server could provide single photons at a rate of 1.2 kHz

In a realistic scenario, one could use an acousto-optic modulator (AOM) to direct the signal used for local evaluation to our detection setup, and (for efficiency reasons) couple the direct transmission of the AOM to a fiber for application purposes. For the test interval, we would have to evaluate the full signal from the cavity. In the following time, sorting out the signal from the repump processes could give us sufficient information about the atom without affecting the delivery of single photons to the user. The real-time analysis of the data was implemented on a field programable gate array (FPGA) and successfully tested

with simulated data. However, the full scenario was not implemented in the experiment so far.

Analyzing our data under the conditions of this scenario, we find that we could detect the loss of an atom from the trap with 98% probability within 30 ms with just the signal from the repump processes. Reloading an atom after the loss is detected takes about 1.5 s. With the possibility of initially loading several atoms as discussed above, one then has to wait for $10.3 - 8.3 = 2.0$ s on average before a coincidence test can be performed. After that test, the single atom is available for another $8.3 - 1.5 = 6.8$ s, giving a total duty cycle of 58%. As trapping times up to 30 s with almost 300 000 photons emitted from one and the same atom have been observed, further improvement on the overall atom lifetime with better alignment of the system seems feasible. This could even increase the system's duty cycle.

With the current data, 2×10^3 of the 9×10^3 single photons that are produced per second would be available for distribution. This takes into account that we lose 50% at the cavity mirror due to the dust particle and another 55% during the separation from the 785 nm stabilization light and spatial filtering. As a single atom is available for photon production for 58% of the time, this means that the photon server can provide single photons at a rate of 1.2 kHz on average.

5 High contrast imaging of single atoms

For a long time, the photon stream collected at the cavity output was the only source of information about the atoms in the experiment. Its characteristics can tell us about the number of trapped atoms, the quality of the atom-cavity coupling, and the non-classical properties of the emitted light, as seen in the previous chapters 3 and 4. However, this signal is sometimes ambiguous, so one can not solely rely on this source of information (see section 4.4). The detection of photons emitted perpendicular to the cavity into free space adds a new dimension to the accessible information about the trapped atom. Therefore, a lens system allowing the detection of single atoms on a CCD-camera was developed and installed by Markus Hijlkema. The system is already described in his thesis [61], but unfortunately we were not able to clearly resolve single atoms at that time. After some improvements, not only the number of trapped atoms but also their position can now be resolved with high efficiency. The camera system additionally became a powerful tool for a systematic alignment of the experiment, as the atoms always scatter light into the camera, irrespective of their coupling to the cavity.

5.1 The camera system

At the time the experiment layout and the vacuum chamber were designed, the installation of a lens system and a camera was already planned. This is why the top viewport was chosen to be reentrant such that the imaging system could be mounted as close as possible to the trapped atoms (see figure 5.1). This reduces the distance between the atom in the cavity and the outside surface of the viewport to 22 mm. The maximally observable solid angle is limited to an numerical aperture of $n \cdot \sin\alpha = 0.43$ (with $\alpha = 25.4\,^\circ$) by the size of the hole in the piezo tube holding the cavity mirrors. These boundary conditions require the use of lenses with large clear aperture, leading to rather large lens aberrations, which need to be compensated to obtain high resolution images.

To image the atoms in the trap onto a camera, a new lens system was designed and optimized using the optics design software ZEMAX. It consists of five custom lenses produced by *Rodenstock* housed in a tube system developed and machined at the institute's machine shop. Details about the imaging system are shown in figure 5.1, together with the parameters of the lenses in the respective table. Together, these lenses form an objective that collects the light from the atom at a focal distance of 25 mm and collimates it. An additional singlet lens with 700 mm focal length finally images the atoms onto the CCD-chip of the camera. The expected magnification factor of the imaging system is therefore 28. The properties of the lens system were investigated in a series of measurements imaging a micrometer scale and simulating an emitting atom using pinholes with diameters down to 1 μm. The result was a measured resolution of 1.3 μm, which is close to the theoretical diffraction limit of 1.1 μm for our given numerical aperture.

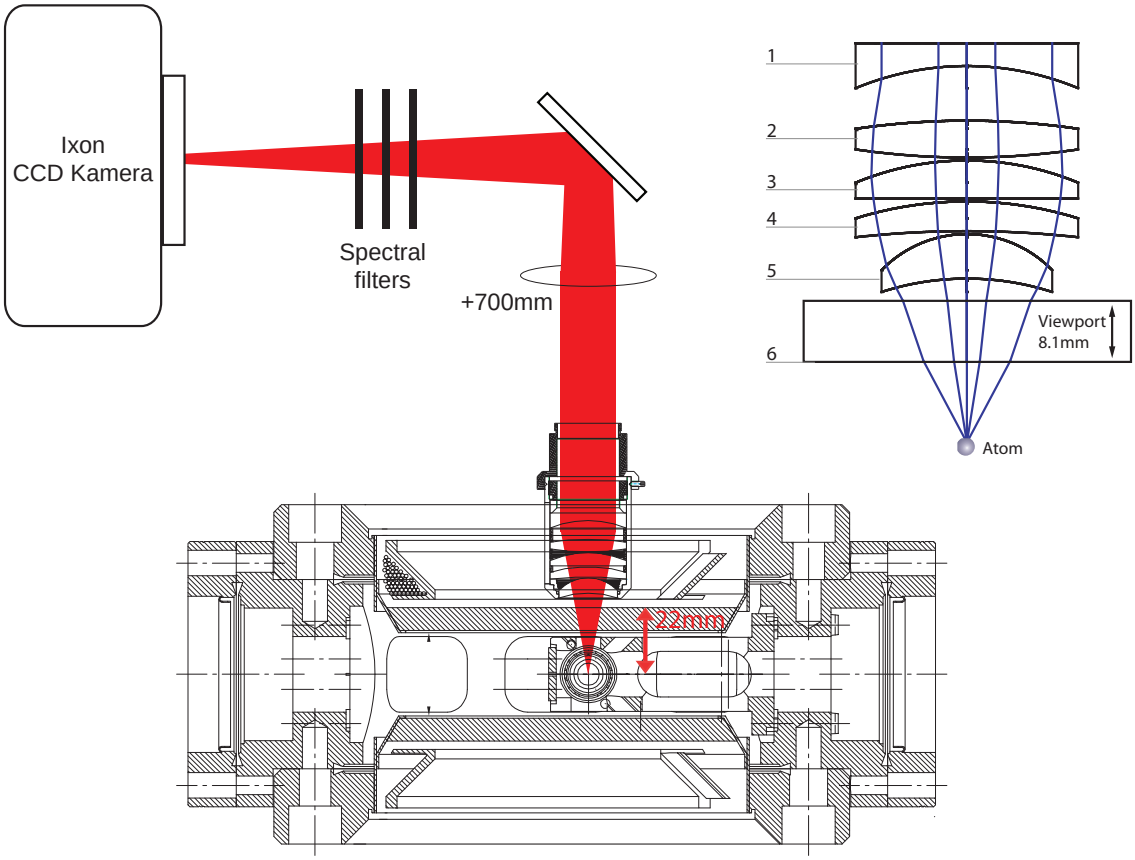

Figure 5.1: Camera and lens system. The five-piece lens has a focal length of 25 mm and collimates the light emitted from the trapped atoms. An additional 700 mm lens images the atoms onto the chip of the CCD camera.

Lens No.	Type	Material	Surface curvatures		Thickness	
			Top	Bottom	Lens	Air gap
1	plane-concave	BK7	∞	39.10 mm	3.08 mm	7.37 mm
2	bi-convex	BK7	103.29 mm	−103.29 mm	4.97 mm	0.40 mm
3	convex-plane	BK7	39.10 mm	∞	5.12 mm	0.40 mm
4	convex-concave	BK7	50.49 mm	136.752 mm	4.00 mm	0.40 mm
5	convex-concave	BK7	16.02 mm	37.58 mm	6.00 mm	2.99 mm
6	viewport	fused silica	∞	∞	8.1 mm	

Our CCD-camera, model *Ixon DV887* from *Andortech*, has a sensor array of 512×512 pixels with a pixel size of $16 \times 16\,\mu m^2$. A special on-chip electron multiplication gain amplifies the collected signal before analog-digital conversion takes place, thereby increasing the signal-to-noise ratio by a factor of up to 1000. The images are read from the camera using *QIxon*, a graphical user interface programmed in C++ using a library provided by *Andortech* to address the camera.

5.1.1 First images and technical improvements

Since the first attempts to image a single atom [61] were not convincing, we reoriented the objective and carefully adjusted the focal plane to the position of the standing-wave trap. We were then able to obtain pictures showing a good signal-to-noise ratio with exposure times down to 500 ms. With these images resolving the trapped atoms in the cavity we gained new insight into the geometry of the system. Using the images as a new source of information about the atom-cavity system, a series of measurements were carried out. We investigated, for example, whether chains of trapped atoms arrange in certain patterns and whether one could show the influence of the Purcell-effect of the cavity on the photon scattering into free space. The results of these measurements are described in the diploma thesis of Tobias Müller [80].

To further increase the signal-to-noise ratio of the images, we replaced a 50/50 beam splitter contained in the lens system by a mirror. The beam splitter was originally installed to have the possibility of adding a tightly focused laser beam to address the trapped atoms from the top. With the mirror installed and new spectral filters of type *LL01-780-25* from *Semrock* with a better transmission of $\approx 97\%$ at 780 nm (see figure 5.1), we were able to increase the signal collected from a single atom by a factor of ≈ 2.5. Additionally, we found that the lens system was not exactly vertically mounted and thus the light collimated by the lens was partially lost at the walls of the lens tube. With these corrections, we now had more than 4 times more light on the camera, allowing us to reduce the exposure time to 100 ms and still receive pictures showing an even better contrast than those taken with 500 ms exposure time before the improvements.

Concerning the software, the rate at which images could be taken was limited by the duration of the camera readout process to about one per second. But as the camera software library offers a feature, where the images are temporarily stored in the camera during an exposure series, we implemented this into our software *QIxon*. Reading the whole image series upon completion of the exposure series now only requires a separation of 100 ms between two exposures. This is the amount of time the camera needs to read the CCD-chip, amplify the signal and to do the AD-conversion. So with a minimum exposure time for good atom signals of 100 ms, one can take five images in a second.

When it comes to the adjustment of the lens to the cavity mode, the dust particle on one of the cavity mirrors causing so much trouble in other measurements now becomes helpful. When the cavity is locked, the dust particle scatters a portion of the locking light into free space. As we know the dust particle to be exactly in the center of the TEM_{00} mode,

moving the objective to that mirror and focussing on the bright spot sets the focal plane of the lens at exactly the height of the standing-wave trap. Now we simply have to scan along the cavity axis to find the atoms.

5.2 Image analysis and single atom identification

The images taken with the camera are saved in two formats, one contains the raw, 14-bit data in a self-defined format named ".hid", the other is a standard ".png" file with the pixel values mapped onto a 256-color palette. All example images shown in this chapter are the ".png" versions. Although their color range is scaled, they give a good visual impression of the signal-to-noise ratio. The raw data pixels have a value range of $[0, 16383]$ and all show a general offset of typically $900 - 1200$, depending on the exposure time and the exposure duty cycle. This offset has technical reasons based on the internal design of the camera. On top of this offset, we find background noise due to stray light and electronic noise from the camera readout process. For an exposure time of 0.5 s this noise level is about 40. Additional to the shot-noise, sometimes interference fringes are visible with an amplitude of up to 100. These exposure-time dependent properties of the images have to be considered in the automated image analysis we use to identify position and brightness of each of the visible atoms.

To perform such an image analysis, we define a region of interest (ROI), covering the area where trapped atoms are expected to appear on the image. We then project the pixel values in the ROI on the dipole trap axis. This procedure is illustrated on two example pictures in figure 5.2, one containing a chain of seven atoms and one with just a single atom. The resulting one-dimensional graph can now be scanned for its maxima.

While there exist of course sophisticated fitting routines to solve this problem, we use a simple algorithm in the evaluation software *QDataExplorer*. It works as follows:

- We calculate the average signal level of the whole image. As single atoms only cover a fraction of the image of $\approx 10^{-4}$, this value is quite close to the real background.
- With the average value as a reference, the curve is scanned for values exceeding it by at least a predefined threshold value.
- Any continuous series of pixel values fulfilling this criterion is considered as an atom signal with the width of the corresponding number of pixels.
- Depending on this signal width, the software distinguishes between a noise pixel, a single atom, or several atoms sitting too close together to be identified individually. This decision is controlled by two user-defined parameters, the minimum and maximum width for accepting a single atom signature.

In the algorithm, we only need three parameters to adapt the atom detection to our images. With the possibility to define a maximum atom number (for most purposes this

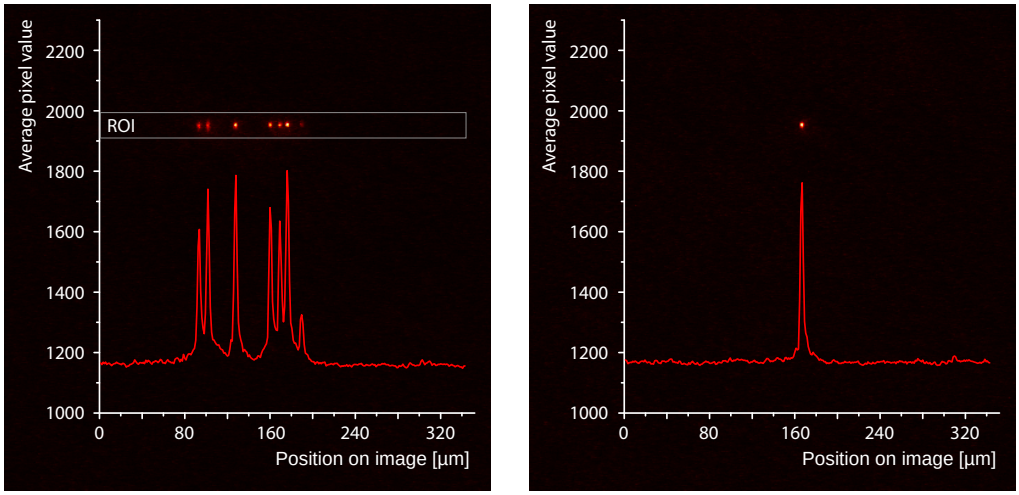

Figure 5.2: Atom image analysis. The signal in the region of interest of the image is projected onto the dipole trap axis by averaging the pixel values. A search algorithm examines the curve and extracts signal brightness, width and position for each atom.

is set to 1), the evaluation software can automatically select matching files from a full set of data. During the detection process, the algorithm additionally calculates the atom positions relative to the ROI and their absolute brightness by summing up the pixel values and doing a signal-weighted average over the atom regions.

The images in figure 5.2 show some of the best signal-to-noise ratios obtained with this system. We find averaged peak values of almost 1800 for some of the atoms, i.e. a signal of roughly 600 on a background of 1170, compared to a noise level of ≈ 10. The resulting signal-to-noise ratio therefore reaches values up to 60 : 1. The pictures were taken with an exposure time of 500 ms and show atoms that were cooled with the cavity on the cycling transition $F{=}2 \leftrightarrow F'{=}3$, giving a rather large scattering rate into the cavity and into free space simultaneously.

5.3 A new alignment tool

With the camera images, the positions of the atoms in the trap can be spatially resolved. This additional information about the system really helps when it comes to the alignment of its components, e.g. the optimization of the standing-wave trap or the positioning of the pump beams. Until now, we only had the scattering into the cavity as a feedback signal, which does not reveal clear details about the quality of the standing wave. Previously, we optimized the alignment of the standing-wave by systematically scanning the retro-reflection of the trap beam on all axes while monitoring trapping times. On the camera images we can now see a clear transition from an elongated cloud of atoms trapped in a running wave to clearly separated single spots as soon as the two counter-propagating

beams of the trap overlap in the cavity. With the focal plane of the camera lens once set to the ideal trapping position for the atoms, the standing-wave trap can be optimized by searching for the minimum signal width transverse to the trap axis.

Using the advantages of the camera images, a typical alignment procedure would be carried out as follows. First, we start with atoms loaded from the MOT into the transportation trap and probe light coupled into the cavity. The transportation trap is then positioned such that the cavity transmission breakdown due to atoms entering the mode is maximized. The next step is to load the atoms into the main trap, but with the retro-reflection blocked, making it just a running-wave trap with focus in the cavity. With the pump lasers applied, we can see on the camera images, where the atoms are trapped. This, of course, also reveals the pump laser positions relative to the trap. We can now optimize pump laser and trap positions until we get the maximum cavity output. It is even possible to individually adjust the two pump laser components applied from above and below of the vacuum chamber. A criterion for a good alignment at this stage would be to have a few atoms surviving a filtering phase with the atoms temporarily stored in the intra-cavity trap (as described in chapter 3.4). We can now continue with the alignment of the retro-reflected beam to form the standing wave trap, looking at both the survival probability during the filter phase and the signals on images taken before the filter phase. The characteristic signal transition mentioned above should be clearly visible and finally lead to images similar to the one shown on the left of figure 5.2, maybe with a larger number of atoms. Reducing the atom number, we finish the alignment process by fine-tuning the single-atom loading probability, the flatness of the cavity signals, and the atom lifetime in the trap.

5.4 Systematic evaluation of single-atom images

The camera images contain more than just information about the positions of the trapped atoms. For example, their brightness on the pictures versus their position can be linked to the applied pump intensity profile. Also, the measured width of the atom signals can either tell us something about the temperature of the atoms [81] and the trap alignment, or whether the camera lens is correctly positioned. To do a systematic investigation, we took a full series of atom images together with corresponding cavity output signals. The software selected 172 data files showing both a constant cavity signal and a single atom on the picture. This data set is the basis of the evaluations discussed in this section.

From each of the atom images, we extract the atom's position and brightness. The brightness is calculated as the total signal of the picture area containing the atom after subtraction of the background offset. This atom signal can now be compared to the corresponding cavity signal. For this purpose, we determine the average photon detection rate during the image exposure time. Plotting the brightness on the image versus the cavity output signal as shown in figure 5.3 a), we find two groups of data points. One represents trapping events outside the cavity mode, the other one atoms coupled to the cavity. Although there is some scattering in the image signal, the data points of the second group show a linear behavior. The typical error on the atom brightness is estimated to be at most 15%,

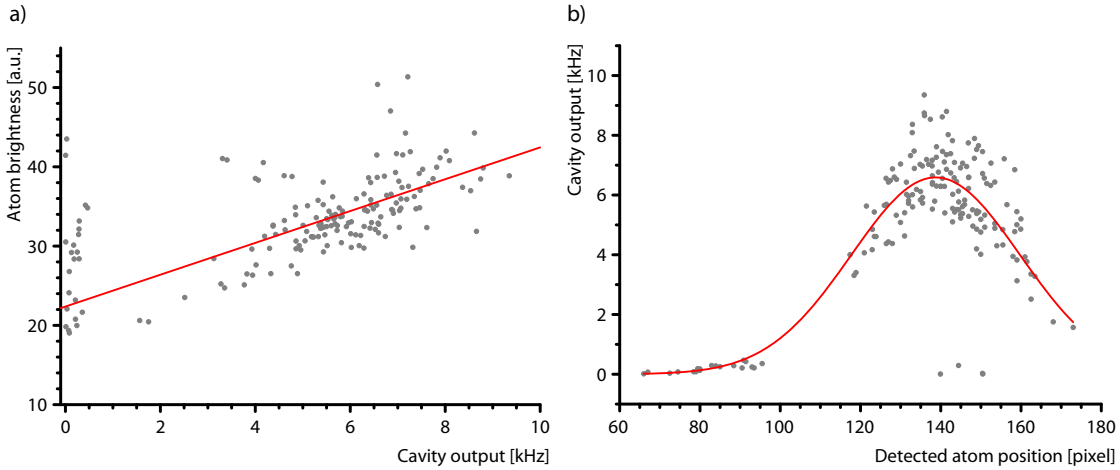

Figure 5.3: Systematic evaluation of the camera images. a) The atom brightness scales approximately linear with the cavity output signal. b) The cavity mode can be mapped to the atom images in a comparison of cavity signal and atom position on the image.

including image noise and signal detection imperfections. While this explains part of the scattering, the rest is attributed to differing atom-cavity coupling values, depending on the individual trapping positions of the atoms. However, image and cavity signals seem to be proportional.

Figure 5.3 b) shows the cavity signal as a function of the detected atom position. These data points can again be divided into the two groups. The majority is well-coupled to the cavity, showing a signal peak around pixel 139. The four single dots below the signal peak are most likely experiment runs where the cavity was not correctly locked to the atomic transition. From a Gaussian fit we find the peak to have a full width at half maximum (FWHM) of 49.5 pixels. With the theoretical magnification factor 28 for the imaging system and the pixel size of $16 \times 16\,\mu\text{m}^2$ giving a scale of $0.58\,\mu$m per pixel , this corresponds to a width of $28\,\mu$m.

The obtained width from the cavity signal is a factor of two smaller than the expected value. From the cavity parameters we calculated the waist of the Gaussian mode to be $\omega_0 = 30\,\mu$m. For the FWHM-value, this has to be doubled to $60\,\mu$m. This is not only a theoretical value, it is also verified by data where single atoms have been shuttled trough the cavity mode via a rotatable glass plate (see chapter 2, figure 2.5) in the optical path of the standing-wave trap [58; 63]. In this data, a cavity signal output is observed over a atom transport range of $\approx 60\,\mu$m. In principle, this can also be seen on the very similar data shown here in figure 5.5, however this is not as easy as it shows the signal of two trapped atoms shuttled through the TEM_{10} mode of the cavity.

For a more detailed investigation, we can directly map the intensity profile of the cavity mode, which is proportional to the square of the coupling g. As derived in the thesis of

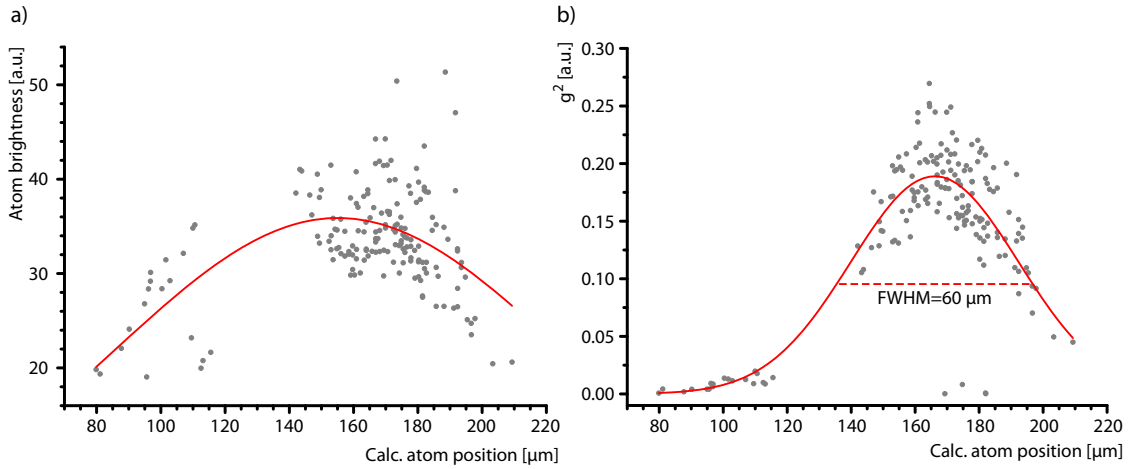

Figure 5.4: Pump laser and cavity mode profiles scaled to the width of the TEM_{00} mode. a) Derived from the atom brightness on the images, the pump laser profile is twice as wide as expected from the calculations. This reveals alignment imperfections of the pump beam. b) The cavity mode profile ($\propto g^2$) is obtained by dividing the cavity signal by the pump laser intensity.

Stefan Nußmann [63], the scattering rate into the cavity is in good approximation given by

$$R_{scat} \simeq 2\kappa \frac{g^2}{\Delta_c^2 + \kappa^2} P_e. \tag{5.1}$$

With constant cavity decay κ and laser-cavity detuning Δ_c, the rate depends only on the spatial variation of the coupling g and the atomic excitation probability P_e. For small values, this probability is approximately given by the pump laser Rabi frequency Ω_l as

$$P_e \simeq \frac{|\Omega_l|^2}{\Delta_s^2}. \tag{5.2}$$

For our timescale of several hundred milliseconds, the Stark shift is also constant. So with Ω_l^2 being equivalent to the pump laser intensity, we can simply divide the observed scattering signals from the cavity by the pump intensity profile. The obtained values then depend only on g^2, which corresponds to the cavity mode intensity.

We derive the pump laser profile by plotting each atom's brightness on the image versus its position and fitting a Gauss function to the distribution. Using this fit, we can now calculate the relative g^2 values and also plot them against the atom position. To make the data fit to the waist of the cavity mode, the position scale is adapted such that the FWHM-value for the g^2 data is now $60\,\mu$m. The consequence is of course, that the resulting magnification factor of the imaging system is $m = 14$, as there is no other way of explaining the data. With this, each pixel of the CCD chip corresponds to an area of $1.2 \times 1.2\,\mu\text{m}^2$ in the object plane.

Both, the pump intensity distribution and the obtained cavity mode profile are scaled using the measured magnification and plotted as shown in figure 5.4. For the pump

profile, we find a FWHM-value of 165 μm. This is much broader than the ideal value of 70 μm calculated from the parameters of the pair of pump beams. It reveals that the actual pump beam alignment either is not correctly focused in the cavity mode, or the two components do not perfectly overlap. The long atom trapping times however show, that the two beam intensities are balanced in the trapping region. The two separated groups of data points could support the assumption that the two beams have different foci. With one focus in the cavity mode and the other beam being wider at this point, stable trapping conditions would only be available on the sides of the tight focus. As the system alignment is optimized on the cavity signal, the pump lasers were probably placed such that one of the trapping regions is centered in the cavity mode.

While there is much room for interpretation, these results show that a combined evaluation of cavity signals and camera images can reveal many details about the system. We also learn here, that as we work with a complex system and rely on only a few sources of information about it, the real system in the lab can easily differ from the ideal experiment by factors of two or three. So the installation of the camera did not only help with the alignment of the system, but it also revealed some weak points. On the other hand, as we successfully worked with the system for years, the cooling and trapping mechanism seem to be quite robust against imperfections.

5.4.1 Mapping of the cavity mode in a single run

A quick method to locate the cavity mode on the camera images is to make use of the rotatable glass plate in the dipole trap optics and combine a cavity mode scan with an image. An example of this procedure with two trapped atoms and the cavity locked to the TEM_{10} mode is shown in figure 5.5. We start with the two trapped atoms and take a picture of them with an exposure time of 0.3 s. Then the atoms are sinusoidally moved in and out of the cavity mode over a total distance of $\approx 160\,\mu$m. The obtained cavity signal gives information about the position of the cavity mode with respect to the position of the atoms on the image. In the example, first the signal disappears, which means both atoms are decoupled from the cavity . We then see the transition of the right atom through the left maximum of the mode. After the turning point, both atoms are moved through the two maxima of the mode, resulting in three characteristic peaks with the central one (with both atoms coupled) being twice as high as the other two. The order of appearance of these atom transitions create a relation between the cavity mode and the atom position. This makes it possible to map the position of the cavity onto atom images within a single of maybe a few experimental runs. Once the cavity is identified on the images, the pump lasers can be aligned relative to it.

5.4.2 Single atom movies

With the technical possibility to store a series of images in the camera before transferring them to a computer, we were able to create short “movies” of single atoms with a frame rate of up to 5 Hz. While these movies typically consist of a series of images showing not

more than a static bright spot on a flickering background, they once again confirm that our atoms usually stay at their positions in the trap. As a movie can obviously not be printed in a thesis, I show a 30 s long trapping event along with a series of images taken during that time and give a short summary of the movie content: the atom stays and stays...

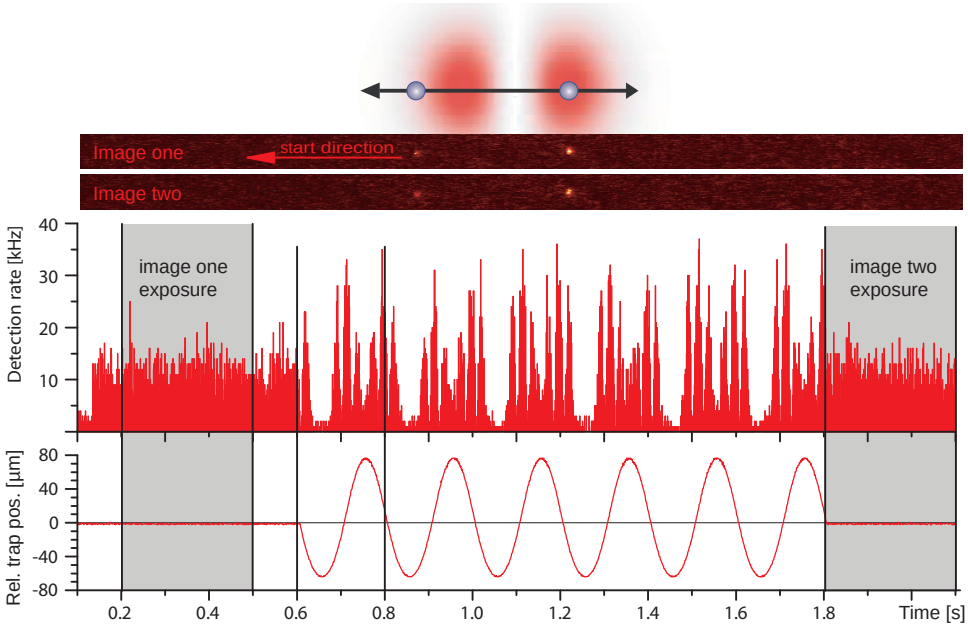

Figure 5.5: Cavity mode scan. We combine atom images with a scan of the TEM_{10} cavity mode by periodically moving the standing-wave trap together with the atom. The characteristic cavity signals allow to map the cavity position onto the images. Once this position is known, the pump lasers can be optimized to preferentially trap atoms in the center of the cavity mode.

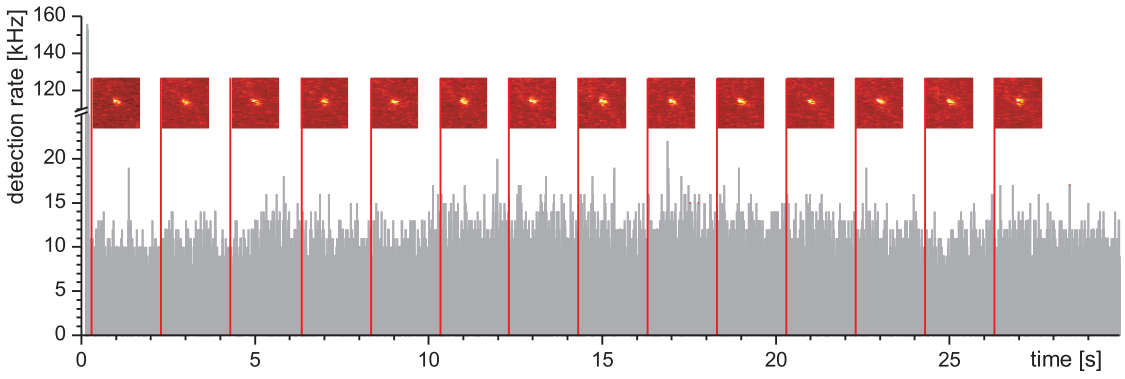

Figure 5.6: Single atom image series. We can take up to five images of the atom per second and create movies of it. With this we can check the atom's position multiple times within an experiment run.

6 Entanglement distribution between a trapped atom and two photons

To create entangled atom-photon states with our system, we implemented an extended version of the single photon production scheme. In chapter 4, we had the photon emitted into the cavity on a transition between two hyperfine-states without taking care of the Zeeman substates. Incorporating these Zeeman states couples each of the transitions to a certain photon polarization. Now the trick we use to create atom-photon entanglement is to give the atom exactly two possible decay channels into the cavity with equal transition energy but orthogonal polarization of the emitted photon. This way, the final Zeeman substate of the atom gets entangled with the polarization state of the emitted photon. Instead of just sending out a single photon which is not linked to the atom anymore, this scheme allows the distribution of quantum information (entangled states) over large distances. With the cavity efficiently collecting the photons emitted by the atom, we can, in a second step, map the atomic part of the entangled state onto the polarization of a second photon. The resulting entangled two-photon state can be verified by a measurement of the polarization states of two subsequently emitted photons. Proving the entanglement between the two photons also demonstrates a successful entanglement distribution from the prior atom-photon state to the two-photon state.

For the experimental realization of these entangled states and their characterization, the experimental apparatus had to meet quite some extra demands compared to the single photon source. First, it was necessary to change to the ^{87}Rb isotope to limit the number of Zeeman states to a minimum. Second, we now not only needed to detect the emitted photons, but we had to be able to perform a full quantum-state tomography on them. For the entanglement measurements, we are additionally very sensitive to the pump laser polarization, magnetic fields and differential Stark shifts induced by the trap, as they influence the individual temporal evolution of the atomic states involved in the entanglement.

In this chapter, I first introduce the entanglement scheme followed by a description of the experimental procedures and calibration measurements. For the characterization of the entanglement we made use of two methods, the measurement of a Bell inequality violation and a full quantum-state tomography. I will discuss these methods and present the measured results.

6.1 The entanglement protocol

For the creation of entangled atom-photon and photon-photon states, we use a protocol that is in principle deterministic. As we want to use , the scheme incorporates transitions between individual Zeeman substates and requires an atom with nuclear spin $I = 3/2$. This is why we have to use ^{87}Rb instead of ^{85}Rb, where we had a $I = 5/2$ system.

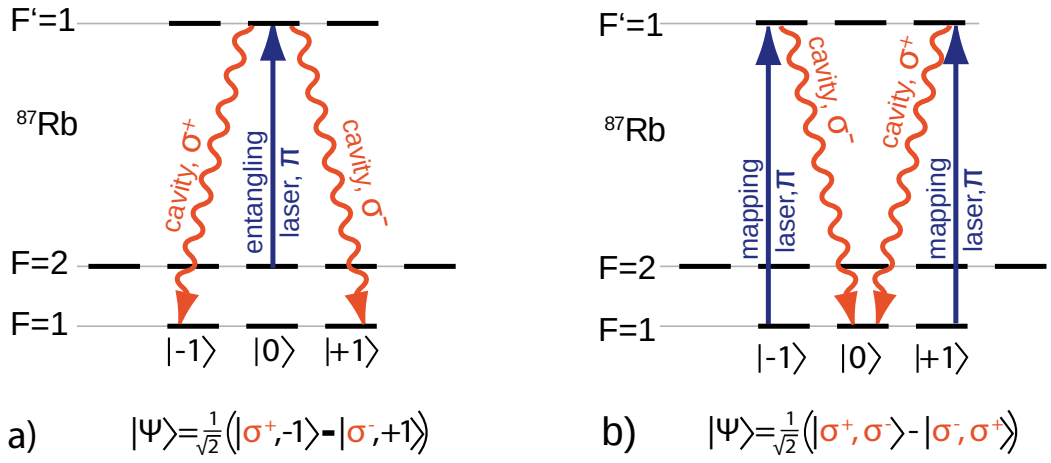

Figure 6.1: Atom-photon entanglement protocol. a) A single atom prepared in the $|\mathrm{F}, \mathrm{m_F}\rangle = |2, 0\rangle$ state emits a single photon during a vSTIRAP process driven by a laser pulse resonant with F=2 $\leftrightarrow$ F'=1 and the cavity tuned to F=1 $\leftrightarrow$ F'=1. As there are two orthogonal decay channels, the resulting atomic Zeeman state is entangled with the photon's polarization. b) The atomic part of the entangles state is mapped onto a second photon via another vSTIRAP process. The result is a two-photon Ψ^- Bell state.

For the entanglement scheme, we consider a single ^{87}Rb atom coupled to the cavity, which is frequency-locked to the F=1 $\leftrightarrow$ F'=1 transition. We define the cavity axis to be our quantization-axis, so the cavity supports only σ^-- and σ^+-transitions. The entanglement process is illustrated in figure 6.1A. In the beginning, the atom is in the F=2, m_F=0 ground state, which from now on we write as $|F, m_F\rangle = |2, 0\rangle$. This is achieved by optical pumping and is explained in the experimental results section. We now apply a π-polarized laser pulse resonant with the F=2 $\leftrightarrow$ F'=1 transition. Together with the cavity, this drives a *vacuum-stimulated Raman adiabatic passage* (vSTIRAP, see chapter 4) to the F=1 ground state. There are two energetically equivalent paths for this transition - one by decaying to the $|1, -1\rangle$ state while emitting a single σ^+-polarized photon from the cavity, and the other ending in the $|1, +1\rangle$ while emitting a σ^--polarized photon. This results in an entanglement of the atomic Zeeman substate with the polarization of the emitted photon. Taking the corresponding Clebsch-Gordan coefficients of the individual transitions into account, we find that the relative phase between the two possible paths is $e^{i\pi} = -1$ [82] and our entangled state reads

$$|\Psi_{\mathrm{AP}}\rangle = \frac{1}{\sqrt{2}}(|1, -1\rangle|\sigma^+\rangle - |1, +1\rangle|\sigma^-\rangle). \tag{6.1}$$

Having produced the entangled state, we need a method to verify it. There already have been experiments, where the photonic and the atomic state have been measured separately. In these experiments, shelving techniques were used where the atom undergoes a state-dependent transfer to a different state to be then detected via fluorescence light [42; 40]. But as the cavity efficiently collects photons emitted by the atom, we can instead map our atomic state onto a second photon. We do this by applying a second π-polarized pulse, this time resonant with the F=1 $\leftrightarrow$ F'=1 transition. This again drives a vSTIRAP sequence

and maps the atomic $|1,-1\rangle$ state onto a σ^--, and the $|1,+1\rangle$ state onto a σ^+-photon. At the same time, the atom is disentangled and ends in state $|1,0\rangle$. This process maps the atom-photon- onto a photon-photon-entanglement and the final state is

$$|\Psi_{\mathrm{APP}}\rangle = |1,0\rangle \otimes |\Psi^-_{\mathrm{PP}}\rangle = \frac{1}{\sqrt{2}}|1,0\rangle \otimes (|\sigma^+\rangle|\sigma^-\rangle - |\sigma^-\rangle|\sigma^+\rangle). \tag{6.2}$$

To verify the prior atom-photon entanglement, we now have to measure the states of the two photons emitted from the cavity. The two-photon entangled state $|\Psi^-_{PP}\rangle$ corresponds to the well-known maximally entangled Ψ^--state, one of the four "Bell states" [6]. As this measurement protocol is non-destructive (i.e. the atom is not lost), we can pump our atom back to the $|2,0\rangle$ and repeat the procedure for as long as the atom stays in the dipole trap.

Having a closer look at the details of the entanglement protocol, we find that the condition of a combined detection of the two photons makes it very robust, as photons from unsuccessful entanglement attempts are efficiently excluded from evaluation. While starting with an atom in the lower F=1 state will obviously not produce a photon during the first vSTIRAP pulse, the emission of two subsequent photons is even suppressed if the atom was prepared in any F=2 state other than $|2,0\rangle$. In this case, the only way to produce a first photon in the cavity mode would automatically end in the $|1,0\rangle$ state, for which the mapping process is a forbidden transition. So imperfections in the atom preparation will only reduce the overall efficiency of the protocol, but will not produce background two-photon events.

6.2 The EPR-paradox and Bell inequalities

J. S. Bell's famous theorem reduced the philosophical conflict between quantum mechanics and the classical concepts of causality and reality to the possible measurement of a single quantity [6]. A violation of a Bell inequality can refute the proposal of so-called "local hidden variables", as introduced by Einstein, Rosen, and Podolski in their classic paper of 1935 [83]. For this reason, a lot of experiments violating Bell inequalities have been carried out over the past four decades to prove the completeness of quantum mechanics and reject any local hidden variable theories. Secondary, Bell measurements are a convincing method to verify entangled states in experiments. We also performed a Bell measurement in the sense of proving entanglement in our system, as for tests on hidden variables our experiment does not meet certain crucial conditions.

To give an introduction to the topic, I loosely follow the manuscript of a talk given by A. Aspect at a conference in commemoration of John Bell in Vienna in 2000 [84]. We start considering our entangled two-photon state from the previous section, equation 6.2. We suppose that we send the two photons to remote locations and detect their polarization state independently. At these locations, we use polarizers with angles α and β respectively and two-channel detectors with outcomes $\uparrow$ and $\downarrow$. As the individual polarizations of the photons are not determined, the quantum-mechanical detection probabilities for the case

of detecting just one of the photons are then given as

$$\begin{aligned} p_\uparrow(\alpha) = p_\downarrow(\alpha) = 1/2, \\ p_\uparrow(\beta) = p_\downarrow(\beta) = 1/2. \end{aligned} \tag{6.3}$$

If we now consider the quantum-mechanical prediction for a joint detection of the two photons, we find

$$\begin{aligned} p_{\uparrow\uparrow}(\alpha,\beta) = p_{\downarrow\downarrow}(\alpha,\beta) = \frac{1}{2}\sin^2(\alpha-\beta), \\ p_{\uparrow\downarrow}(\alpha\beta) = p_{\downarrow\uparrow}(\alpha,\beta) = \frac{1}{2}\cos^2(\alpha-\beta). \end{aligned} \tag{6.4}$$

This result has some remarkable consequences. For the case of a parallel orientation of the polarizers ($\alpha - \beta = 0$) we find the detection probabilities

$$\begin{aligned} p_{\uparrow\uparrow}(\alpha,\alpha) = p_{\downarrow\downarrow}(\alpha,\alpha) &= 0, \\ p_{\uparrow\downarrow}(\alpha,\alpha) = p_{\downarrow\uparrow}(\alpha,\alpha) &= 1/2. \end{aligned} \tag{6.5}$$

This means, that whenever photon ν_1 is detected in one of the states $\uparrow$ and $\downarrow$, the detection of the other photon ν_2 will have an opposite result with certainty. Although the individual results are random, there is a total correlation for a joint detection.

To measure the extent of polarization correlations, a useful quantity is given by the correlation coefficient

$$E(\alpha,\beta) = p_{\downarrow\downarrow}(\alpha,\beta) + p_{\uparrow\uparrow}(\alpha,\beta) - p_{\uparrow\downarrow}(\alpha,\beta) - p_{\downarrow\uparrow}(\alpha,\beta) \tag{6.6}$$

With the quantum-mechanical predictions for the detection probabilities from equations 6.4, the correlation coefficient for our state is given by

$$E_{QM}(\alpha,\beta) = -\cos(2(\alpha-\beta)). \tag{6.7}$$

The interesting aspect here is that this result is independent of the spatial separation of the photons and whether their detection was coincident or not. So if the first photon is detected in a certain polarization state, the state of the second photon, indefinite until this exact moment, is projected onto the orthogonal polarization. The fact that this happens instantaneously seemingly conflicts with relativity as there is not necessarily a space-time connection between the two photons. This is known as the Einstein-Poldolski-Rosen (EPR) paradox and led to the proposal of so-called "local hidden variable" theories. These theories assume that quantum mechanics can not be considered as a complete theory and introduce additional parameters carrying the necessary information to explain the above results. Their conclusion is that measuring the state of a quantum-mechanical variable is equivalent to performing a statistical measurement of the hidden variables, or, in other words, quantum mechanics is a statistical mechanics description of a deeper level. Bell translated the problem into a mathematical formalism predicting that quantum mechanics shows certain properties that are contradictory to all local hidden variable theories.

Bell formalism

We introduce a supplementary parameter λ in our two-photon problem, carrying information about the real polarization state of the photons. An ensemble of such photon pairs is then specified by a probability distribution $\rho(\lambda)$ for the parameter values with

$$\begin{aligned} \rho(\lambda) &\geq 0, \\ \int d\lambda \rho(\lambda) &= 1. \end{aligned} \tag{6.8}$$

The result of a measurement on the photons is now defined by bivalent functions $A(\lambda, \alpha) = \pm 1$ at polarizer I of one detection setup and $B(\lambda, \beta) = \pm 1$ at polarizer II of the second setup. A particular "hidden variable" theory is completely defined by the explicit form of $\rho(\lambda)$, $A(\lambda, \alpha)$ and $B(\lambda, \beta)$.

The single and combined detection probabilities can be expressed in terms of these functions. We find for instance

$$\begin{aligned} p_{\uparrow}(\alpha) &= \int d\lambda \rho(\lambda) \frac{[1 + A(\lambda, \alpha)]}{2}, \quad \text{and} \\ p_{\uparrow\downarrow}(\alpha, \beta) &= \int d\lambda \rho(\lambda) \frac{[1 + A(\lambda, \alpha)]}{2} \frac{[1 - B(\lambda, \alpha)]}{2}. \end{aligned} \tag{6.9}$$

Similarly, the correlation coefficient $E(\alpha, \beta)$ can be written as the integral over the parameter distribution as

$$E(\alpha, \beta) = \int d\lambda \rho(\lambda)\ A(\lambda, \alpha)\ B(\lambda, \beta). \tag{6.10}$$

A simple example

As an example of a supplementary parameter theory, we now consider a simple model based on the two photons from above with orthogonal polarization. We use the supplementary parameter λ to label the polarization direction of photon ν_1 which implicitly labels photon ν_2 to have a polarization of $\lambda + \pi/2$. We assume the probability distribution of the supplementary parameter λ to be rotationally invariant with

$$\rho(\lambda) = \frac{1}{2\pi}, \tag{6.11}$$

which means we do not choose any specific polarization basis for the photons. We specify the explicit form of the functions $A(\lambda, \alpha)$ and $B(\lambda, \beta)$ as:

$$\begin{aligned} A(\lambda, \alpha) &= \text{sign}\{\cos\ 2(\alpha - \lambda)\} \\ B(\lambda, \beta) &= \text{sign}\{\cos\ 2(\beta - \lambda - \pi/2)\}. \end{aligned} \tag{6.12}$$

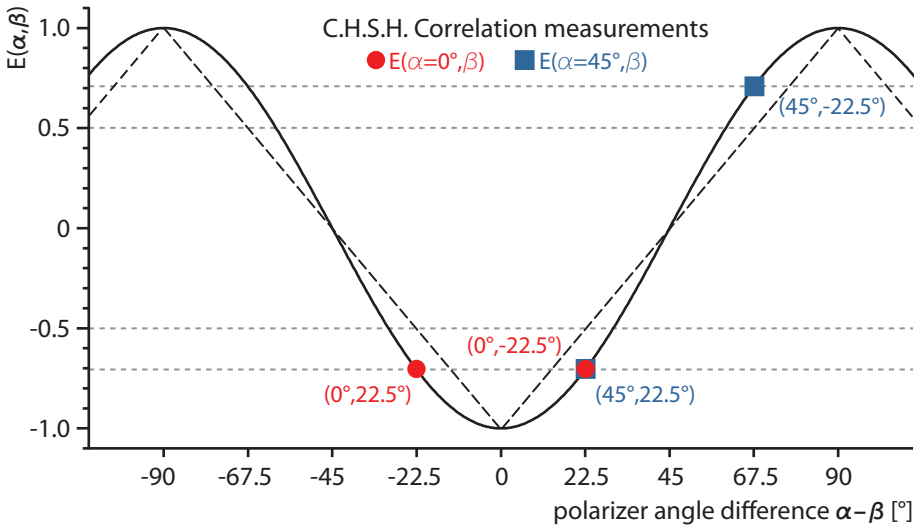

Figure 6.2: Correlation measurements used to demonstrate the violation of a Bell inequality as proposed by C.H.S.H. On a set of two-photon Ψ^- Bell-states, we measure correlation coefficients $E(\alpha, \beta)$ for four combinations of polarizations (circles and squares), each with a theoretical absolute value of $\sqrt{2}/2 \approx 0.707$, following the prediction of quantum mechanics (solid line). Together, they can violate the classical limit (indicated with the dashed line) of 2 with a Bell-Signal as large as $2\sqrt{2}$.

This choice is reasonable as we always get detection events with opposite sign for parallel polarizers and coincident results if we rotate one of the polarizers by 90 ° according to the orthogonal polarization of the two photons. Using equations 6.9 and mapping the results of the above functions ± 1 to our detection events $\uparrow$ and $\downarrow$ we find single probabilities

$$p_\uparrow(\alpha) = p_\downarrow(\alpha) = p_\uparrow(\beta) = p_\downarrow(\beta) = \frac{1}{2}, \tag{6.13}$$

identical with the quantum-mechanical predictions. For the joint detection, the correlation coefficient is given by

$$E(\alpha, \beta) = \frac{4}{\pi}|\alpha - \beta| - 1, \tag{6.14}$$

$$\text{for} \quad -\pi/2 \leq \alpha - \beta \leq \pi/2, \tag{6.15}$$

which only depends on the relative angle between the two polarizers. In figure 6.2 the result of this simple model is compared to that derived from quantum mechanics. Although the correlation coefficient $E(\alpha, \beta)$ of the simple model is already quite close, Bell showed that there is no way to further approach the quantum-mechanical prediction. As we will see, the difference between these two curves sets the basis to the experimental violation of Bell inequalities.

The C.S.H.S. Bell inequality

The formulation of the Bell inequality we use here is a generalized version published by Clauser, Horne, Shimony, and Holt [85], which is directly applicable to experiments. We take a combination of polarizer angles α, α' and β, β' and consider the quantity

$$s = A(\lambda,\alpha)B(\lambda,\beta) - A(\lambda,\alpha)B(\lambda,\beta') + A(\lambda,\alpha')B(\lambda,\beta) + A(\lambda,\alpha')B(\lambda,\beta'), \tag{6.16}$$

which will take the values

$$s(\lambda,\alpha,\alpha',\beta,\beta') = \pm 2, \tag{6.17}$$

as A and B only take values ± 1. The integral over the λ space is then limited to

$$-2 \leq \int d\lambda \rho(\lambda) s(\lambda,\alpha,\alpha',\beta,\beta') \leq 2. \tag{6.18}$$

With the definition of

$$S(\alpha,\alpha',\beta,\beta') \equiv |E(\alpha',\beta') - E(\alpha,\beta')| + |E(\alpha',\beta) + E(\alpha,\beta)| \leq 2, \tag{6.19}$$

and the use of equation 6.10, we find that this combination of four correlation coefficients is limited within

$$S(\alpha,\alpha',\beta,\beta') \leq 2 \tag{6.20}$$

for any hidden variable theory. Looking at the quantum-mechanical prediction in figure 6.2, we see that many of the possible combinations of polarizer angles result in a value for S exceeding the limit of 2. Especially for the choice of $\alpha = 0°$, $\alpha' = 45°$, $\beta = 22.5°$ and $\beta' = -22.5°$ the violation of the inequality can be maximized and S takes the theoretical value of $2\sqrt{2}$. We can conclude that if a measurement of polarization correlations in these four detection basis combinations shows a result of $S > 2$, this can only be explained by a measurement on a quantum-mechanical entangled state.

In the past decades, numerous experiments have shown Bell inequality violations with increasing precision and steadily approaching the ideal "gedanken-experiment" of John Bell, which sets strict conditions that are hard to fulfill all at the same time. These conditions are

- **Closing of the locality loophole.** This requires a strict relativistic separation between the detection events of the two photons. This means that their temporal and spatial distance has to be chosen such that no information exchange between the detectors about the first measurement can influence the result of the second one.
- **Strict Einstein locality conditions.** This even stricter separation of the two measurements also includes the analyzer orientations to be set during the flight of the particles, avoiding prior information exchange on the analyzer angles. Additionally, data recording should also happen in a separated way.
- **Closing of the detection loophole.** Low detection efficiencies could allow the possibility that the subensemble of detected events agrees with quantum mechanics even though the entire ensemble would satisfy Bell's inequalities. This loophole can be closed with a highly efficient detection scheme.

So far, all the loopholes have been closed, but not all at a time or with the same experiment. Concerning the locality, impressive experiments with photon pairs detected at large distances of several kilometers were carried out for example in Malvern [86] and Geneva [87]. An experiment by Weihs in Innsbruck was even able to show a Bell inequality violation under strict Einstein locality conditions [88]. The detection loophole requiring a high detection efficiency and a deterministic preparation of the entangled state, was closed by two experiments until now. Both were carried out with trapped ion systems, one with two ions in the same trap [89], the other with a separation of about a meter between the two ions [90].

With the experimental apparatus discussed in this thesis, none of the requirements for testing hidden variable theories are fulfilled, as the two photons are both detected in the same detection setup with an efficiency of about 20%. Nevertheless, with the assumption that quantum mechanics is a valid theory, showing a violation of a Bell inequality is a very convincing method to prove the entanglement created in our protocol.

6.3 Two-photon quantum-state tomography

A quantum-state tomography is very similar to its classical counterpart, where a three-dimensional object is scanned along the different spatial directions and is then reconstructed from the measured projections. In the commonly accepted interpretation of quantum mechanics, a measurement on a quantum state $|\Psi\rangle$ leads to a collapse of the original wave function. What we measure when the detector signals a detection event, is a projection onto a certain detection state $|\chi\rangle$ defined by the detection conditions chosen by the experimenter. To characterize a quantum state, one therefore has to perform a series of measurements on identically prepared states detected in different measurement bases. From the statistical probabilities of detection events in these bases, the original quantum state can then be reconstructed. To discuss the measurement procedure of the two-photon state tomography, we now mainly follow the description in [91].

Characterization of light polarization

The Irish mathematician and physicist Sir George Gabriel Stokes was probably the first to publish a method to fully determine the polarization of a light beam in 1852 [92]. He defined a set of four parameters, the Stokes-parameters, which can be measured in a series of four independent experiments, where the light is detected using:

0. a filter with a polarization-independent transmission of 50%.
1. a linear horizontal polarizer.
2. a linear polarizer at 45 °.
3. a polarizer transmitting right-circular light only.

While Stokes had to measure light intensities at his time, our detectors in the experiment count single photon detection events. As we are interested in the polarization of single photons, we define now different measurement bases as quantum-mechanical states in the bra-ket-formalism:

state definition	polarization
$\|H\rangle$	linear horizontal
$\|V\rangle$	linear vertical
$\|D\rangle = (\|H\rangle + \|V\rangle)/\sqrt{2}$	linear diagonal (45 °)
$\|A\rangle = (\|H\rangle - \|V\rangle)/\sqrt{2}$	linear "anti"-diagonal (−45 °)
$\|R\rangle = (\|H\rangle + i\|V\rangle)/\sqrt{2}$	right circular
$\|L\rangle = (\|H\rangle - i\|V\rangle)/\sqrt{2}$	left circular

In this vector formalism, the polarization state is represented by a 2×2 matrix ρ. Normalizing on the detection rates obtained in the experiments, we can write the results of our four measurements as:

$$\begin{aligned} n_0 &= \frac{1}{2}\left(\langle H|\rho|H\rangle + \langle V|\rho|V\rangle\right) = \frac{1}{2}\left(\langle R|\rho|R\rangle + \langle L|\rho|L\rangle\right) \\ n_1 &= \langle H|\rho|H\rangle = \frac{1}{2}\left(\langle R|\rho|R\rangle + \langle L|\rho|L\rangle + \langle R|\rho|L\rangle + \langle L|\rho|R\rangle\right) \\ n_2 &= \langle D|\rho|D\rangle = \frac{1}{2}\left(\langle R|\rho|R\rangle + \langle L|\rho|L\rangle - i\langle L|\rho|R\rangle + i\langle R|\rho|L\rangle\right) \\ n_3 &= \langle R|\rho|R\rangle. \end{aligned} \tag{6.21}$$

With these detection probabilities, we can specify the normalized Stokes-Parameters, which completely describe the polarization of a light state:

$$\begin{aligned} \mathcal{S}_0 &\equiv 2n_0' = \left(\langle R|\rho|R\rangle + \langle L|\rho|L\rangle\right) = \mathrm{tr}(\rho)\,, \\ \mathcal{S}_1 &\equiv 2\left(n_1' - n_0'\right) = \left(\langle R|\rho|L\rangle + \langle L|\rho|R\rangle\right), \\ \mathcal{S}_2 &\equiv 2\left(n_2' - n_0'\right) = i\left(\langle R|\rho|L\rangle - \langle L|\rho|R\rangle\right), \\ \mathcal{S}_3 &\equiv 2\left(n_3' - n_0'\right) = \left(\langle R|\rho|R\rangle - \langle L|\rho|L\rangle\right). \end{aligned} \tag{6.22}$$

As our density matrix is normalized, we know that $\mathrm{tr}(\rho) = 1$, which means that $\mathcal{S}_0 = 1$. To transfer our results into a matrix formalism, we take a complete basis set of 2×2-matrices consisting of the unity-matrix σ_0 and the well-known Pauli spin matrices $\{\sigma_{1,2,3}\}$ obeying the algebra

$$\begin{aligned} \sigma_i\sigma_j &= \delta_{ij} + i\varepsilon_{ijk}\sigma_k, \\ [\sigma_i, \sigma_j] &= 2i\varepsilon_{ijk}\sigma_k. \end{aligned} \tag{6.23}$$

If we write our basis of orthonormal polarization states as $|R\rangle = (1\ 0)^T$ and $|L\rangle = (0\ 1)^T$ we find that

$$\begin{aligned}
\sigma_0 &= |R\rangle\langle R| + |L\rangle\langle L| = \begin{pmatrix} 1 & 0 \\ 0 & 1 \end{pmatrix}, \\
\sigma_1 &= |R\rangle\langle L| + |L\rangle\langle R| = \begin{pmatrix} 0 & 1 \\ 1 & 0 \end{pmatrix}, \\
\sigma_2 &= i\left[|L\rangle\langle R| - |R\rangle\langle L|\right] = \begin{pmatrix} 0 & -i \\ i & 0 \end{pmatrix}, \\
\sigma_3 &= |R\rangle\langle R| - |L\rangle\langle L| = \begin{pmatrix} 1 & 0 \\ 0 & -1 \end{pmatrix}.
\end{aligned} \tag{6.24}$$

Now we can simply construct our density matrix ρ as a combination of the Stokes-parameters and the matrices σ_i as

$$\rho = \frac{1}{2}\sum_{i=0}^{3} \mathcal{S}_i \sigma_i. \tag{6.25}$$

or, in the reversed direction,

$$\mathcal{S}_i = \mathrm{tr}(\sigma_i \rho)\,. \tag{6.26}$$

This means, a measurement of the Stokes-parameters constitutes a full tomography of the density matrix ρ of a polarization state.

Tomography of a single qubit state

The results found in the previous section are not only valid for the choice of a certain basis. We can generalize this such that every choice of orthogonal states $|\Psi\rangle$ and $|\Psi^{\perp}\rangle$ can be associated with the two qubit states $(1\ 0)^T$ and $(0\ 1)^T$. The rewritten equation 6.26

$$\mathcal{T}_i = \mathrm{tr}(\sigma_i \rho) \tag{6.27}$$

now describes the results of projection measurements

$$\begin{aligned}
\mathcal{T}_0 &= p_{|\psi\rangle} + p_{|\psi^{\perp}\rangle} = 1, \\
\mathcal{T}_1 &= p_{\frac{1}{\sqrt{2}}(|\psi\rangle + |\psi^{\perp}\rangle)} - p_{\frac{1}{\sqrt{2}}(|\psi\rangle - |\psi^{\perp}\rangle)}, \\
\mathcal{T}_2 &= p_{\frac{1}{\sqrt{2}}(|\psi\rangle + i|\psi^{\perp}\rangle)} - p_{\frac{1}{\sqrt{2}}(|\psi\rangle - i|\psi^{\perp}\rangle)}, \\
\mathcal{T}_3 &= p_{|\psi\rangle} - p_{|\psi^{\perp}\rangle},
\end{aligned} \tag{6.28}$$

where $p_{|\psi\rangle}$ denotes the probability of measuring state $|\psi\rangle$. The parameters $\{\mathcal{T}_i\}$ are defined with reference to the states

$$\begin{aligned}
|\Phi_1\rangle &= \frac{1}{\sqrt{2}}\left(|\psi\rangle + |\psi^{\perp}\rangle\right) \\
|\Phi_2\rangle &= \frac{1}{\sqrt{2}}\left(|\psi\rangle + i|\psi^{\perp}\rangle\right) \\
|\Phi_3\rangle &= |\psi\rangle
\end{aligned} \tag{6.29}$$

With this we can write the $\{\mathcal{T}_i\}$ in a compact way as

$$\begin{aligned} \mathcal{T}_{i=1,2,3} &= p_{|\Phi_i\rangle} - p_{|\Phi_i^\perp\rangle} \\ \mathcal{T}_0 &= p_{|\psi\rangle} + p_{|\psi^\perp\rangle} = 1,\ \forall\ |\psi\rangle, \end{aligned} \tag{6.30}$$

and the density matrix reads

$$\rho = \frac{1}{2}\sum_{i=0}^{3} \mathcal{T}_i \sigma_i = \frac{1}{2}\left(1 + \sum_{i=1}^{3} \mathcal{T}_i \left(|\phi_i\rangle\langle\phi_i| - |\phi_i^\perp\rangle\langle\phi_i^\perp|\right)\right). \tag{6.31}$$

For a measurement on an ensemble in a pure state, we find $\mathrm{tr}\left(\rho^2\right) = 1$, which can be simplified to $\sum_{i=1}^{3} \mathcal{T}_i^2 = 1$ using $\mathcal{T}_0 = 1$ and equations 6.23. If we measure on an ensemble consisting of multiple pure states or if the individual objects of the ensemble are not in pure states, we have $\mathrm{tr}\left(\rho^2\right) < 1$ and, accordingly $\sum_{i=1}^{3} \mathcal{T}_i^2 < 1$.

Tomography of a two-photon state

We can now expand our system to the case of a two-qubit system, where the density matrix

$$\rho = \frac{1}{4}\sum_{i_1,i_2=0}^{3} r_{i_1,i_2}\, \sigma_{i_1} \otimes \sigma_{i_2} \tag{6.32}$$

with parameters r_{i_1,i_2} being real numbers describes our entangled state. As the normalization of the matrix ($\mathrm{tr}(\rho) = 1$) requires $r_{0,0} = 1$, we are left with 15 free parameters. Analog to the tomography of a single qubit, where we had to measure the state in 4 different projections $\{\sigma_i\}$, we can determine a state consisting of two qubits by 16 projection measurements $\sigma_i \otimes \sigma_j, (i,j = 0,1,2,3)$. Accordingly, the $\{\mathcal{T}_i\}$ defined in equation 6.27 in combination with the density matrix of 6.32 expand to

$$\begin{aligned} \mathcal{T}_{i_1,i_2} &= \mathrm{tr}((\sigma_{i_1} \otimes \sigma_{i_2})\,\rho) \\ &= \frac{1}{4}\sum_{j_1,j_2=0}^{3} r_{j_1,j_2} \mathrm{tr}\{\sigma_{i_1}\sigma_{j_1}\}\mathrm{tr}\{\sigma_{i_2}\sigma_{j_2}\} \\ &= r_{i_1,i_2}, \end{aligned} \tag{6.33}$$

as we have $\mathrm{tr}\{\sigma_i\sigma_j\} = 2\delta_{ij}\ \forall\, i,j \in \{0,1,2,3\}$. Expressed in the $|\Phi_i\rangle$-states, the $\{\mathcal{T}_{i_1,i_2}\}$ now read, in analogy to what we had in equations 6.30:

$$\mathcal{T}_{i_1,i_2} = \left(p_{|\Phi_{i_1}\rangle} \pm p_{|\Phi_{i_1}^\perp\rangle}\right) \otimes \left(p_{|\Phi_{i_2}\rangle} \pm p_{|\Phi_{i_2}^\perp\rangle}\right). \tag{6.34}$$

In this representation, the + sign is used, whenever the indices i_1 or i_2 of the corresponding probabilities P is 0. For the case of $i_1 \neq 0$ and $i_2 \neq 0$, equation 6.34 can be reduced to

$$\begin{aligned} \mathcal{T}_{i_1,i_2} &= \left(p_{|\Phi_{i_1}\rangle} - p_{|\Phi_{i_1}^\perp\rangle}\right) \otimes \left(p_{|\Phi_{i_2}\rangle} - p_{|\Phi_{i_2}^\perp\rangle}\right) \\ &= p_{|\Phi_{i_1}\rangle|\Phi_{i_2}\rangle} - p_{|\Phi_{i_1}\rangle|\Phi_{i_2}^\perp\rangle} - p_{|\Phi_{i_1}^\perp\rangle|\Phi_{i_2}\rangle} + p_{|\Phi_{i_1^\perp}\rangle|\Phi_{i_2^\perp}\rangle}. \end{aligned} \tag{6.35}$$

Using equation 6.33, the two-qubit density matrix can be written in terms of the $\mathcal{T}_{i_1,i_2}$ as

$$\rho = \frac{1}{4} \sum_{i_1,i_2=0}^{3} \mathcal{T}_{i_1,i_2}\, \sigma_{i_1} \otimes \sigma_{i_2}. \tag{6.36}$$

Density matrix reconstruction from a series of measurements

In the following, a possible series of measurements to determine the parameters $\{\mathcal{T}_{i_1,i_2}\}$ for a two-photon entangled state is given. This is also the basis of the experimental results described later in this chapter. The $|\Phi_i\rangle$-states and their orthogonal complements are assigned to polarization states as

$$\begin{aligned}
|\phi_1\rangle &= |H\rangle = (|R\rangle + |L\rangle)/\sqrt{2} \\
|\phi_1^{\perp}\rangle &= |H^{\perp}\rangle = |V\rangle = (|R\rangle - |L\rangle)/\sqrt{2} \\
|\phi_2\rangle &= |D\rangle = (|R\rangle + i|L\rangle)/\sqrt{2} \\
|\phi_2^{\perp}\rangle &= |D^{\perp}\rangle = |A\rangle = (|R\rangle - i|L\rangle)/\sqrt{2} \\
|\phi_3\rangle &= |R\rangle \\
|\phi_3^{\perp}\rangle &= |R^{\perp}\rangle = |L\rangle
\end{aligned} \tag{6.37}$$

For the full state tomography, we combine these to 9 different measurement bases. This results in 36 measurement results which can be described using equation 6.35. From these, we obtain 9 independent $\{\mathcal{T}_{i_1,i_2}\}$ as

$$\begin{aligned}
\mathcal{T}_{1,1} &= p_{HH} - p_{HV} - p_{VH} + p_{VV} \\
\mathcal{T}_{1,2} &= p_{HD} - p_{HA} - p_{VD} + p_{VA} \\
\mathcal{T}_{1,3} &= p_{HR} - p_{HL} - p_{VR} + p_{VL} \\
\mathcal{T}_{2,1} &= p_{DH} - p_{DV} - p_{AH} + p_{AV} \\
\mathcal{T}_{2,2} &= p_{DD} - p_{DA} - p_{AD} + p_{AA} \\
\mathcal{T}_{2,3} &= p_{DR} - p_{DL} - p_{AR} + p_{AL} \\
\mathcal{T}_{3,1} &= p_{RH} - p_{RV} - p_{LH} + p_{LV} \\
\mathcal{T}_{3,2} &= p_{RD} - p_{RA} - p_{LD} + p_{LA} \\
\mathcal{T}_{3,3} &= p_{RR} - p_{RL} - p_{LR} + p_{LL},
\end{aligned} \tag{6.38}$$

while the remaining 6 are depending on the same measurement results. With equation 6.34 we get

$$\begin{aligned}
\mathcal{T}_{0,1} &= p_{HH} - p_{HV} + p_{VH} - p_{VV} \\
\mathcal{T}_{0,2} &= p_{DD} - p_{DA} + p_{AD} - p_{AA} \\
\mathcal{T}_{0,3} &= p_{RR} - p_{RL} + p_{LR} - p_{LL} \\
\mathcal{T}_{1,0} &= p_{HH} + p_{HV} - p_{VH} - p_{VV} \\
\mathcal{T}_{2,0} &= p_{DD} + p_{DA} - p_{AD} - p_{AA} \\
\mathcal{T}_{3,0} &= p_{RR} + p_{RL} - p_{LR} - p_{LL}.
\end{aligned} \tag{6.39}$$

The choice of the same basis for components with index 0 and for those with index i is not unique. Because of $p_{|H\rangle} + p_{|V\rangle} = p_{|D\rangle} + p_{|A\rangle} = p_{|R\rangle} + p_{|L\rangle}$, we could, for example, also write $\mathcal{T}_{0,1}$ as

$$\begin{aligned}\mathcal{T}_{0,1} &= \frac{1}{3}\left[\left(p_{|H\rangle} + p_{|V\rangle}\right) + \left(p_{|D\rangle} + p_{|A\rangle}\right) + \left(p_{|R\rangle} + p_{|L\rangle}\right)\right] \otimes \left(p_{|H\rangle} - p_{|V\rangle}\right) \\ &= \frac{1}{3}\left(p_{HH} - p_{HV} + p_{VH} - p_{VV}\right) \\ &+ \frac{1}{3}\left(p_{DH} - p_{DV} + p_{AH} - p_{AV}\right) \\ &+ \frac{1}{3}\left(p_{RH} - p_{RV} + p_{LH} - p_{LV}\right).\end{aligned} \tag{6.40}$$

This means, we can incorporate a lot more measured data to determine $\mathcal{T}_{0,1}$ and reduce statistical errors. With the use of equation 6.36 and $\mathcal{T}_{0,0} = 1$, we can now reconstruct the full density matrix from the measurement results.

6.4 Entanglement measures

While the density matrix contains all possible information about a given state, it is quite useful to define a single quantity that measures the amount of entanglement contained in a given state. Such an entanglement measure is usually a positive, monotone and additive quantity with a value between 0 and 1. To evaluate our measured density matrices, we calculate some of the most popular measures, which are briefly defined here. A more detailed description of entanglement measures can be found in [93].

Entanglement of Formation and Concurrence

The *Entanglement of Formation* is an entanglement measure introduced by Hill and Wootters [94; 95], representing the minimal possible average entanglement over all pure-state decompositions of a given state ρ. For its definition, we first define the entropy of entanglement for a pure state $|\Psi\rangle$ as

$$E\left(|\Psi_i\rangle\langle\Psi_i|\right) := S\left(\mathrm{tr}_A\left\{|\Psi_i\rangle\langle\Psi_i|\right\}\right) = S\left(\mathrm{tr}_B\left\{|\Psi_i\rangle\langle\Psi_i|\right\}\right), \tag{6.41}$$

with S being the *von Neumann entropy* $S(\rho) = -\mathrm{tr}[\rho \log_2 \rho]$ and tr_B the partial trace over subsystem B of the state. Using this measure of entanglement for pure states, the Entanglement of Formation E_F is defined as

$$E_F(\rho) := \inf\left\{\sum_i p_i E\left(|\Psi_i\rangle\langle\Psi_i|\right) \;:\; \rho = \sum_i p_i |\Psi_i\rangle\langle\Psi_i|\right\} \tag{6.42}$$

For a general state ρ, the variational problem that defines E_F usually can only be solved using numerical techniques. Nevertheless, for bipartite states a closed solution is known

[96], which is based on the calculation of the *Concurrence*. The Concurrence for a two-qubit system is obtained from the density matrix ρ defining the non-hermite matrix

$$R = \rho\Sigma\rho^T\Sigma, \tag{6.43}$$

with

$$\Sigma = \begin{pmatrix} 0 & 0 & 0 & -1 \\ 0 & 0 & 1 & 0 \\ 0 & 1 & 0 & 0 \\ -1 & 0 & 0 & 0 \end{pmatrix} \tag{6.44}$$

and calculating the eigenvalues of R. After sorting them such that $r_1 \geq r_2 \geq r_3 \geq r_4$, the Concurrence is given by

$$C = \max\{0, \sqrt{r_1} - \sqrt{r_2} - \sqrt{r_3} - \sqrt{r_4}\}. \tag{6.45}$$

The closed solution for E_F for any bipartite qubit state now has been proven to be

$$E_F(\rho) = s(\frac{1 + \sqrt{1 - C^2(\rho)}}{2}) \tag{6.46}$$

with

$$s(x) = -x\log_2(x) - (1-x)\log_2(1-x). \tag{6.47}$$

While the Entanglement of formation is really an entanglement measure, the Concurrence obtains its meaning via its relation to E_F. For higher dimensional systems, this connection breaks down. Although the Concurrence is sometimes used to characterize entanglement, giving the Entanglement of Formation would be a better choice. For a bipartite state, C and E_F both map the entanglement contained in the density matrix ρ on the interval $[0, 1]$ with a value of 1 representing a maximally entangled state.

Negativity and Logarithmic Negativity

Compared to the Entanglement of Formation, the *Negativity* $N(\rho)$ is an entanglement measure that is in general a lot easier to compute. This made it quite popular to describe experimental entanglement results. $N(\rho)$ is a convex entanglement monotone that attempts to quantify the negativity in the spectrum of the partial transpose of the density matrix. Given a bipartite state ρ_{AB} expanded in a given orthonormal basis as

$$\rho = \sum_{i,j,k,l} \rho_{ij,kl}|i\rangle\langle j| \otimes |k\rangle\langle l|, \tag{6.48}$$

the partial transpose with respect to party B is defined as

$$\rho^{T_B} := \sum_{i,j,k,l} \rho_{ij,kl}|i\rangle\langle j| \otimes |l\rangle\langle k|. \tag{6.49}$$

While for a separable state this partial transpose is always positive, negative values indicate entanglement in the state. Using the trace norm $\|X\| := \mathrm{tr}\sqrt{X^\dagger X}$, the Negativity is defined as

$$N(\rho) := \frac{\|\rho^{T_B}\| - 1}{2}. \tag{6.50}$$

This quantity is zero for any unentangled state and has positive values if entanglement is contained. For the two-photon Ψ^- Bell state considered in our experiments, the maximum value is $N = 0.5$. As the Negativity itself is not additive, one can define a new measure

$$E_N(\rho) := \log_2 \|\rho^{T_B}\|, \tag{6.51}$$

which is called the *Logarithmic Negativity*. It is now additive by construction but fails to be convex.

Fidelity with an entangled state

The *Fidelity* F is widely used to characterize entangled states, nevertheless is it not really a measure of entanglement. It is rather a comparison of your test state to a state with known properties. It is defined as

$$F(\rho_1, \rho_2) = \left[\mathrm{tr}\left(\sqrt{\sqrt{\rho_1}\rho_2\sqrt{\rho_1}}\right)\right]^2 \tag{6.52}$$

and calculates the overlap of two states represented by ρ_1 and ρ_2. The Fidelity therefore can tell you how close your measured density matrix ρ_2 is to a pure maximally entangled state. For a two-qubit system, this could be one of the four Bell-states [6]:

$$\begin{aligned} |\phi^\pm\rangle &= \frac{1}{\sqrt{2}}\left(|HH\rangle \pm |VV\rangle\right) \\ |\psi^\pm\rangle &= \frac{1}{\sqrt{2}}\left(|HV\rangle \pm |VH\rangle\right). \end{aligned} \tag{6.53}$$

For the case of the entanglement measurements described in this thesis, our reference state corresponds to the $|\Psi^-\rangle$ Bell-state:

$$|\Psi^-\rangle = \frac{1}{\sqrt{2}}\left(|\sigma^+\sigma^-\rangle - |\sigma^-\sigma^+\rangle\right). \tag{6.54}$$

While the Fidelity with this state has a range of $[0, 1]$, values of $F > 0.5$ can only be explained by quantum entanglement. However, a decrease of F, e.g. during a temporal evolution of the state, does not automatically mean that the entanglement is lost, as the state could for example rotate into another Bell-state. To maintain its meaning as an entanglement measure, one could at every point in time find the closest maximally entangled state by maximizing the value of F. So the choice of the state we compare our results to gives the Fidelity its relevance as an entanglement measure.

6.5 Implementation and calibration measurements

I will now describe the implementation of the protocol in the experiment. In addition to the change of the Rb isotope, quite a few changes had to be made to the existing apparatus. The entanglement protocol required a different pump laser setup, an effective reduction of the residual magnetic field in the cavity, full Stark shift compensation and a new detection setup for the state tomography. The results of the individual calibrations depend on the degree of optimization achieved with the respective other calibrations. So the actual process of preparing the system for the measurements consisted in repeated application of the different calibration procedures.

6.5.1 Laser configuration and cooling scheme adaptation

For all previous experiments performed with this apparatus, the polarization of the pump laser was not explicitly defined. All pump lasers had been applied as an intensity-balanced, counter-propagating pair of lin $\perp$ lin polarized laser beams. This configuration was chosen to avoid interference structures along the beams, which would lead to spatially inhomogeneous Rabi frequencies. All needed laser frequencies were coupled to the same fiber and the fiber output was oriented such that the light was focused on the atoms through the top viewport under an angle of 45 degrees. After traversing the vacuum chamber, the light was recollimated and retroreflected back to the atoms, with a polarization rotated by 90 ° after passing the same $\lambda/4$-plate twice.

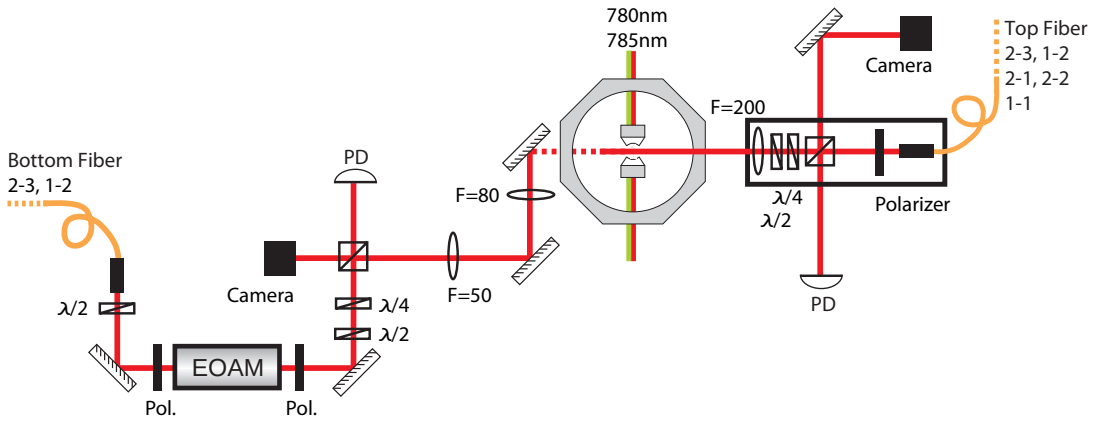

Figure 6.3: Pump laser configuration. The fiber coming from the top of the apparatus contains all five laser frequencies necessary for the entanglement protocol. The light from the lower fiber is only applied to balance the light pressure of those used for the cooling scheme. The polarization of the beams is determined by polarizers and wave plates after the fiber couplers and the beam intensity can be balanced via the voltage of an EOM.

The entanglement scheme now requires that the lasers used for optical pumping, entangling, and mapping pulses are π-polarized with respect to the cavity axis. Nevertheless, it seemed useful to keep the lin $\perp$ lin configuration with the two counterpropagating beams for all cooling purposes where many photons are scattered and thus balanced light pressure is necessary. Fortunately, those laser frequencies where the π-polarization now becomes important are different from those needed for the cooling. To meet all requirements, the retroreflection setup was replaced by a second optical fiber delivering all pump light for the cooling to the bottom viewport of the vacuum chamber (see figure 6.3). The fiber coming from the top contains all frequencies for cooling and the entanglement scheme. Its output is defined to be π-polarized with respect to the cavity axis using a polarizer at the fiber output and a combination of half-wave- and quarter-wave plate to correct birefringence of the viewport. Both, the top and the bottom pump laser beams are focused in the cavity with expected beam waists of about 70 μm FWHM. The following table summarizes the available pump lasers.

Top pump lasers π-polarized	Bottom pump lasers $\perp$ to top pump
F=2 $\leftrightarrow$ F'=3	F=2 $\leftrightarrow$ F'=3
F=1 $\leftrightarrow$ F'=2	F=1 $\leftrightarrow$ F'=2
F=2 $\leftrightarrow$ F'=2	
F=2 $\leftrightarrow$ F'=1	
F=1 $\leftrightarrow$ F'=1	

A fraction of the top pump light can also be coupled into the cavity, allowing to lock the cavity frequency to any of the above transitions. This is useful e.g. for the optimization of the optical pumping process (see section 6.5.5). The only disadvantage of the new setup is the intensity balance of the two beams, which has to be readjusted whenever the fiber coupling efficiencies drift. An EOM in the optical path of the lower pump beam can therefore be used to adjust the relative intensities of the two beams. This is usually done optimizing the atom trapping times. As the settings for good trapping performance showed differences up to a factor of 4 in the total power of the two pump beams, we conclude that the foci of the pump beams are not at exactly the same place. Nevertheless, within our optimization attempts, this configuration showed the best results.

As the cavity has to be locked to the F=1 $\leftrightarrow$ F'=1 transition for the entanglement protocol, it seemed quite logical to adapt the cavity-cooling scheme described in chapter 3 to the new situation. Unfortunately, the Sisyphus force will on average heat the atoms when the pump lasers are near-resonant with the Stark-shifted transitions, as required for the entanglement sequence. With this force counteracting the cavity cooling, the tested scheme simply did not satisfy the expectations. It was not possible to achieve acceptable trapping times using just a F=1 $\leftrightarrow$ F'=1 laser and repumpers. As a solution, we passed on the use of cavity cooling and relied on the Sisyphus-like cooling mechanism established in the previous experiments. For this, we use a laser tuned to the undisturbed closed F=2 $\leftrightarrow$ F'=3 transition, which is, due to the Stark shift from the trap, far-detuned from the real atomic resonance. With this light-pressure balanced laser and an additional repump laser on the F=1 $\leftrightarrow$ F'=2, we achieved trapping times of the same order as in

the single-photon experiments. To still have a signal from the cavity which allows us to monitor the presence of the trapped atom, we added a weak ($\approx 0.2\,\mu$W) laser resonant with $F{=}1 \leftrightarrow F'{=}1$ to scatter some photons into the cavity.

6.5.2 Detection setup

At the output of the cavity, the emitted photons are coupled to an optical fiber and directed to a new detection apparatus. It consists of four single-photon counting modules (SPCM) constituting two detection setups. Each of them is capable of measuring the photons in an individually definable polarization basis at the two output ports of a polarizing beam splitter (PBS). As the detection optics was installed and aligned mainly by our diploma student Tobias Müller, most of the numbers given in this section are taken from his thesis [80].

The photons emitted from the cavity are mode-matched to couple into the fiber with an efficiency of $> 70\%$. The 10 m long single mode optical fiber was explicitly chosen not to be polarization maintaining. The emitted entangled photons have any polarization and we can thus not allow to have any preferred axis in the fiber. The fiber is enclosed in a metal tube, avoiding unnecessary displacement leading to a change of the differential phase of the guided photons. Both, the fiber output and the whole detection optics are shielded from stray light by a metal housing.

Instead of the intricate separation of cavity stabilization light and signal photons with the help of gratings or prisms, we now use three highly efficient spectral filters to suppress the 785 nm light. This stabilization light is roughly 10 orders of magnitude more intense than the actual signal at 780 nm. The filters of type *LL01-780-25* from *Semrock* are specified to attenuate 785 nm light by at least a factor of 10^4 and have been measured to transmit the 780 nm signal with $\approx 97\%$ each. Two of them are placed before, and one directly after the fiber. In addition to the spectral filters, the optical fiber acts as a spatial filter and efficiently suppresses background stray light.

The optics layout of the detection apparatus is illustrated in figure 6.4. A non-polarizing 50/50 beam splitter (NPBS) equally distributes the photons onto the two detection setups. The NPBS was aligned such that both, horizontal and vertical polarization components are equally distributed with a precision measured better than 1 : 400. At the PBS cubes of the two detection branches, an extinction ratio better than 1 : 1000 for the wrong polarization component at each output port was achieved optimizing the incident beam angle. The polarization of the incident light at the PBS's can be individually defined with the use of a quarter-wave plate ($\lambda/4$) and half-wave plate ($\lambda/2$). Both are mounted on motorized rotation stages of type *DRTM 65* from *Owis*. These rotation stages memorize their position and allow for a quick (with maximum speed of $1200\,^\circ$/s) and precise ($0.1\,^\circ$ absolute positioning resolution) setting of the two polarization bases. Redefining the detection bases in-between consecutive experiment runs reduces possible drifts during long measurements to a minimum.

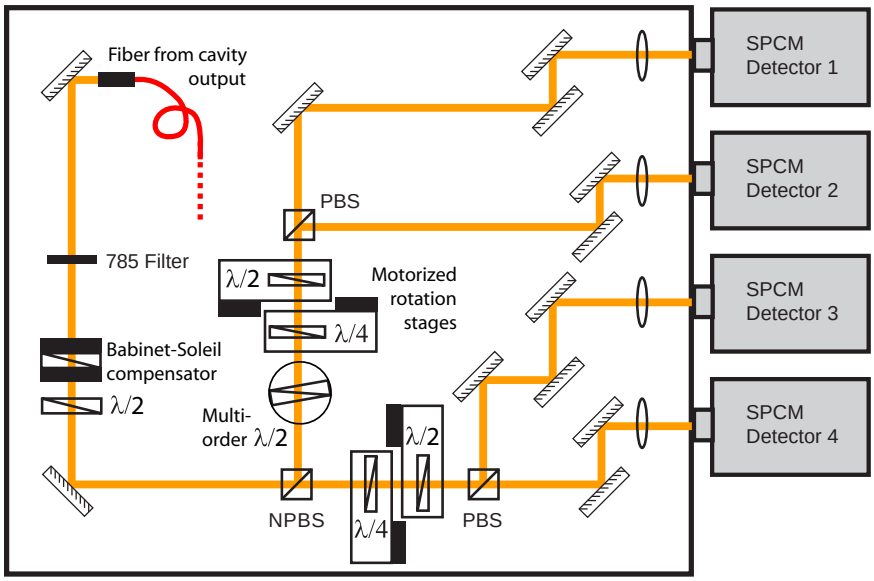

Figure 6.4: The detection apparatus. Coming from the output of a single mode fiber, the single photons from the cavity are directed onto a 50/50 beam splitter (NPBS) which equally distributes them onto the detectors of two independent measurement bases. These measurement bases are defined by half- and quarter-wave plates mounted on motorized rotation stages. This way, the used combination of detection bases can be reset in-between consecutive experiment runs.

Detectors and data acquisition

The four detectors of type *SPCM-AQR16* by *Perkin&Elmer* have a darkcount rate lower than 25 Hz and a measured quantum efficiency of $\approx 50\%$. The overall background detection level for the full detection apparatus was determined to be ≈ 140 Hz, which is only 50 Hz above the measured minimum of 90 Hz given by the detectors alone. The TTL-pulses from the SPCMs are inverted and adapted for the registration with a four-channel TOF multiscaler card with 2 ns time-binning resolution (model *P7888* from *FastComtec*). The four channels are assigned to the four detectors. Additionally, a trigger signal to label the start of each individual pulse sequence also needs to be recorded. This trigger signal is therefore coded as a double-pulse added to the photon signals on channel 4. With a 12 ns separation of the two pulses being significantly shorter than the detector's pulse length of ≈ 50 ns, the two signals are unambiguously separable.

Although the whole detection setup was carefully aligned, the relative detection efficiencies of the four individual channels are still not exactly the same. Measured with V-polarized light and normalized on detector 4, the relative efficiency of the others are 1.08 (detector 1), 1.03 (2), and 1.09 (3). These imperfections have to be considered in the data evaluations, but as long as we equally distribute the measurement bases on the different detectors within full data sets, they will only have minor influence on the results.

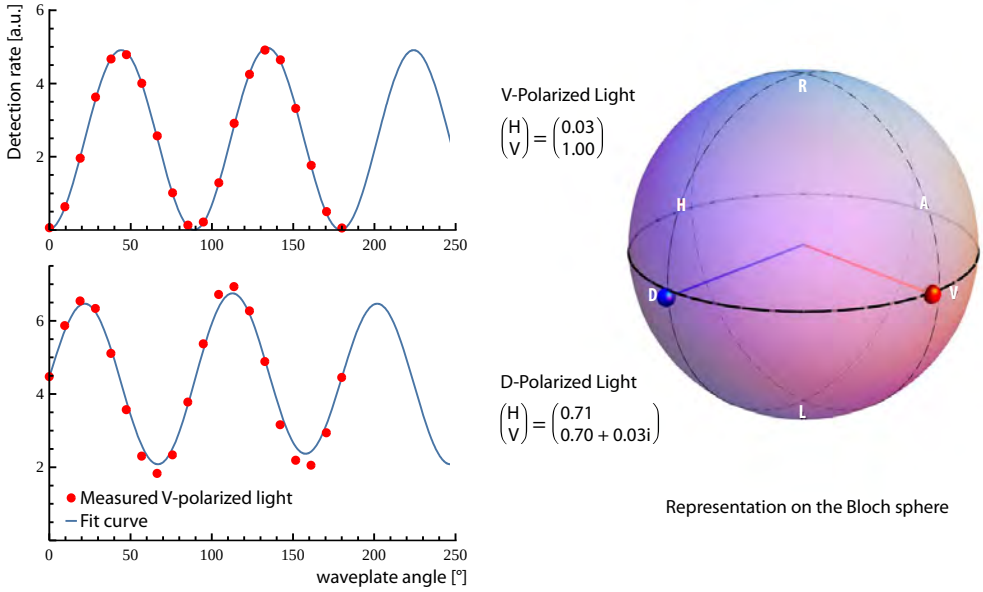

Figure 6.5: Optimization of phase corrections in the detection setup. To test the phase corrections made in the detection setup, we define the polarization state (in our case V or D) via a polarizer before coupling the cavity output to the fiber. Then the signal on a SPCM detecting V- polarized light is recorded while scanning the measurement basis by rotation of a wave plate. Fitting a simulated curve to the data returns the measured polarization state in the H/V basis, which is then compared to the input polarization state.

Phase correction and calibration

To achieve an intuitive mapping of the cavity output polarization onto the measurement bases H/V, D/A and R/L used for data analysis, the individual phase shifts of the optical fiber, the NPBS cube, and the mirrors in the optical path need to be compensated. The overall shift is corrected using a *Babinet-Soleil compensator* followed by a half-wave plate. The relative phase shift between the two output ports of the NPBS cube is equalized with a multi-order half-wave plate, which is set into the beam at an adjustable angle behind the reflected output port of the cube.

To calibrate the phase shift compensation, we developed a quick method based on the test of the detection results for two different polarizers set to transmit H and D light respectively. For each of the polarizers placed at the cavity output, the transmitted light of the locked cavity is detected in a measurement series scanning one of the motorized wave plates. As shown in the example measurement in figure 6.5, the detector set to measure V polarized light shows oscillations when scanning the wave plate angle. To evaluate these signals, the expected signal for this scan is calculated for a given input light state in the H/V basis. Using the input state as a fit parameter, the calculated signal is matched to the measured data. The resulting state vector is displayed on the Poincaré sphere, visualizing how close the results are to the desired states, which are V and D in the given example. With this procedure, we are able to adjust the mapping of the light polarization right

after the cavity to the measurement bases of the detectors. Additionally, when repeated at regular intervals, we are able to trace phase drifts in the optical fiber which guides the photons from the cavity to the detectors.

6.5.3 Magnetic field compensation

During the time between entanglement and mapping process, the two atomic states involved in the entanglement will independently evolve. This means that to successfully measure the entanglement, there should be no differential evolution between these two states, or the exact evolution should be at least known. Magnetic fields lead to such a differential evolution with consequences depending on the field orientation.

In presence of a magnetic field Δ_B parallel to the cavity axis (which is the quantization axis), the two atomic states $|1,-1\rangle$ and $|1,+1\rangle$ are Zeeman-shifted proportional to the magnetic field strength by $+\hbar\Delta_B$ and $-\hbar\Delta_B$ respectively. They will therefore evolve differently in time and accumulate a relative phase given by $e^{i2\hbar\Delta_B t}$. The resulting entangled atom-photon state from equation 6.1 then reads

$$|\Psi_{\mathrm{AP}}\rangle = \frac{1}{\sqrt{2}}(|1,-1\rangle|\sigma^+\rangle - e^{i2\hbar\Delta_B t}\,|1,+1\rangle|\sigma^-\rangle) \tag{6.55}$$

The subsequent state mapping onto a second photon will then fix the value of this phase in the two-photon state

$$|\Psi^-_{\mathrm{PP}}\rangle = \frac{1}{\sqrt{2}}|1,0\rangle \otimes (|\sigma^+\rangle|\sigma^-\rangle - e^{i2\hbar\Delta_B \tau}\,|\sigma^-\rangle|\sigma^+\rangle). \tag{6.56}$$

with τ being the time difference between the two photon emissions. The two-photon entangled state therefore rotates between the two Bell states Ψ^-_{PP} and Ψ^+_{PP}. This was shown experimentally by Tatjana Wilk [71].

The case of a magnetic field orthogonal to the cavity axis is more complicated. As quantization axis and magnetic field now point at different directions, the atomic states as defined via the cavity axis are precessing around the magnetic field axis. This leads to an interchange of the populations of all three F=1 Zeeman states. So to maintain the Ψ^-_{PP} state during the time interval between entanglement creation and mapping pulse, we have to carefully eliminate residual magnetic fields in the experiment.

To identify the zero-point of the magnetic field in the atom trapping region, we ran the full entanglement sequence similar to the one shown in figure 6.11. The two subsequently emitted and detected photons from the entanglement and mapping processes are expected to show orthogonal polarization in any detection basis, if the magnetic field is zeroed. To quantify this, a signal we refer to as the *Contrast* is defined as

$$C = \frac{N_{\uparrow\downarrow} + N_{\downarrow\uparrow} - N_{\downarrow\downarrow} - N_{\uparrow\uparrow}}{N_{total}} \tag{6.57}$$

with $\uparrow$ and $\downarrow$ labeling the two polarizations of a given detection basis, and N being the number of detected two-photon events. It essentially represents the fraction of photon

pairs measured to have orthogonal polarization and takes the value of 1 for perfectly correlated photons representing the entangled state from equation 6.2. We performed two different types of measurements, one scanning the magnetic field and the other scanning the temporal separation of the two pulses.

Magnetic field scans

The magnetic field in our setup can be adjusted with the help of three orthogonal pairs of coils oriented along the dipole trap axis, the cavity axis and the vertical axis. The first of the two methods to minimize the magnetic field consists in simply scanning each of these axes individually looking at the correlation contrast in two different bases. As magnetic field scans are rather time-consuming when using only single trapped atoms, we decided to load multiple atoms into the cavity giving more correlations per experiment run. We found that we still obtain the expected signals, but with a reduced contrast of about 0.3 compared to values of up to 0.8 achieved with single atoms [71]. This can be explained with rather low photon emission probabilities of about 10% for each laser pulse. If the atom numbers are not too large, the correlation signals from the individual atoms are not fully hidden by random correlations between photons from different atoms.

As can be seen from equations 6.55 and 6.56, scanning the magnetic field **parallel to the cavity axis** is equivalent to scanning the phase between the two atomic states involved in the entanglement. For any measurement of the first photon in a basis projecting the atomic state into a superposition of $|1,-1\rangle$ and $|1,+1\rangle$, we are sensitive to this relative phase. A magnetic field scan therefore leads to an oscillation of the contrast in the H/V and A/D bases as shown in the example data presented in figure 6.6. In the R/L basis, the contrast should in this case show a constant value as long as the total magnetic field is dominated by the cavity-axis component. However, as seen in the figure, the contrast decreases to a value of ≈ -0.35 at an applied field of ≈ -0.2 Gauss, indicating the Zero-point of the cavity-axis magnetic field. This Signature was obtained with intention by the application of a constant offset field along the dipole trap axis. Depending on their relative amplitudes, either the scanned field component parallel to the cavity is dominant (at large values of $B_{\parallel}$), or the constant component $B_{\perp}$ determines the observed contrast signal. For a good choice of the offset field value, this results in a signal dip as shown in the data.

For a magnetic field scan **orthogonal to the cavity axis**, we also find oscillations in the contrast, this time caused by the state populations being interchanged. The oscillation frequency is only half of that observed in the case of a field along the quantization axis, i.e. it only rotates with $e^{i\hbar\Delta_B t}$ compared to $e^{i2\hbar\Delta_B t}$. While this phenomenon is observed in the magnetic field scans, the exact mechanism is not completely understood. Similar to the case of the parallel field, we can induce a dip in the contrast seen in the other measurement bases. These markers made the clear identification of the zero-points of the three magnetic field components possible.

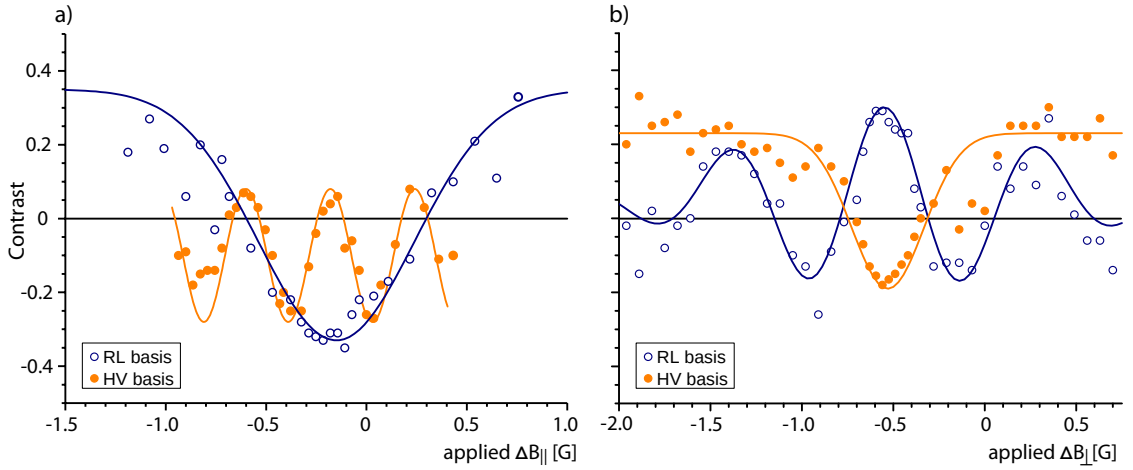

Figure 6.6: Determining the zero-point of the magnetic field. The contrast C for the photon correlations is measured varying the applied compensation field along one axis. a) A scan of the field parallel to the cavity axis shows oscillations (filled circles) in the contrast in the R/L basis, representing the differential state evolution. In presence of an appropriately chosen orthogonal offset field, the otherwise constant contrast in H/V has a dip pointing at zero magnetic field on the cavity axis. b) For a scan of the magnetic field orthogonal to the cavity axis, the roles of R/L and H/V are interchanged and the oscillation period is only half as long. These signals have their origin in the rotation and mixing of the atomic states due to the Larmor precession around the magnetic field axis. The solid curves are approximations to the data to guide the eye.

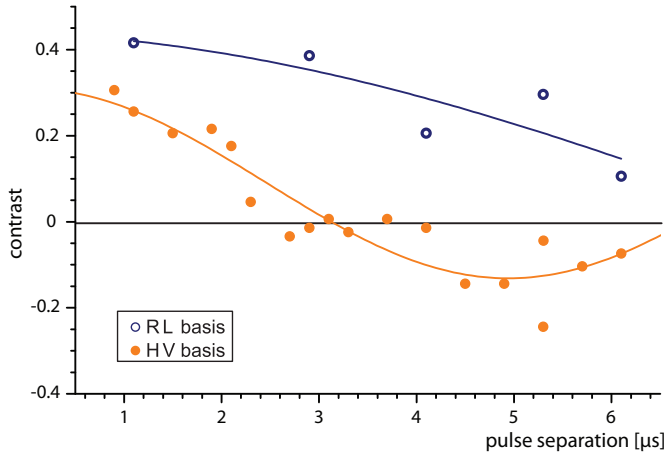

Figure 6.7: Contrast measurements at different pulse separation times show the oscillations observed with the magnetic field scans in the time domain. As the signal obtained in the R/L basis is insensitive to magnetic fields parallel to the cavity axis, one can independently determine the remaining magnetic field components parallel and orthogonal to the cavity using the detection bases H/V and R/L.

Pulse separation scans

Another way to find the magnetic field minimum is to vary the temporal pulse separation Δt and measure the resulting contrasts in different bases. With a scan of Δt, we expect from equation 6.56 to see oscillations in the contrast proportional to the magnetic field. As discussed before, the oscillation in the R/L detection basis is independent of the cavity-axis field. We can therefore calculate the remaining magnetic field parallel and orthogonal to the cavity from the observed oscillation frequencies. A very useful method to fine-tune the field compensation was to take a full curve as displayed in figure 6.7, adjust the pulse separation to the time of the zero-crossing of the oscillation and then incrementally try to increase this contrast varying the magnetic field. In principle, this method can be extended to very long timescales.

Although we carefully minimized the static magnetic field with the described methods, we still observed offset fields of a few 10 mG in some state tomography results, pointing at changing conditions in the laboratory from day to day. Additionally, we are only sensitive to DC magnetic fields. Significant AC field components would make an active magnetic field control necessary, a technical upgrade that would certainly help improving the entanglement results.

6.5.4 Stark shift compensation

For a good performance of the entanglement protocol, all applied laser pulses should be resonant with the actual atomic transitions. This not only increases the efficiency of the individual processes, but at the same time suppresses unwanted coupling to other atomic states. For our standing-wave trap configuration, the theoretical maximum Stark shift for the $D2$-line is calculated to be 103 MHz. Considering the atoms being cold, but not in the motional ground state, the actual Stark shift of the atomic resonance is fluctuating on a timescale defined by the trap frequencies. This means, the linewidth of the transition will appear broadened. In the experiments done so far with this apparatus, several attempts have been made to measure the Stark shift in the system, leading to values of ≈ 70 MHz [61; 63].

For the entanglement experiments, we developed a new scheme to deduce the Stark shift of the atomic resonance measuring the population transfer efficiency of a single laser pulse. This transfer pulse is embedded into a sequence with additional atom preparation and state detection pulses. As shown in figure 6.8, we drive a *vacuum-stimulated Raman adiabatic passage* (vSTIRAP) with the cavity on the $F{=}1 \leftrightarrow F'{=}1$ transition and a laser pulse tuned to $F{=}2 \leftrightarrow F'{=}1$, to pump all atoms into the $F{=}1$ state. After this preparation, the population is transferred to the $F{=}2$ state with a laser pulse addressing the transition $F{=}1 \leftrightarrow F'{=}2$ with a certain detuning to its natural frequency. As the cavity is not resonant, no photons are detected during this process. The efficiency of the transfer is subsequently probed with another vSTIRAP, this time applying a pulse on $F{=}1 \leftrightarrow F'{=}1$. The photon scattering rate into the cavity is proportional to the population remaining in the $F{=}1$ after the transfer pulse. Scanning the detuning of the $F{=}1 \leftrightarrow F'{=}2$ pulse, we

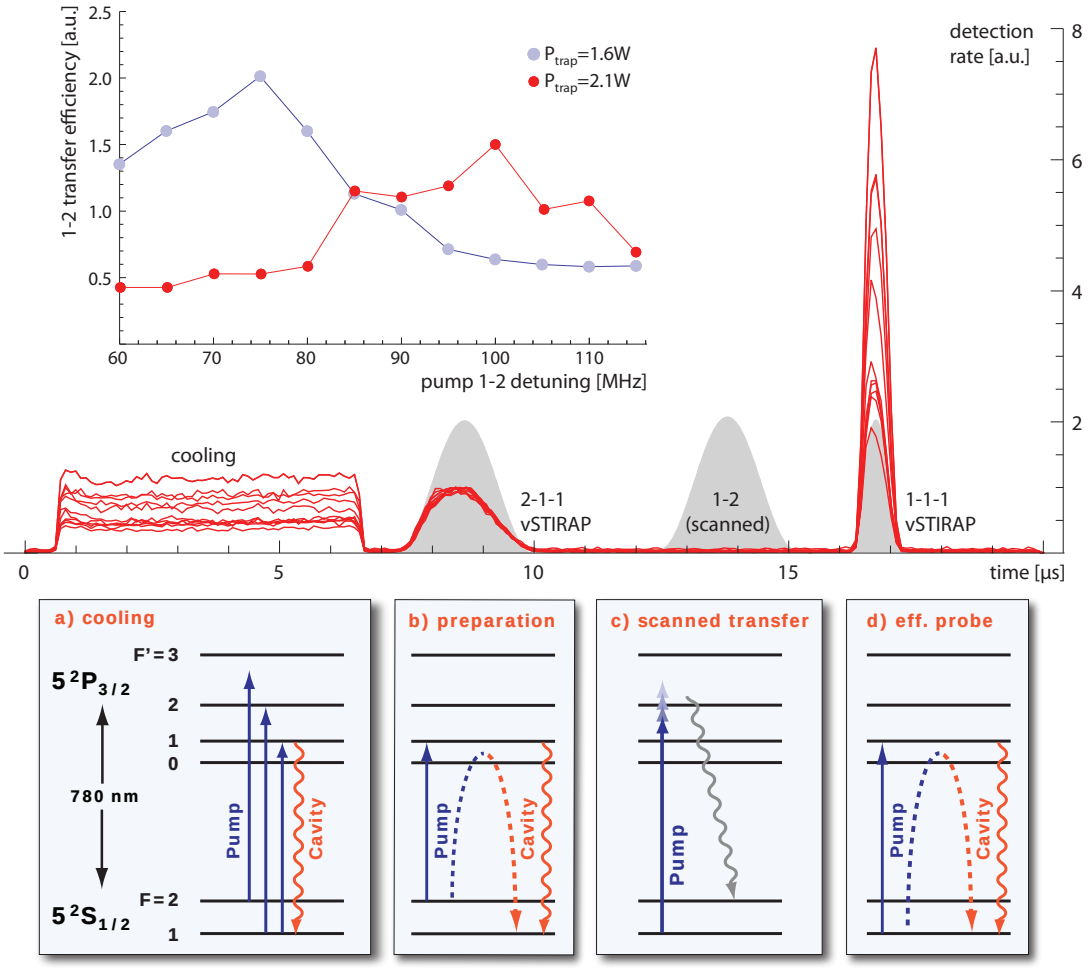

Figure 6.8: Stark shift measurements. To find the shifted resonance, the detuning of a probe laser on $F{=}1 \leftrightarrow F'{=}2$ transferring the atoms to the $F{=}2$-state is scanned. The population remaining in the $F{=}1$ state is proportional to the photons scattered into the cavity during a $F{=}1 \leftrightarrow F'{=}1$ detection pulse.

can find the Stark-shifted resonance by evaluating its transfer efficiency. To collect some statistics, we average over a series of ~ 20 experimental runs with multiple atoms for each detuning value. The detected photon rate is normalized on the signal obtained during the first STIRAP.

The results in figure 6.8 show a rather broad resonance at $\approx 95\,\mathrm{MHz}$ for our standard standing-wave trap using a 1030 nm-laser power of 2.1 W. To test the reliability of the method, we also performed a scan with the laser power reduced to $1.6\,\mathrm{W} \approx 0.8 \times 2.1\,\mathrm{W}$. This results in a shift of the measured resonance to $\approx 75\,\mathrm{MHz} \approx 0.8 \times 95\,\mathrm{MHz}$. Although the resonances are quite broad due to the atom dynamics in the trap, this proves the scheme to be a safe method to approximately determine the Stark shift. This is mainly attributed to the fact that the vSTIRAP signals used for normalization and to probe the transfer efficiency are quite robust against Stark-shift-induced detunings from the exited

state. Comparing the obtained Stark-shift value of 95 MHz to the theoretical calculation of 103 MHz for perfectly overlapping beams also indicates a quite good alignment of the standing wave trap. The measured value is of course the sum of the individual components induced by the main dipole trap and the trap provided by the 785 nm stabilization laser. But with an estimated contribution of $2-3$ MHz, the intra-cavity trap only plays a minor role here.

Differential Stark shifts

Until now, we only considered Stark shifts averaged over the hyperfine- and Zeeman states, as their energy splitting is small compared to the detuning of the trap light, at least for the deep standing-wave trap at 1030 nm. For the entanglement protocol, the relative time evolution of the two Zeeman states $|1,-1\rangle$ and $|1,+1\rangle$ is very crucial for the coherence of the entangled state. Therefore we need to analyze the differential Stark shifts between these two states. While there are no state-dependent shifts for linear trap light, circular light induces differential shifts between the three Zeeman substates of the F=1 hyperfine-level. These state-dependent Stark shifts are plotted versus the trap light wavelength in figure 6.9. The left side illustrates the situation in the vicinity of the intra-cavity trap. We can see from the plot, that at a wavelength of 785 nm, the energy shift of the $|1,-1\rangle$ state is only about one third of that of $|1,+1\rangle$. So far, the trap light was coupled into the cavity with circular polarization with the differential shift taking full effect. This means, that the 3 MHz total Stark shift mentioned above results in an estimated differential Stark shift of ≈ 2 MHz. To avoid this situation, we changed the trap polarization from circular to linear installing a polarizer (due to spatial restrictions) at the cavity input and compensating the intensity loss.

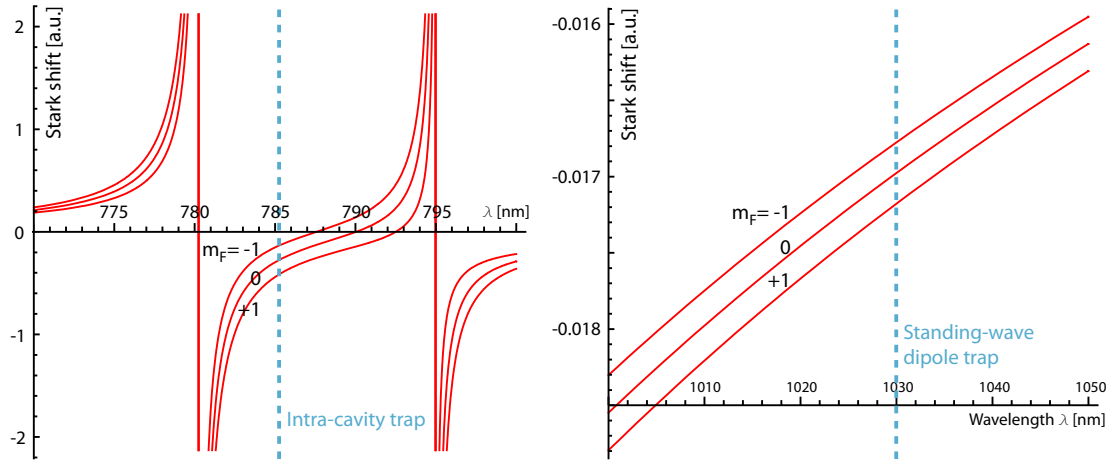

Figure 6.9: Theoretical differential Stark shifts for circular polarized light. With circular polarization components in the trapping light, the Zeeman states $|1,-1\rangle$ and $|1,+1\rangle$ experience different Stark shifts. The time evolution of the two states would therefore be different. The relative differential shift is about two thirds of the full trap depth for the 785 nm trap and $\approx 2.5\%$ for the deep trap at 1030 nm.

For the trap at 1030 nm, the relative differential shift is smaller, but scaled to the ≈ 95 MHz total Stark shift the $\approx 2.5\%$ difference extracted from the right plot of figure 6.9 still makes ≈ 2.4 MHz for circular light. The standing-wave trap is composed of two linearly polarized beams, but birefringence of the viewports may add circular components leading to decoherence of the entangled state, as discussed later in section 6.6.7.

6.5.5 Optical pumping and laser polarization optimization

As shown in section 6.1, the entanglement protocol will only succeed when the atom has been prepared in the $|\mathrm{F}, \mathrm{m_F}\rangle = |2, 0\rangle$ state. It is therefore necessary to implement an efficient optical pumping procedure, as the overall performance of the full scheme depends on the probability of starting in the right state. We apply a π-polarized laser resonant with $F{=}2 \leftrightarrow F'{=}2$ to empty all Zeeman states with $F{=}2$ and $m_F \neq 0$ and accumulate the population in $|2, 0\rangle$, as this is a dark state according to the transition selection rules. This pumping process is of course not directional. The state population is redistributed performing a random walk between the Zeeman substates until it accumulates in $m_F = 0$. As the atom can also decay to the $F{=}1$ ground state, we additionally need a repumping process which is provided by the application of a $F{=}1 \leftrightarrow F'{=}2$ laser. These two lasers addressing the same excited states induce an additional coherent dark state, so we also have to apply a second repump laser at $F{=}1 \leftrightarrow F'{=}1$.

To optimize the optical pumping process, we ran a sequence as illustrated in figure 6.10 at a repetition rate of 20 kHz. Following a $\approx 30\,\mu$s long cooling phase, the optical pumping procedure is applied for about $8\,\mu$s. A characteristic signal for a successful optical pumping process would be the reduction of the photon emission rate on the $F{=}2 \leftrightarrow F'{=}2$ transition while the atoms get trapped in the dark state. The cavity was therefore locked to this frequency and we observed signals as shown in figure 6.10. The most interesting feature is the signal decay during the optical pumping phase. Attributing the initial peak level to the scattering rate resulting from an equally distributed state population, the observed signal reduces while the atoms are pumped to the $|2, 0\rangle$ state. The repump process was tested to be much faster than the observed decay, so loss to the $F = 1$ state will only show a minor contribution to the signal. While in an ideal process the signal should approach zero, our final scattering rate is limited to a certain fraction of the start level. This is reasonable, if we consider the imperfections in our system leading to a loss from $|2, 0\rangle$. It is not only that the applied lasers, especially the one on $F{=}2 \leftrightarrow F'{=}2$, will occasionally drive unintended off-resonant transitions to other states. The more critical parameter is the polarization of the pump laser. It can be clearly defined to be π-polarized outside the vacuum chamber, but has to be optimized for the atoms inside the chamber as the viewports may be birefringent and thus rotate the polarization. Even small deviations from the ideal π-polarized light open excitation channels from $|2, 0\rangle$. Thinking of these factors as loss rates compared to the pump rates in a rate equation, it is clear that the final scattering rate, and also the efficiency of the optical pumping process, is limited.

To estimate the population fraction in $|2, 0\rangle$, we take the ratio of initial peak value and final remaining signal as a measure for the efficiency of the whole process. The polarization of

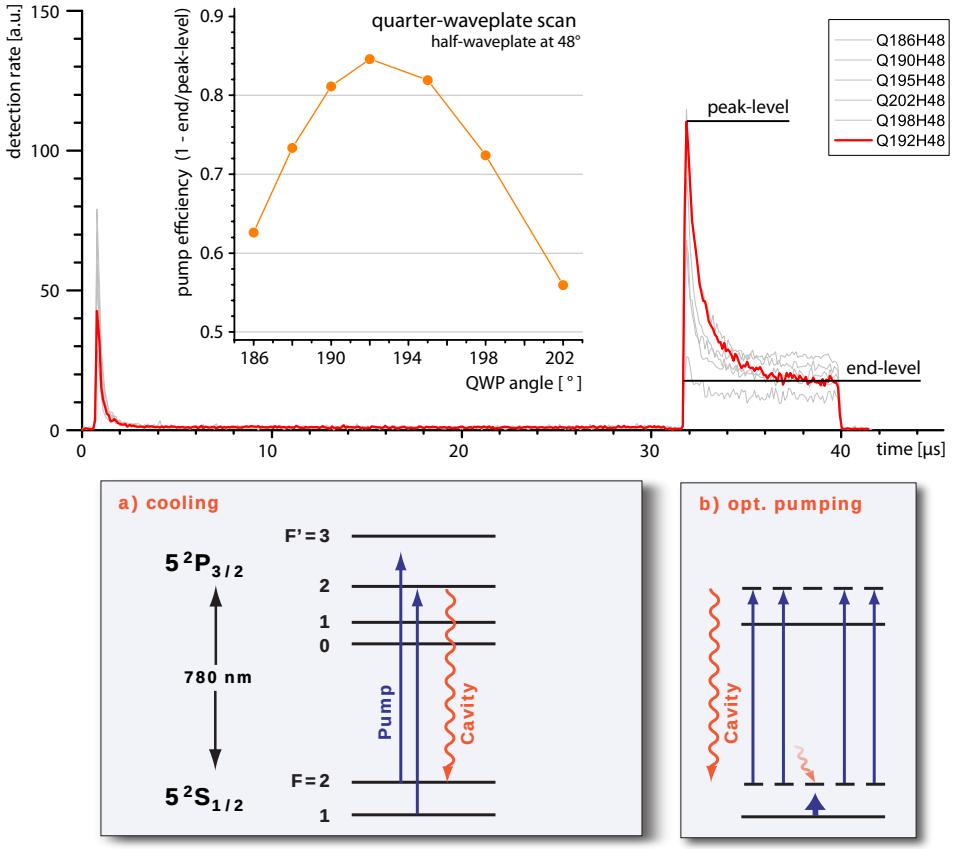

Figure 6.10: Optical pumping. With the cavity locked to the $F{=}2 \leftrightarrow F'{=}2$ transition, the optical pumping process can be studied. We take the ratio of initial peak level and remaining signal at the end as a measure for the efficiency of the process. The polarization of the pump laser was optimized using this signal.

the pump lasers was optimized on this signal, as shown in an example measurement result in figure 6.10. The polarization can be adjusted using a half-wave and a quarter-wave plate. We performed measurements scanning the quarter-wave plate angle for a series of half-wave plate orientations. Although the method turned out to be quite reliable, the ideal wave plate orientations could only be determined within an error of $\pm 1\,^\circ$ each. Compared to their original settings for vertical linear light, the half-wave plate had to be rotated by $+1\,^\circ$, and the quarter-wave plate by $+3\,^\circ$ for an optimal compensation of the birefringence. For the laser intensities applied later in the actual entanglement sequences (see the following section) we estimate the efficiency of the optical pumping to be $\approx 80\%$.

6.6 Entanglement results

Implementing the scheme described before in section 6.1, we created entanglement between single trapped atoms in the cavity and single emitted photons. As the atomic part of the produced state is subsequently mapped onto a second emitted photon, we can verify the entanglement by measuring the polarization state of the two photons. With such measurements, we were able to demonstrate that the entangled photons clearly violate a Bell inequality. Additionally, we performed a full quantum-state tomography on the two photons and reconstructed the density matrix of the state. To further characterize the system, the coherence lifetime was determined in a series of tomography measurements with increasing temporal spacing between entanglement generation and mapping process.

6.6.1 Experiment sequence

After finishing the described optimization measurements, the parameters for the experimental sequence for all the measurements described in this chapter were fixed. A single experimental run starts with the standard atom loading process. Cold atoms from the MOT are transferred to the cavity and trapped within the antinodes of two orthogonal standing-wave traps provided by the 1030 nm YAG-laser and the 785 nm cavity stabilization laser. A subsequent filter phase of 10 ms without the 1030 nm trap selects only atoms that are well-coupled to the cavity. The number of trapped atoms can be adjusted to be one on average by adapting the duration of the MOT loading period. For the whole experiment, the cavity frequency is locked to the $F{=}1 \leftrightarrow F'{=}1$ transition, shifted by $\Delta = +90\,\mathrm{MHz}$ to compensate the Stark effect of the traps.

With this initial preparation, we start our experiment with a 300 ms long interval where the atom is mainly cooled using the Sisyphus-like cooling mechanism. As illustrated in figure 6.11 a), the lasers applied on the atom in this interval are:

Transition	Polarization	Detuning Δ	Intensity
$F{=}2 \leftrightarrow F'{=}3$	lin $\perp$ lin	0 MHz	$3\,\mu$W
$F{=}1 \leftrightarrow F'{=}2$	lin $\perp$ lin	90 MHz	$0.2\,\mu$W
$F{=}1 \leftrightarrow F'{=}1$	π-pol.	87 MHz	$0.1\,\mu$W

While the $F{=}2 \leftrightarrow F'{=}3$ laser with its large detuning from the Stark-shifted atomic resonance does the cooling, the $F{=}1 \leftrightarrow F'{=}2$ light is only applied for repumping. The $F{=}1 \leftrightarrow F'{=}1$ laser is near-resonant with the cavity and is intended to scatter photons into the resonator for atom detection purposes. As its light pressure is not balanced, we can only use low intensities, limiting the scattering rate into the cavity to a few 100 Hz. With this, it is not possible to reliably filter single atoms events by just using the cavity signal. At the same time, as an effect of the cooling on the $F{=}2 \leftrightarrow F'{=}3$ transition, a lot of photons are scattered into free space. We therefore adapted the length of this cooling period such that we collect enough light with the CCD-camera system to obtain a clear

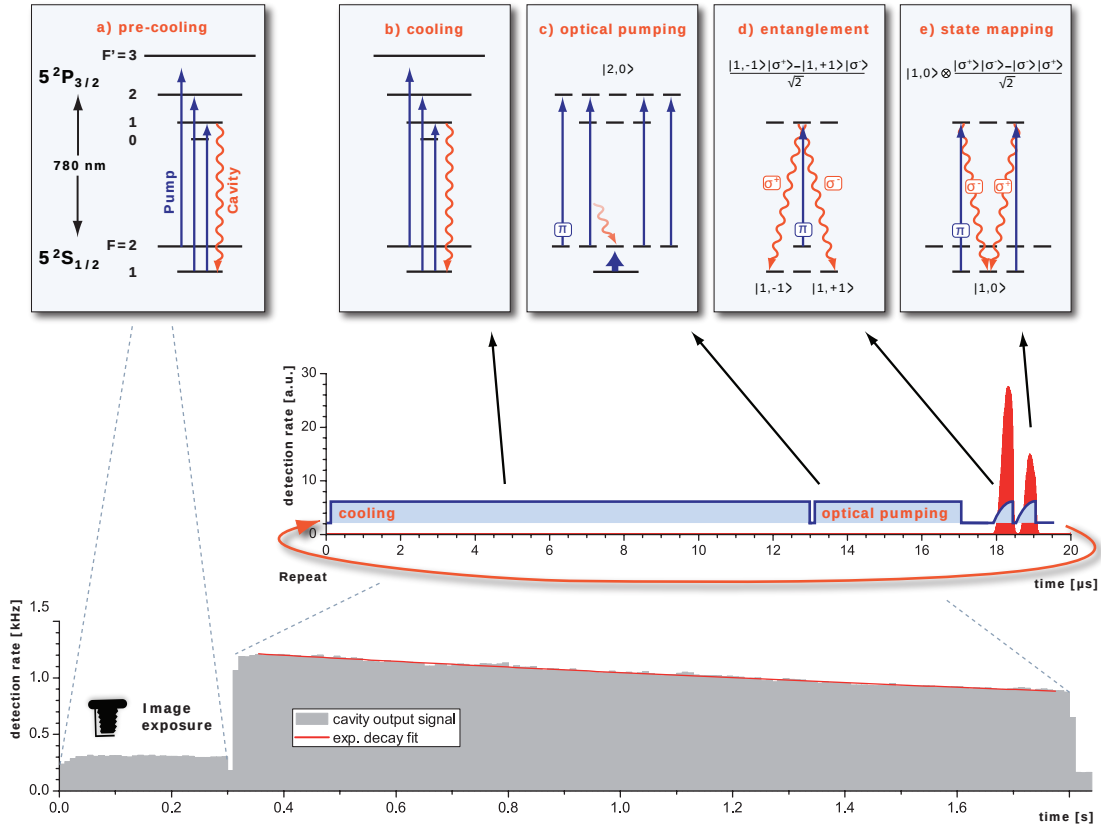

Figure 6.11: The experiment sequence used for the main results presented in this chapter divides into two parts. First, during a $300ms$ long interval only cooling lasers are continuously applied, mainly to collect enough light on the camera to obtain a picture of the atom with a good signal-to-noise ratio. In the second phase, the entanglement scheme is repeatedly applied as a series of laser operations on the atom: atom cooling, optical pumping to the $|2,0\rangle$ state, entangling pulse on $F{=}2 \leftrightarrow F'{=}1$, and mapping pulse on $F{=}1 \leftrightarrow F'{=}1$. The fact that all π-polarized lasers are impinging from one side only limits the lifetime of the atoms to $3.8s$ while the entanglement scheme is applied.

image of the trapped atom(s). These images are used to select single atom trapping events from the whole data set, as described later in this section.

The initial cooling interval is followed by the repeated application of our entanglement protocol. This can be divided into a series of four different phases:

- **Cooling (fig. 6.11b).** During this $\approx 13\,\mu$s long interval, we again make use of the Sisyphus-like cooling effect. It is supposed to compensate heating of the atom caused by the unidirectional light pressure acting on the atoms during the following phases. The laser configuration is again that of the table given above.

- **Optical pumping (fig. 6.11c).** The atom is prepared for the entanglement process by optically pumping it into the $|2,0\rangle$ state. To do so, we make use of the fact that

a π-polarized laser on the $F{=}2 \leftrightarrow F'{=}2$ can drive transitions from all Zeeman states but the $|2,0\rangle$ state, and thus we accumulate population there. For the full scheme, we apply the following lasers for a period of $\approx 4\,\mu$s:

Transition	Polarization	Detuning Δ	Intensity
$F{=}2 \leftrightarrow F'{=}2$	π-pol.	90 MHz	$0.1\,\mu$W
$F{=}1 \leftrightarrow F'{=}2$	lin $\perp$ lin	90 MHz	$0.2\,\mu$W
$F{=}1 \leftrightarrow F'{=}1$	π-pol.	90 MHz	$\approx 0.1\,\mu$W

Additional details on the optical pumping process can be found in the previous section 6.5.5.

- **Atom-photon entanglement (fig. 6.11d).** The entanglement process is carried out driving a vSTIRAP transition from the $|2,0\rangle$ to the $F{=}1$ ground-state. We apply a $0.4\,\mu$s long, π-polarized laser pulse resonant with the Stark-shifted transition $|2,0\rangle \leftrightarrow |1',0'\rangle$. We can drive this pulse with a relatively high intensity of $3\,\mu$W, as with the atom being then in $F{=}1$, the laser is so far detuned that additional excitations are very unlikely. Defining the quantization axis, the cavity supports only σ-polarized modes and so we have two final states for the vSTIRAP process, namely the two ground states $|1,-1\rangle$ and $|1,+1\rangle$. This way, the polarization of the photon emitted into the cavity gets entangled with the atomic state and we prepare

$$|\Psi_{\mathrm{AP}}\rangle = \frac{1}{\sqrt{2}}(|1,-1\rangle|\sigma^+\rangle - |1,+1\rangle|\sigma^-\rangle). \tag{6.58}$$

- **State mapping. (fig. 6.11e).** To map the atomic part of the entangled state onto the polarization of a second photon, we apply another vSTIRAP pulse, this time with a π-polarized laser resonant with the $F{=}1 \leftrightarrow F'{=}1$ Stark-shifted transition and a power of $1\,\mu$W. The polarization of the photon emitted during this mapping process corresponds to the two atomic states involved in the entanglement. So the two subsequently emitted photons are entangled in the state

$$|\Psi^-_{\mathrm{PP}}\rangle = \frac{1}{\sqrt{2}}|1,0\rangle \otimes (|\sigma^+\rangle|\sigma^-\rangle - |\sigma^-\rangle|\sigma^+\rangle). \tag{6.59}$$

  The polarization of the two photons emitted from the cavity is always orthogonal, but their assignment is not defined until the first photon's polarization is detected.

This sequence of four separate phases is normally run for 1.5 s, with a repetition rate of 50 kHz. Within the $20\,\mu$s period, the temporal separation of entangling and mapping pulse can be adjusted and is here set to 0.8μs. This means the verification of the entanglement always takes place after a certain time interval in which the state evolves according to external influences on the atom like magnetic fields of differential Stark shifts. Thus, we do not measure the properties of the original atom-photon entanglement, but the remaining entanglement after a certain time evolution of the state 6.58.

6.6.2 Data analysis

The two subsequently emitted photons are coupled to a single-mode optical fiber at the cavity output and then directed to the detection setup described in section 6.5.2. The motorized wave-plates allow a redefinition of the measurement bases during the MOT-loading phase of every single experiment run, which avoids systematic drifts during the measurements. While the parameter settings of the measurements are recorded in a SQL-database, the photon detection events registered with the $P7888$-card are saved in a raw binary format. The images taken with the Ixon-camera are saved both in a self-defined raw data format and in a standard ".png"-format. The images are linked to the photon data via unique filenames. This way, the data analysis software developed for this project, QDataExplorer, has full access to all parameters and data.

For the entanglement scheme, it is again very important that only data taken from single trapped atoms enter the evaluations. To ensure this, we filter the recorded data files applying two independent tests:

- **Image analysis.** The image of the trapped atom(s) taken during the first 300 ms long cooling interval is analyzed as described in chapter 5.2. With a signal-to-noise ratio of about 8 : 1, we estimate the probability to successfully detect a single atom to be $\approx 90\%$. On a second image taken during the pulse sequence with heating processes included, the atom position seems to be not static enough, with the consequence that a mode hop of a single trapped atom during the exposure time mimics two individual atoms on the recorded image. As we did not want to discard good data because of image misinterpretations, we stayed with the first image taken in advance.
- **Photon correlation analysis.** Very similar to the experiments with the single photons described in chapter 4, multiple trapped atoms leave a telltale trace in the two-photon correlations of a single-photon process. Applied to our pulse scheme, the $F{=}2 \leftrightarrow F'{=}1$ entangling pulse is the ideal candidate for a correlation analysis, as multiple photon emissions in this process can be attributed to multiple atoms with almost 100% certainty. The selection is carried out by calculating the correlation function for the photons detected during the entangling pulse with a binning of $20\,\mu$s, corresponding to the sequence length. We accept a data file as a single atom trapping event, if it shows a $\Delta\tau = 0$ coincidence rate of at most 0.5 of the average correlation signal for $\Delta\tau \neq 0$, and, additionally $N_{\mathrm{corr}}(\Delta\tau = 0) \leq 1$. The selection criteria are based on the experimental observation that trapping events with two or more atoms typically show $N_{\mathrm{corr}}(0) \geq 1$ while there is a 10% chance for a single coincidence just from background signal.

The selection of data for the entanglement measurements using these two selection criteria is legitimate as we consider only properties of the data that are independent of the derived results. Typical examples for results of these tests are shown in figure 6.12. Applied for example on the data for the Bell measurement described in the next section, the image analysis selected 1433 out of 7858 data files, which means that in 18% of all trapping attempts we had a single atom stored for at least as long as it needs to be detected on

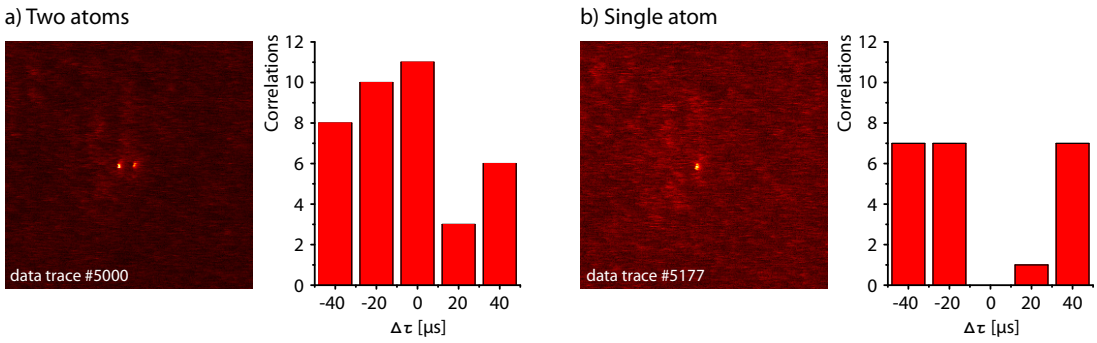

Figure 6.12: Data selection using camera images and a photon correlation test. A data file is only kept for further evaluation if exactly one atom is detected on the image and the photons emitted during the entanglement process show antibunching in the cross-correlation. The plot shows typical test results for a trapping event with two atoms (a) and one with just a single atom (b).

the image shot in the first 300 ms. Out of this selection, 90% or 1292 data files pass the correlation test and are used for the evaluation.

After the application of the two filters, we can extract the efficiencies of the individual processes in the entanglement scheme. From a series of measurements we select those intervals clearly showing that a trapped atom was present in the cavity. This results in a total number of 75.9 million run sequences in 1518 seconds of trapping time. Within these, 1.250×10^6 first photons, 0.606×10^6 second photons, and 25641 two-photon correlations were detected. Including an approximated total detection efficiency of ≈ 0.18, we find the probability of producing a first photon to be 9%. Conditioned on the existence of this first photon, the probability to create the second photon in the cavity is 11%. This gives a total probability of 1% for a photon pair to be produced and 0.03% for being detected. On average, we find 17 detected pair correlations per second with a single-atom trapped in the cavity.

Compared to the clean process of the entanglement pulse on $F{=}2 \leftrightarrow F'{=}1$, allowing for only one emitted photon, the mapping procedure has additional channels leading to the occasional emission of a second photon. This second-photon rate mainly scales with the pulse length and intensity. The probability of detecting additional photons increases towards the end of the mapping pulse. For this reason, we cut the tail of this pulse at position 19.0 μs, as it improves the results significantly while removing only a small fraction of the data. This selection of course reduces the detection probability of a two-photon correlation to 0.024%. A more detailed analysis of this issue is given in section 6.6.7.

6.6.3 Bell inequality violation

Following the ideas discussed in 6.2, we measured correlation coefficients $E(\alpha, \beta)$ to obtain a Bell-signal $S(\alpha, \alpha', \beta, \beta')$ as proposed by C.H.S.H. [85]. The largest effect is expected for the choice of angles $\alpha = 0\,^\circ$, $\alpha' = 45\,^\circ$, $\beta = -22.5\,^\circ$ and $\beta' = 22.5\,^\circ$. To measure these correlations in our detection setup, one of the measurement basis has to be set to detect H/V or D/A while the other basis detects in the $-22.5\,^\circ/67.5\,^\circ$ or $22.5\,^\circ/112.5\,^\circ$ basis. In the standard definition of the Bell measurement, the first photon would be detected in one of the α-bases and one would measure the probability to detect the other photon in one of the β-bases. As the 50/50 beam splitter randomly distributes the photons between the two detection bases, only one quarter of the detected two-photon events can be used for such a measurement, namely those with the first photon in basis one and the second in basis two. While all events with both photons detected in the same basis can only be used for normalization purposes, those where just the roles of first and second photon are interchanged correspond to a Bell measurement with exchanged α and β values. The Bell measurement performed here was measured in the 4 necessary basis combinations and in the corresponding 4 combinations with interchanged detection bases to avoid systematic errors. In the data set of 1292 single atom trapping events, we find 3947 relevant correlations for the standard Bell-measurement leading to the following result:

Bell inequality 1		
$E(0\,^\circ, 22.5\,^\circ)$	$=$	-0.49 ± 0.03
$E(0\,^\circ, -22.5\,^\circ)$	$=$	-0.70 ± 0.02
$E(45\,^\circ, 22.5\,^\circ)$	$=$	-0.74 ± 0.02
$E(45\,^\circ, -22.5\,^\circ)$	$=$	$+0.54 \pm 0.03$
$S(0\,^\circ, 45\,^\circ, 22.5\,^\circ, -22.5\,^\circ)$	$=$	2.46 ± 0.05

The same data set also contains 4142 correlations matching the Bell measurement with interchanged angle values and giving a second Bell signal result:

Bell inequality 2		
$E(22.5\,^\circ, 0\,^\circ)$	$=$	-0.73 ± 0.02
$E(-22.5\,^\circ, 0\,^\circ)$	$=$	-0.56 ± 0.03
$E(22.5\,^\circ, 45\,^\circ)$	$=$	-0.55 ± 0.03
$E(-22.5\,^\circ, 45\,^\circ)$	$=$	$+0.68 \pm 0.02$
$S(22.5\,^\circ, -22.5\,^\circ, 0\,^\circ, 45\,^\circ)$	$=$	2.53 ± 0.05

Quantum mechanics predicts an absolute value of $1/\sqrt{2}$ for each of the $E(\alpha, \beta)$ values and thus a total signal of $S = 2\sqrt{2}$. This maximum value can only be achieved with a maximally entangled state and ideal detection. On the other hand, the classical limit

of the Bell inequality is $S = 2$. Our results show a violation of the inequality by more than 9 standard deviations. This clearly proves that the two detected photons formed an entangled state.

It is remarkable, that the photons violate a Bell inequality although they never existed at the same time. Without the prior detection of the first photon, we would certainly produce an entangled two-photon state with properties similar to our data. The fact that we measured this Bell inequality violation despite the photon detection leads to the conclusion, that there had to be prior atom-photon entanglement and a subsequent transfer of quantum information from the atom to the second photon.

6.6.4 Tomography of the two-photon state

The Bell measurement convincingly verified the produced entanglement. To get a more detailed picture of the entangled state, we performed a tomography on the two photons following the recipe described above. We choose our detection bases to be H/V, D/A and R/L. It would be sufficient to measure the photons in the three possible combinations of different measurement bases. Nevertheless, to avoid systematic errors due to imbalanced detection probabilities and wave plate mismatches, we also measure with the chosen bases being interchanged between the two detection setups. Another technical source of error arises from the detectors themselves. It turned out that one and the same detector can produce a two-photon coincidence signal although there was only one photon present. False pulses in the detection electronics, as for instance afterpulsing of the SPCMs, should be the origin of this effect. As this effect was to large to be neglected, the consequence was to only counte those coincidence events where the two photons were detected in different detection setups. To include correlations within the same measurement basis, we had to add three settings with both detection setups being identical. Altogether, we measured the photons in the following nine detection configurations:

detectors	basis combination								
	1	2	3	4	5	6	7	8	9
setup one: 1/2	H/V	H/V	H/V	D/A	D/A	D/A	L/R	L/R	L/R
setup two: 4/3	H/V	A/D	L/R	H/V	D/A	L/R	H/V	D/A	L/R

With this, the measured two-photon events are equally distributed over all four detectors. To obtain a density matrix of the state at a pulse separation of $0.8\,\mu$s, we took a data-set containing 826 single-atom trapping events. Analog to the case of the Bell-measurement, they were selected from a larger set of data according to the rules defined in section 6.6.1. From these, a total number of 4965 two-photon coincidences enter the calculations and the density matrix we obtain reads:

$$\rho = \begin{pmatrix} 0.04 & -0.02-0.05i & 0.04+i0.08 & 0 \\ -0.02+0.05i & \mathbf{0.49} & \mathbf{-0.44+0.05i} & -0.03-0.01i \\ 0.04-0.08i & \mathbf{-0.44-0.05i} & \mathbf{0.44} & 0.01-0.01i \\ 0 & -0.03+0.01i & 0.01+0.01i & 0.03 \end{pmatrix} \tag{6.60}$$

This result is visualized in figure 6.13 and can now be interpreted. The diagonal of the real part shows that 92.8% of the prepared entangled states are detected as two photons with orthogonal polarization. The bold printed elements in the density matrix are the ones constituting the Ψ^- Bell state. They should ideally take the values $+0.5$ on the diagonal and -0.5 at off-diagonal positions, representing an ideal phase of π between the two parts of the entangled state. The imaginary part of the matrix is supposed to be zero in all elements. Here, the rather big off-diagonal values $\pm 0.05i$ that we measured at positions ρ_{23} and ρ_{32} (second row, third value and third row, second value in the matrix) indicate a non-vanishing constant magnetic field with a magnitude of a few milligauss (or a corresponding differential Stark shift).

With the similarity to the Ψ^- Bell state being visibly clear, we can calculate the Fidelity F of our measured density matrix and the other measures of entanglement discussed in section 6.4:

Entanglement measure	Tomography result
Fidelity with Ψ^-_{PP}	$F = 0.902 \pm 0.009$
Concurrence	$C = 0.81 \pm 0.03$
Entanglement of Formation	$E_F = 0.73 \pm 0.04$
Negativity	$N = 0.412 \pm 0.009$
Logarithmic Negativity	$E_N = 0.867 \pm 0.014$

To calculate the errors we tried two different approaches. First, we applied the standard error propagation formalism starting with the squares of the individual elements of ρ. This way, we find the errors of these individual elements to be ± 0.02 (except $\Delta\rho_{11} = \Delta\rho_{44} = \pm 0.01$), which is an upper bound as this error calculation relies on statistically independent errors in the individual measurements. This is not given here as for example certain combinations of correlation probabilities always have to sum up to 1. The second method for the error calculation is a Monte-Carlo-simulation. The individual correlation counts are varied according to a binomial distribution. With this redistribution of the detection probabilities, we get errors for the individual matrix elements which are a factor of 2 smaller than those from the standard calculations. Especially the otherwise very large errors for the Concurrence C and Entanglement of Formation E_F seemed to be more realistic when using the Monte-Carlo-simulation. For this reason, all errors given in the table above are derived from the simulation.

The calculated matrix is based on correlation measurements which not only include statistical deviations, but also background signal from stray light, detector darkcounts and other noise sources. This is why the resulting matrix does not necessarily correspond to a physical state. In fact, if we extract the eigenvalues of ρ, we find $\lambda_1 = 0.917, \lambda_2 = 0.062, \lambda_3 = 0.029$ and $\lambda_4 = -0.008$. As not all eigenvalues are positive, the measured matrix does not represent a physical state. To overcome this problem, one can fit a physical matrix to the data which is as close as possible to the measured one. This is called a "maximum likelihood fit" and is discussed later in section 6.6.6. As the negative value λ_4

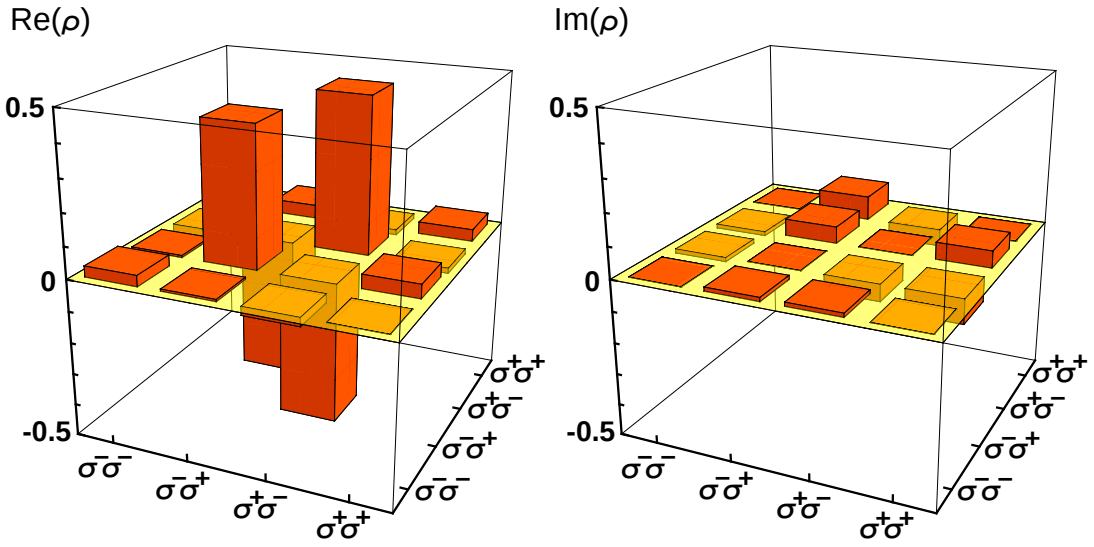

Figure 6.13: Real and imaginary part of the measured density matrix. From the two big bars on the diagonal and the two negative off-diagonal ones representing the phase relation between the photons, we calculate the Fidelity with the Ψ^- Bell-state to be $F = 0.901 \pm 0.009$.

is rather small, the measured density matrix is close to a physical state and therefore I preferred showing the original data.

Bell signal derived from the tomography

The density matrix ρ contains all information about the two-photon state. Therefore it is possible to "simulate" a Bell measurement as described in section 6.2. We take the measured density matrix, calculate the resulting correlation coefficients $E(\alpha, \beta)$ and the C.H.S.H.-Bell signal $S(\alpha, \alpha', \beta, \beta')$ and we get

Bell signal from tomography		
$\mathrm{E}(0\,^\circ, 22.5\,^\circ)$	$=$	-0.54 ± 0.03
$\mathrm{E}(0\,^\circ, -22.5\,^\circ)$	$=$	-0.69 ± 0.03
$\mathrm{E}(45\,^\circ, 22.5\,^\circ)$	$=$	-0.69 ± 0.04
$\mathrm{E}(45\,^\circ, -22.5\,^\circ)$	$=$	$+0.54 \pm 0.04$
$\mathrm{S}(0\,^\circ, 45\,^\circ, 22.5\,^\circ, -22.5\,^\circ)$	$=$	2.47 ± 0.04

These results are in good agreement with those obtained from the actual Bell measurements from section 6.6.3. This also shows the stability of the experimental setup as the individual data for these two different measurements were taken over a period of 11 days.

6.6.5 Coherence lifetime measurement

All entanglement data discussed so far had a separation of 0.8 μs between entangling laser pulse and the mapping process. As the atom lifetimes in the trap would in principle allow to extend the sequence to timescales of milliseconds or even seconds, the coherence time of the entangled state is of natural interest. A detailed knowledge of the decay behavior would even allow to draw conclusions about the quality of the entangled state right after its creation. To gain detailed information about the time dependence of the state, a series of full state tomographies with increasing pulse separation was measured. As the pulse separation could not be changed before each experimental run for technical reasons, the matrices had to be measured one after the other. To avoid systematic errors, the full data set was taken entirely in one day. Therefore, the individual density matrices contain less data and thus show larger statistical errors than the results presented in the previous section. In contrary to this, the data from the previous sections represents the average performance of the system over a period of almost two weeks.

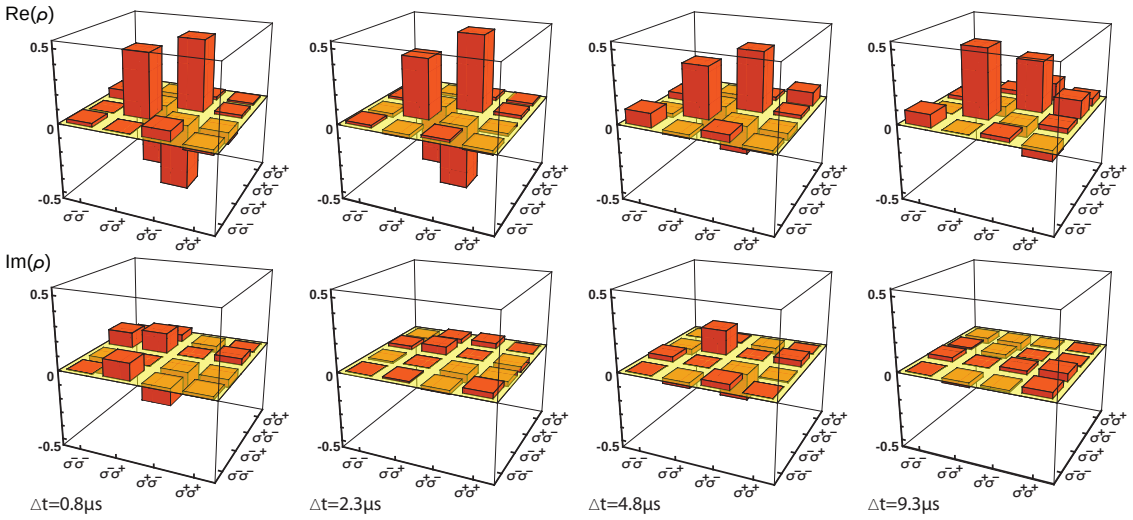

Figure 6.14: Measured density matrices at different pulse separations. While the diagonals mainly keep their shape, the off diagonal elements showing the coherence are partially rotated to the imaginary part while they decay.

Figure 6.14 shows the temporal evolution of the entangled two-photon state, displaying the density matrices $\rho(\Delta t = 0.8\,\mu\text{s})$, $\rho(2.3\,\mu\text{s})$, $\rho(4.8\,\mu\text{s})$ and $\rho(9.3\,\mu\text{s})$. Compared to the matrix obtained at $\Delta t = 0.8\,\mu$s pulse separation, the most evident change is the loss of phase coherence in the off-diagonal elements. While for the first two matrices with short evolution times the entanglement is almost perfectly maintained, we see a rotation into imaginary components in the third matrix at 4.8 μs. This can be explained by a static magnetic field with the effect that the second of the two subsequently emitted photons collects a phase relative to the first one. Looking at the absolute values, we also see that a part of the phase coherence is already lost and it vanishes almost completely in the fourth matrix at $\Delta t = 9.3\,\mu$s. In contrary, the elements along the diagonal of of the density matrix

keep their shape quite well until the end of the time interval. The majority of the photons therefore still show orthogonal polarization in the R/L detection basis representing σ^+ and σ^- in our experimental setup.

This result can also be clearly seen by calculating the Fidelitiy with the $|\Psi^-_{\mathrm{PP}}\rangle$ state from equation 6.2 for each of the matrices. The obtained values are plotted as a function of Δt in figure 6.15. Starting with $F(0.8\,\mu\mathrm{s}) = 0.94$, it takes about $8\,\mu$s to approach 0.5, which is the limit value separating entangled states from those that could also be explained classically. To obtain a characteristic decay time, we fit a Gauss-function with an offset of 0.5 to the Fidelity. Assuming a Gaussian noise source in the entangled state, the Fidelity consisting of linear combinations of the correlation probabilities will also show a Gaussian decay, and thus the fit should be a good approximation (see for instance in [28]). The decay time is determined to be $\tau = 4.5 \pm 0.3\,\mu$s. The choice for the offset value of the fit is not definite. While our data clearly approaches $F = 0.5$ on the considered timescale, the final value for a real random state with an equal probability distribution along the diagonal of the density matrix would be $F = 0.25$. This indicates that there should be a second, much longer timescale, which is not resolved in our data.

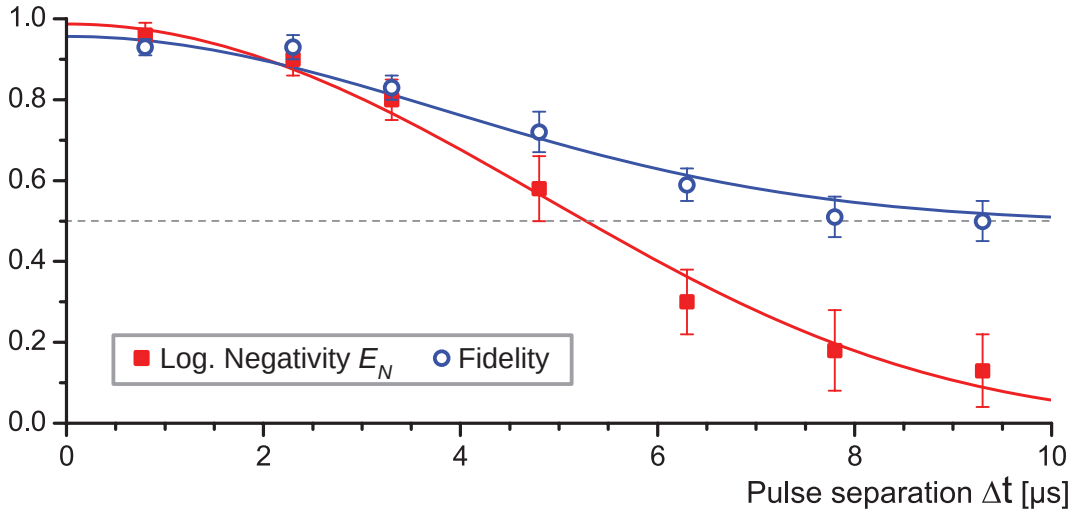

Figure 6.15: Coherence time of the entangled state. On this series of tomography measurements, the plot of the Logarithmic Negativity indicates that the entanglement is lost within $10\,\mu$s. The Fidelity settling at $F = 0.5$ however shows that in the end the state is still not just a random statistical distribution, which would have $F = 0.25$.

As the Fidelity is not a true measure of entanglement, we also plot the Logarithmic Negativity E_N. A Gauss-fit is applied to the Negativity N and then scaled to E_N. While it is not obvious to fit a Gauss function to N as it is calculated via the partial transpose of the density matrix (see section 6.4), we see that the approximation fits quite well to the data and gives a reasonable number for the decay timescale τ. The determined decay time is $\tau = 5.7 \pm 0.2\,\mu$s, which is longer than the one obtained from the Fidelity. This could be explained with a partial state rotation due to magnetic fields which does not affect the entanglement itself, but reduces the Fidelity with the Ψ^- Bell state.

6.6.6 Maximum likelihood fits

As already discussed in section 6.6.4, a density matrix representing a physical state will only show positive eigenvalues. Although the negative eigenvalues in the measured density matrices are usually small, it is interesting to approximate the data with a maximum likelihood fit and compare the results. We tried two mathematical approaches for these fits.

The first approach is an implementation of the recipe described in [91]. First, a formula for an explicitly "physical", non-negative definite density matrix is generated. The property of non-negative definiteness for any matrix $\hat{\mathcal{G}}$ is written mathematically as

$$\langle\Psi|\hat{\mathcal{G}}|\Psi\rangle \geq 0 \quad \forall\,|\Psi\rangle. \tag{6.61}$$

Defining $|\Psi'\rangle = \hat{T}|\Psi\rangle$ with the Hermitian matrix $\hat{T}$, we find

$$\langle\Psi'|\Psi'\rangle = \langle\Psi|\hat{T}^\dagger\hat{T}|\Psi\rangle \geq 0. \tag{6.62}$$

This means that any matrix of the form $\hat{\mathcal{G}} = \hat{T}^\dagger\hat{T}$ is non-negative definite. Thus we can write a physical density matrix as

$$\hat{\rho}_p = \hat{T}^\dagger\hat{T}/\mathrm{tr}\{\hat{T}^\dagger\hat{T}\}. \tag{6.63}$$

For our two-qubit state the $\hat{T}$ matrix is described by 16 independent real parameters. We now need to find the optimum set of these parameters to find $\hat{T}$ and then calculate $\hat{\rho}_p$. To quantify how our constructed density matrix compares to the one obtained from the data, a "likelihood function" is introduced as a function of the 16 parameters. For our purposes this function is the formula for the Fidelity. The optimum density matrix can be found maximizing this "likelihood function" with standard numerical optimization techniques.

The second method to make the measured density matrix physical is more straightforward. We calculate the eigenvectors of our matrix and recompose it from these vectors omitting those with a corresponding negative eigenvalue (this is usually only the case for one of the eigenvectors). We now have to normalize the matrix again to obtain a physical state representation.

If we take the matrix at $\Delta t = 0.8\,\mu$s, apply the fit and calculate the entanglement measures we are interested in, we can compare the results in the following table:

Entanglement measure	Raw matrix	Max.likelihood	Neg. EV cut
Fidelity with Ψ^-_{PP}	0.901	0.900	0.894
Concurrence	0.807	0.822	0.809
Entanglement of Formation	0.732	0.751	0.734
Negativity	0.412	0.410	0.404
Logarithmic Negativity	0.867	0.864	0.855

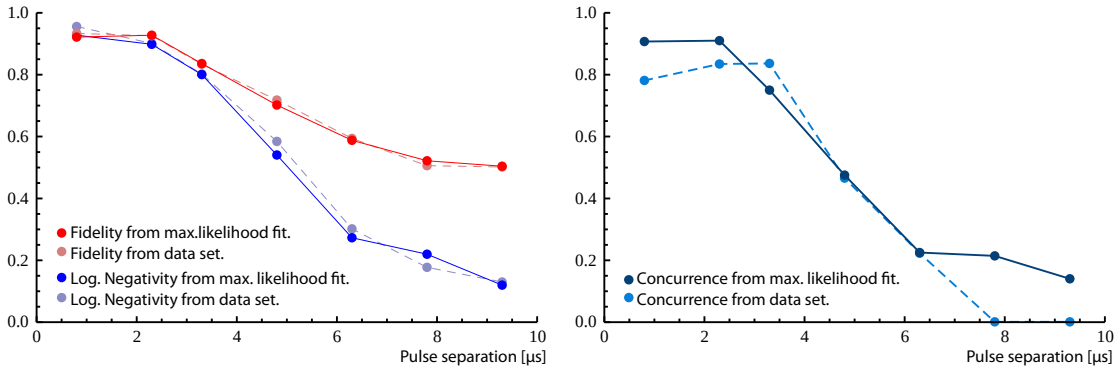

Figure 6.16: Maximum likelihood fits. The plotted curves compare entanglement measures obtained from a maximum likelihood fit (solid lines) to those from the raw data (light dashed lines). While the differences are only minor for the Fidelity and the Logarithmic Negativity, the values of the Concurrence show significant deviations.

As expected, there are only minor differences between the original data and the results from the fitted matrix. This is mainly because the matrix contains enough correlation statistics to keep the negative eigenvalues small. As we will see, this looks different for the series of density matrices from the lifetime measurement. Each of the matrices is reconstructed from about ≈ 1200 measured two-photon correlations and thus contains larger statistical errors than the data from section 6.6.4.

Figure 6.16 shows several entanglement measures plotted as a function of temporal pulse separation and compares the values from the likelihood fit to the ones obtained directly from the data. While the curves for the Fidelity and the Logarithmic Negativity do not show significant deviations, the Concurrence clearly shows a different behavior. The curve obtained via the calculations from the raw data shows an increase of C for the first three points, which, compared to the curves of the other entanglement measures, seems not realistic. In contrary, the decrease of C obtained from the likelihood fit agrees well with the other curves. For this reason, the values from the fit for the two points at pulse separations $7.8\,\mu$s and $9.3\,\mu$s also seem more reliable. The benefits from a maximum likelihood fit apparently depend on the type of entanglement measure and its sensitivity to negative eigenvalues. Especially when your set of data is not clean enough or does not contain sufficient statistics, one can learn more about the system from the likelihood fits.

6.6.7 Limitations in the current system

With the data presented in this thesis, atom-photon entanglement with a single atom trapped in a high finesse cavity and the mapping to a two-photon entangled state was successfully demonstrated. Although the measured degree of entanglement is quite high, there is room for improvements. Two main issues should be addressed. First, we could work on the purity of the entangled state, as the Fidelity with the Ψ^- Bell state could still be enhanced, and second, we could think of ways to extend the coherence time.

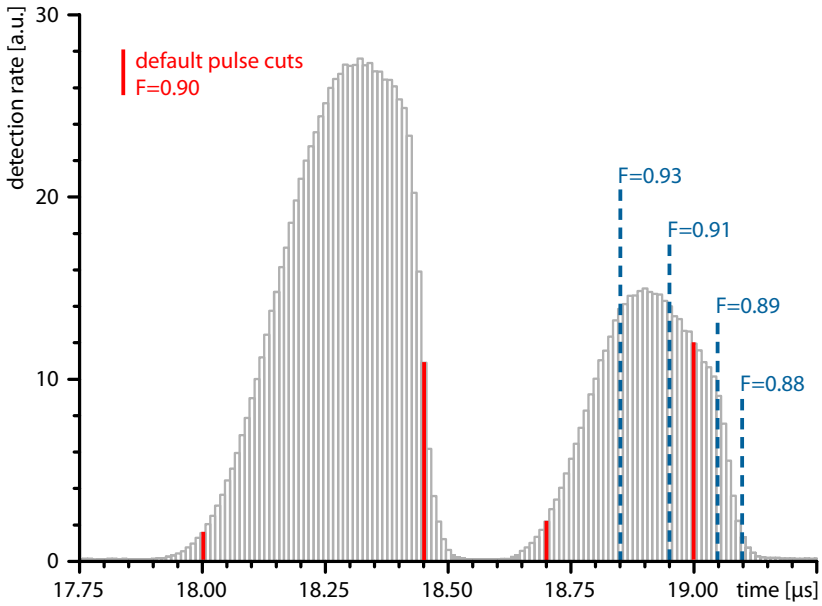

Figure 6.17: Fidelity values obtained from different subsets of the data. An increasing probability of a second photon detection towards the end of the mapping pulse influences the quality of the obtained entanglement.

If we think about improvements on the quality of the entanglement, we find several limiting imperfections in the system. But besides further optimization of the detection setup, suppression of background signal or improved pump polarizations, there is one point I would like to discuss here in more detail. Looking at the detection time histogram for the pulses in figure 6.17, we see that the tails of the pulses were cut before evaluating the data. This was originally done reasoning that the signal-to-noise ratio in these regions is not good enough. However, when we cut the mapping pulse at earlier positions, we find that the Fidelity increases and reaches even a value of $F = 0.93$ when only the first 40% of the detected photons are included. This significant improvement can be explained with an increasing probability of emitting two photons in the mapping process towards the end of the pulse. The possibility of having a second photon in this pulse is mainly given by possible excitation of the F'=0 state, which is only 72 MHz detuned from the transition addressed by the mapping laser. As this is one of the main limitations in the system, it will for sure be advantageous to perform future experiments using this protocol on the $D1$-line of ^{87}Rb, which has no F'=0 state in the vicinity. Another approach that could be worth trying is to use a short excitation (π-)pulse instead of the vSTIRAP in the mapping process, which will not allow for multiple excitations. The application of 3 ns short excitation pulses to create a single-photon source was just demonstrated successfully in our group [55].

Concerning the lifetime of the entangled state, we must state that there are dephasing mechanisms in our system. They lead to a rather short coherence time compared to timescales of milliseconds observed in other experiments with atoms in dipole traps [97].

The reasons for the decoherence could be fluctuations of the magnetic field, destroying the phase relation in the time evolution of the two atomic states $|1,-1\rangle$ and $|1,+1\rangle$. With a decay time shorter than $10\,\mu$s, these fluctuations should be on timescales of at least 100 kHz. Once verified as the source of noise, one could eliminate the fluctuations with an active control of the magnetic field. But the phase noise could also have a different origin. Time-dependent differential Stark shifts between the two involved atomic states could also explain the observed behavior, as they would mimic the presence of a magnetic field. As discussed in section 6.5.4, circular components in the trapping light lead to differential energy shifts between the Zeeman substates. For this reason, the polarization of the intracavity 785 nm trap was changed from circular to linear light. The main trap at 1030 nm is also linear polarized at the entrance of the vacuum chamber, defined by a polarizing beam cube. Nevertheless, birefringence of the glass windows may add a small circular component to the trap light at the atom's position. As discussed in section 6.5.4, a trap composed of circular polarized light should lead to a differential Stark shift of 2.4 MHz. From this we can infer that a 10% component of circular light leads to a differential state rotation on the same timescale as the observed coherence decay. If we now take into account, that a rather hot atom will oscillate with characteristic frequencies of several 100 kHz in the standing-wave trap, the resulting absolute and differential Stark shift will also show this time-dependence. This would have the same effect on the entanglement lifetime as magnetic field fluctuations. As the trap light polarization has such an impact at this point, carefully eliminating circular components should help improving the entanglement lifetime.

7 Summary and outlook

The experiments with single atoms and photons in a cavity described in this thesis were carried out with an apparatus constituting a second generation of atom-cavity systems. The first generation experiment set up in our group led to the creation of single photons [51], their characterization via two-photon interference [75; 54], a single-photon source with alternating polarization [53] and atom-photon entanglement [98].

However, these experiments were always limited by the rather short interaction time between the freely falling atom and the cavity as well as the fact that the presence of a coupled atom was always probabilistic. With the second generation setup, we now provide an additional trap for the atom, extending the interaction time to several ten seconds with support of the cavity-cooling forces [48]. Even though such a trap adds more complexity to the physical system, almost every application for the atom-cavity system significantly benefits from the long trapping times. As shown with our single-photon source, we were able to emit extended streams of up to 300 000 single photons from just one trapped atom [61]. In addition, the signal rates even allow for their characterization via an antibunching test within a small fraction of the average trapping time.

The new results from this thesis now show additional advances concerning two aspects of the experiment. The first is that with the installation of the camera system, we are now able to detect single trapped atoms independent from the cavity on an orthogonal axis. This increases the amount of control we have over the system to a new level and allows for precise alignment of its individual components. With this improved technological basis, the application of protocols which are critical to imbalanced trap or pump beam configurations became possible, as demonstrated now with the successful realization of our entanglement protocol with a trapped atom. It constitutes the second big advance as it upgrades the atom-cavity system to a quantum interface suitable for future quantum networking applications. The cavity make the information transfer from atoms to photons efficient and, in our case, allows the application of a quantum state mapping from an atom to a single photon. With a measured Fidelity of up to 93%, the entanglement created with our protocol is very close to the ideal state. However, fluctuations of the relative energies of the contributing atomic states limit the coherence time in the current system. This can be overcome by eliminating remaining laser polarization impurities and magnetic field instabilities. The results also show that the application of a quantum information processing protocol can be combined with long atom trapping times. The near-permanent presence of an atom in the cavity makes the applied protocol in principle deterministic and opens new possibilities for even more complex experiments.

The cavity not only enhances the efficiency of quantum information transfers, but can also make them reversible. This allows to emit time-symmetric photon wave-packets from one cavity, which can be coupled into another “receiving” cavity, thereby mapping the photon state onto a single atom [45]. An experiment demonstrating this bidirectionality

would substantiate the versatility of cavities as a quantum interface and their usefulness for future quantum networks. With the recent completion of a second atom-cavity system similar to the one described in this theses, it is now possible to start with experiments towards such quantum networks in the group of Prof. Rempe. In a first step, running both systems as single photon sources, the indistinguishability of photons emitted from these two systems has to be tested in a two-photon interference experiment showing the characteristic Hong-Ou-Mandel dip in the correlations [74; 75]. Next, the individually trapped single atoms in the two systems can be entangled by applying the same scheme used for the atom-photon entanglement from this thesis and subsequently measuring the two emitted photons in a Bell state basis. Such a photon-mediated remote atom-atom entanglement was recently demonstrated in an experiment with two ions in separated traps [43; 90]. Including high finesse cavities could not only speed up the event rates, but also significantly increase the photon collection efficiency such that quantum information processing at larger scales becomes realistic [44]. With photons mediating the entanglement, one could in principle extend the separation of two atom-cavity systems to large distances and measure a loophole-free violation of a Bell inequality to test quantum mechanics [99]. Another proposed protocol allows a quantum state teleportation from one atom-cavity system to the other [100].

Apart from experiments with multiple atom-cavity systems, one could also extend the systems themselves by increasing the number of atoms in the dipole trap. Using a chain of single trapped atoms representing a quantum register, a cavity could mediate quantum gates between the qubits [101]. Some of the requirements of such a system can already be fulfilled. While the possibility to deterministically couple single atoms to the cavity was shown with our system [58], other experiments demonstrated the possibility to arbitrarily sort an array of single atoms with the use of two orthogonal standing-wave dipole traps [102].

Based on what has been achieved so far, cavities promise to play a decisive role in future realizations of quantum networks. Their particular advantages are not restricted to atomic systems. They also apply to any other type of qubit, such as quantum dots or superconducting circuits.

A ^{85}Rb and ^{87}Rb transition strengths

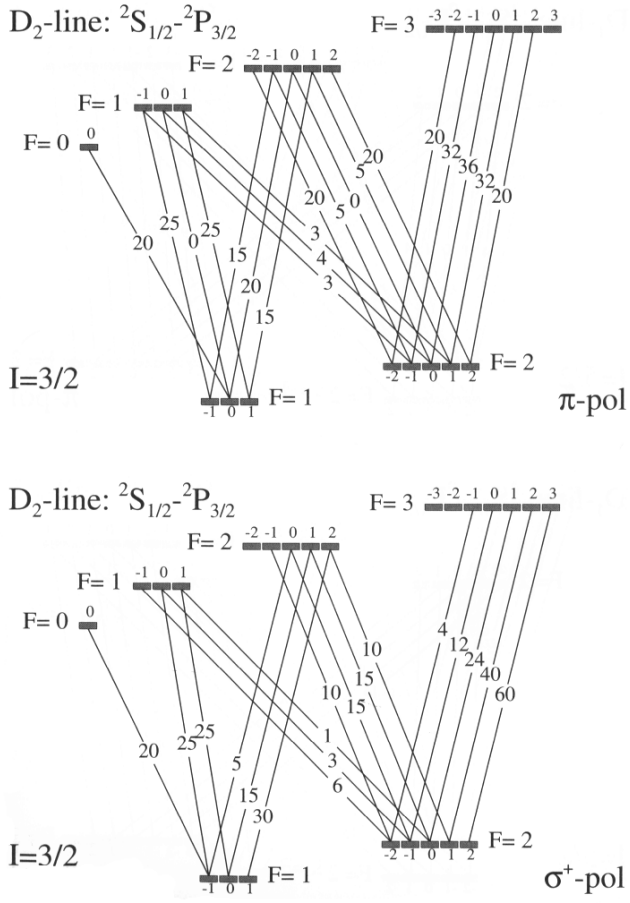

Figure A.1: Relative transition strenghts of the D_2-line of ^{87}Rb. Taken from the book **Laser cooling and trapping** [82]

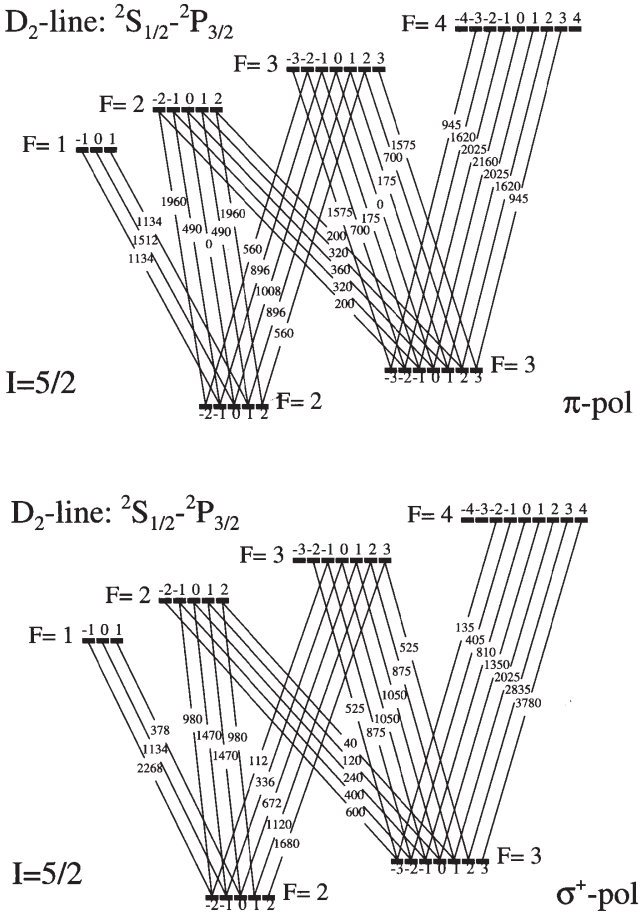

Figure A.2: Relative transition strenghts of the D_2-line of ^{85}Rb. Taken from the book **Laser cooling and trapping** [82]

Bibliography

[1] S. J. Freedman and J. F. Clauser. Experimental test of local hidden-variable theories. *Phys. Rev. Lett.* **28**, 938–941 (1972).

[2] A. Aspect, P. Grangier, and G. Roger. Experimental tests of realistic local theories via bell's theorem. *Phys. Rev. Lett.* **47**, 460–463 (1981).

[3] Z. Y. Ou and L. Mandel. Violation of Bell's Inequality and Classical Probability in a Two-Photon Correlation Experiment. *Phys. Rev. Lett.* **61**, 50 – 53 (1988).

[4] Y. H. Shih and C. O. Alley. New Type of Einstein-Podolsky-Rosen-Bohm experiment using pairs of light quanta produced by optical parametric down conversion. *Phys. Rev. Lett.* **61**, 2921 – 2924 (1988).

[5] J. S. Bell. *Speakable and Unspeakable in Quantum Mechanics*. Cambridge University Press, Oxford, (1987).

[6] J. S. Bell. On the Einstein Podolsky Rosen paradox. *Physics* **1**, 195 (1964).

[7] R. Feynman. Simulating physics with computers. *Int. J. Theor. Phys.* **21**, 467–488 (1982).

[8] D. Deutsch. Quantum theory, the church-turing principle and the universal quantum computer. *Proc. R. Soc. Lond. A* **400**, 97–117 (1985).

[9] D. Deutsch. Quantum computational networks. *Proc. R. Soc. Lond. A* **425**, 79–90 (1989).

[10] P. Shor. Algorithms for quantum computation: Discrete logarithms and factoring. In *Proc. 35th Annual Symposium on Foundations of Computer Science*. IEEE Press, (1994).

[11] Lov K. Grover. A fast quantum mechanical algorithm for database search. *Proc. 28 Annual ACM Symposium on the Theory of Computing* pages 212 – 219 (1996).

[12] E. Knill, R. Laflamme, and G. J. Milburn. A scheme for efficient quantum computing with linear optics. *Nature* **409**, 46–52 (2001).

[13] D. Greenberger, M. A. Horne, and Zeilinger A. *Going beyond Bell's Theorem*, volume 1. Kluwer, (1989).

[14] D. Bouwmeester, J. W. Pan, M. Daniell, H. Weinfurter, and A. Zeilinger. Observation of Three-Photon Greenberger-Horne-Zeilinger Entanglement. *Phys. Rev. Lett.* **82**, 1345–1349 (1999).

[15] J.-W. Pan, D. Bouwmeester, M. Daniel, H. Weinfurter, and A. Zeilinger. Experimental Test of Quantum Nonlocality in Three-Photon Greenberger-Horne-Zeilinger Entanglement. *Nature* **403**, 515–519 (2000).

[16] J. L. O'Brien, G. J. Pryde, A. G. White, T. C. Ralph, and D. Branning. Demonstration of an all-optical quantum controlled-NOT gate. *Nature* **426**, 264–267 (2003).

[17] T. B. Pittman, M. J. Fitch, B. C Jacobs, and J. D. Franson. Experimental controlled-NOT logic gate for single photons in the coincidence basis. *Phys. Rev. A* **68**, 032316 (2003).

[18] S. Gasparoni, J.-W. Pan, P. Walther, T. Rudolph, and A. Zeilinger. Realization of a Photonic Controlled-NOT Gate Sufficient for Quantum Computation. *Phys. Rev. Lett.* **93**, 020504 (2004).

[19] B. Julsgaard, J. Sherson, I. Cirac, J. Fiurassek, and E. S. Polzik. Experimental demonstration of quantum memory for light. *Nature* **432**, 482 – 486 (2004).

[20] D. Jaksch, J. I. Cirac, P. Zoller, S. L. Rolston, R. Côté, and M. D. Lukin. Fast Quatum Gates for Neutral Atoms. *Phys. Rev. Lett.* **85**, 2208–2211 (2000).

[21] D. Jaksch, H.-J. Briegel, J. I. Cirac, C. W. Gardiner, and P. Zoller. Entanglement of Atoms via Cold Controlled Collisions. *Phys. Rev. Lett.* **82**, 1975 – 1978 (1999).

[22] J. I. Cirac and P. Zoller. How to Manipulate Cold Atoms. *Science* **301**, 176–177 (2003).

[23] C. Monroe, D. M. Meekhof, B. E. King, W. M. Itano, and D. J. Wineland. Demonstration of a Fundamental Quantum Logic Gate. *Phys. Rev. Lett.* **75**, 4714–4717 (1995).

[24] F. Schmidt-Kaler, H. Häffner, M. Riebe, S. Gulde, G. P. T. Lancaster, T. Deuschle, C. Becher, C. F. Roos, J. Eschner, and R. Blatt. Realization of the Cirac-Zoller controlled-NOT quantum gate. *Nature* **422**, 408–411 (2003).

[25] A. S. Sorensen and K. Molmer. Quantum Computation with Ions in Thermal Motion. *Phys. Rev. Lett.* **82**, 1971–1974 (1999).

[26] J. I. Cirac and P. Zoller. Quantum Computations with Cold Trapped Ions. *Phys. Rev. Lett.* **74**, 4091 (1995).

[27] C. F. Roos, G. P. T. Lancaster, M. Riebe, H. Häffner, W. Hänsel, S. Gulde, C. Becher, J. Eschner, F. Schmidt-Kaler, and R. Blatt. Bell states of atoms with ultralong lifetimes and their tomographic state analysis. *Phys. Rev. Lett.* **92**, 220402 (2004).

[28] H. Häffner, F. Schmidt-Kaler, W. Hänsel, C. F. Roos, T. Körber, M. Chwalla, M. Riebe, J. Benhelm, U. D. Rapol, C. Becher, and R. Blatt. Robust entanglement. *Applied Physics B: Lasers and Optics* **81**, 151–153 (2005).

[29] C. A. Sackett, D. Kielpinski, B. E. King, C. Langer, V. Meyer, C. J. Myatt, M. Rowe, Q. A. Turchette, W. M. Itano, D. J. Wineland, and C. Monroe. Experimental Entanglement of Four Particles. *Nature* **404**, 256–259 (2000).

[30] D. Leibfried, E. Knill, S. Seidelin, J. Britton, R. B. Blakestad, J. Chiaverini, D. B. Hume, W. M. Itano, J. D. Jost, C. Langer, R. Ozeri, R. Reichle, and D. J. Wineland. Creation of a six-atom "Schrödinger cat" state. *Nature* **438**, 639–642 (2005).

[31] J. I. Cirac and P. Zoller. A Scalable Quantum Computer with Ions in an Array of Microtraps. *Nature* **404**, 479–581 (2000).

[32] D. Kielpinski, C.R. Monroe, and D.J. Wineland. Architecture for a Large-Scale Ion-Trap Quantum Computer. *Nature* **417**, 709 – 711 (2002).

[33] R. Blatt and D. Wineland. Entangled states of trapped atomic ions. *Nature* **453**, 1008–1015 (2008).

[34] W. K. Hensinger, S. Olmschenk, D. Stick, D. Hucul, M. Yeo, M. Acton, L. Deslauriers, C. Monroe, and J. Rabchuk. T-junction ion trap array for two-dimensional ion shuttling, storage and manipulation. *Appl. Phys. Lett.* **88**, 034101 (2006).

[35] S. Seidelin, J. Chiaverini, R. Reichle, J. J. Bollinger, D. Leibfried, J. Britton, J. H. Wesenberg, R. B. Blakestad, R. J. Epstein, D. B. Hume, W. M. Itano, J. D. Jost, C. Langer, R. Ozeri, N. Shiga, and D. J. Wineland. Microfabricated surface-electrode ion trap for scalable quantum information processing. *Phys. Rev. Lett.* **96**, 253003 (2006).

[36] D. Stick, W. K. Hensinger, S. Olmschenk, M. J. Madsen, K. Schwab, , and C. Monroe. Ion trap in a semiconductor chip. *Nature Physics* **2**, 36–39 (2006).

[37] L. Deslauriers, S. Olmschenk, D. Stick, W. K. Hensinger, J. Sterk, and C. Monroe. Scaling and suppression of anomalous heating in ion traps. *Phys. Rev. Lett.* **97**, 103007 (2006).

[38] J. Labaziewicz, Y. Ge, P. Antohi, D. Leibrandt, K. R. Brown, and I. L. Chuang. Suppression of heating rates in cryogenic surface-electrode ion traps. *Phys. Rev. Lett.* **100**, 013001 (2008).

[39] L.-M. Duan, M. D. Lukin, J. I. Cirac, and P. Zoller. Long-distance quantum communication with atomic ensembles and linear optics. *Nature* **414**, 413–418 (2001).

[40] B. B. Blinov, D. L. Moehring, L.-M. Duan, and C. Monroe. Observation of entanglement between a single trapped atom and a single photon. *Nature* **428**, 153–157 (2004).

[41] D. L. Moehring, M. J. Madsen, B. B. Blinov, and C. Monroe. Experimental Bell inequality violation with an atom and a photon. *Phys. Rev. Lett.* **93**, 090410 (2004).

[42] J. Volz, M. Weber, D. Schlenk, W. Rosenfeld, J. Vrana, K. Saucke, C. Kurtsiefer, and H. Weinfurter. Observation of entanglement of a single photon with a trapped atom. *Phys. Rev. Lett.* **96**, 030404 (2006).

[43] D. L. Moehring, P. Maunz, S. Olmschenk, K. C. Younge, D. N. Matsukevich, L.-M. Duan, and C. Monroe. Entanglement of single-atom quantum bits at a distance. *Nature* **449**, 68–71 (2007).

[44] E. T. Campbell and S. C. Benjamin. Measurement based entanglement under conditions of extreme photon loss. *arXiv:0710.4352v4 [quant-ph]* , (2007).

[45] J. I. Cirac, P. Zoller, H. J. Kimble, and H. Mabuchi. Quantum State Transfer and Entanglement Distribution Among Distant Nodes in a Quantum Network. *Phys. Rev. Lett.* **78**, 3221–3224 (1997).

[46] H. Mabuchi, Q. A. Turchette, M. S. Chapman, and H. J. Kimble. Real-Time Detection of Individual Atoms Falling Through a High-Finesse Optical Cavity. *Optics Lett.* **21**, 1393 (1996).

[47] P. Maunz, T. Puppe, I. Schuster, N. Syassen, P. W. H. Pinkse, and G. Rempe. Cavity cooling of a single atom. *Nature* **428**, 50–52 (2004).

[48] S. Nußmann, K. Murr, M. Hijlkema, B. Weber, A. Kuhn, and G. Rempe. Vacuum-stimulated cooling of single atoms in three dimensions. *Nature Physics* **1**, 122 (2005).

[49] K. Murr, S. Nußmann, T. Puppe, M. Hijlkema, B. Weber, S. Webster, A. Kuhn, and G. Rempe. Three-dimensional cavity cooling and trapping in an optical lattice. *Phys. Rev. Lett.* **96**, 253001 (2006).

[50] A. D. Boozer, A. Boca, R. Miller, T. E. Northup, and H. J. Kimble. Cooling to the ground state of axial motion for one atom strongly coupled to an optical cavity. *Phys. Rev. Lett.* **97**, 083602 (2006).

[51] A. Kuhn, M. Hennrich, and G. Rempe. Deterministic single-photon source for distributed quantum networking. *Phys. Rev. Lett.* **89**, 067901 (2002).

[52] J. McKeever, A. Boca, A. D. Boozer, R. Miller, J. R. Buck, A. Kuzmich, and H. J. Kimble. Deterministic Generation of Single Photons from One Atom Trapped in a Cavity. *Science* **303**, 1992 – 1994 (2004).

[53] T. Wilk, S. C. Webster, H. P. Specht, G. Rempe, and A. Kuhn. Polarization-controlled single photons. *Phys. Rev. Lett.* **98**, 063601 (2007).

[54] T. Legero, T. Wilk, M. Hennrich, G. Rempe, and A. Kuhn. Quantum beat of two single photons. *Phys. Rev. Lett.* **93**, 070503 (2004).

[55] J. Bochmann, M. Mücke, G. Langfahl-Klabes, C. Erbel, B. Weber, H. P. Specht, D. L. Moehring, and G. Rempe. Fast excitation and photon emission of a single-atom-cavity system. *arXiv:0806.2600v1 [quant-ph]* , (2008).

[56] J. McKeever, A. Boca, A. D. Boozer, J. R. Buck, and H. J. Kimble. Experimental realization of a one-atom laser in the regime of strong coupling. *Nature* **425**, 268–270 (2003).

[57] M. Keller, B. Lange, K. Hayasaka, W. Lange, and H. Walther. Continuous generation of single photons with controlled waveform in an ion-trap cavity system. *Nature* **431**, 1075–1078 (2004).

[58] S. Nußmann, M. Hijlkema, B. Weber, F. Rohde, G. Rempe, and A. Kuhn. Sub-Micron Positioning of Single Atoms in Micro Cavities. *Phys. Rev. Lett.* **95**, 173602 (2005).

[59] J. A. Sauer, K. M. Fortier, M. SW. Chang, C. D. Hamley, and M. S. Chapman. Cavity QED with optically transported atoms. *Phys. Rev. A* **69**, 051804(R) (2004).

[60] M. Khudaverdyan, W. Alt, I. Dotsenko, T. Kampschulte, K. Lenhard, A. Rauschenbeutel, S. Reick, K. Schörner, A. Widera, and D. Meschede. Controlled insertion and retrieval of atoms coupled to a high-finesse optical resonator. *New J. Phys.* **10**, 073023+ (2008).

[61] M. Hijlkema, B. Weber, H. P. Specht, S. C. Webster, A. Kuhn, and G. Rempe. A single-photon server with just one atom. *Nature Physics* **3**, 253–255 (2007).

[62] H. J. Kimble. The quantum internet. *Nature* **453**, 1023–1030 (2008).

[63] Stefan Nußmann. *Kühlen und Positionieren eines Atoms in einem optischen Resonator*. Dissertation, Max-Planck Institut für Quantenoptik, (2005).

[64] M. Hijlkema. *Single photons from a single atom trapped in a high-finesse optical cavity*. Dissertation, Max-Planck-Institut für Quantenoptik und Technische Universität München, (2007).

[65] E. T. Jaynes and F. W. Cummings. Comparison of Quantum and Semiclassical Radiation Theories with Application to the Beam Maser. *Proc. IEEE* **51**, 89–109 (1963).

[66] B. Weber. Transport von Atomen in einer optischen Dipolfalle. Diplomathesis, Max-Planck-Institut für Quantenoptik und Technische Universität München, (2002).

[67] F. Rohde. Ein optischer Resonator hoher Finesse als Atomdetektor. Diplomathesis, Max-Planck-Institut für Quantenoptik und Technische Universität München, (2003).

[68] R. Grimm, M. Weidemuller, and Y. B. Ovchinnikov. Optical dipole traps for neutral atoms. *Adv. At. Mol. Opt. Phys.* **42**, 95–170 (2000).

[69] M. Hennrich. *Kontrollierte Erzeugung einzelner Photonen in einem optischen Resonator hoher Finesse*. Dissertation, Max-Planck-Institut für Quantenoptik und Technische Universität München, (2003).

[70] T. Legero. *Zeitaufgelöste Zwei-Photonen-Interferenz*. Dissertation, Max-Planck-Institut für Quantenoptik und Technische UniversitätMünchen, (2005).

[71] T. Wilk. *Single-Atom Single-Photon Quantum Interface*. Dissertation, Max-Planck-Institut für Quantenoptik und Technische Universität München, (2008).

[72] J. Dalibard and C. Cohen-Tannoudji. Dressed-Atom Approach to Atomic Motion in Laser Light: The Dipole Force Revisited. *J. Opt. Soc. Am. B* **2**, 1707 (1985).

[73] R. Taïeb, R. Dum, J. I. Cirac, P. Marte, and P. Zoller. Cooling and localization of atoms in laser-induced potential wells. *Phys. Rev. A* **49**, 4876–4887 (1994).

[74] C. K. Hong, Z. Y. Ou, and L. Mandel. Measurement of Subpicosecond Time Intervals between Two Photons by Interference. *Phys. Rev. Lett.* **59**, 2044 – 2046 (1987).

[75] T. Legero, T. Wilk, A. Kuhn, and G. Rempe. Time-Resolved Two-Photon Quantum Interference. *Appl. Phys. B* **77**, 797–802 (2003).

[76] A. Kuhn and G. Rempe. Optical Cavity QED: Fundamentals and application as a Single-Photon Light Source. *Proceedings of the Varenna School on 'Experimental Quantum Information'* , (2001).

[77] M. Fleischhauer and M. D. Lukin. Dark-State Polaritons in Electromagnetically Induced Transparency. *Phys. Rev. Lett.* **84**, 5094–5097 (2000).

[78] L.-M. Duan, A. Kuzmich, and H. J. Kimble. Cavity qed and quantum-information processing with "hot" trapped atoms. *Physical Review A (Atomic, Molecular, and Optical Physics)* **67**, 032305 (2003).

[79] B. Darquié, M. P. A. Jones, J. Dingjan, J.Beugnon, S. Bergamini, Y. Sortais, G. Messin, A. Browaeys, and P. Grangier. Controlled single-photon emission from a single trapped two-level atom. *Science* **309**, 454–456 (2005).

[80] T. Müller. Abbildung einzelner Atome in einem optischen Resonator høchster Finesse. Diplomathesis, Max-Planck-Institut für Quantenoptik und Technische Universität München, (2007).

[81] B. B. Blinov, R. N. Kohn, Jr., M. J. Madsen, P. Maunz, D. L. Moehring, and C. Monroe. Broadband laser cooling of trapped atoms with ultrafast laser pulses. *J. Opt. Soc. Am. B* **23**, 1170–1173 (2006).

[82] H. J. Metcalf and P. van der Straten. *Laser Cooling and Trapping*. Springer, New York, (1999).

[83] A. Einstein, B. Podolsky, and N. Rosen. Can Quantum-Mechanical Description of Physical Reality Be Considered Complete? *Phys. Rev.* **47**, 777–780 (1935).

[84] A. Aspect. Bell's theorem : The naive view of an experimentalist. In R.A. Bertlmann and A. Zeilinger, editors, *Quantum [Un]speakables - From Bell to Quantum information*. Springer, (2002).

[85] J. F. Clauser, M. A. Horne, A. Shimony, and R. A. Holt. Proposed experiment to test local hidden-variable theories. *Phys. Rev. Lett.* **23**, 880+ (1969).

[86] P. R. Tapster, J. G. Rarity, and P. C. M. Owens. Violation of bell's inequality over 4 km of optical fiber. *Phys. Rev. Lett.* **73**, 1923–1926 (1994).

[87] W. Tittel, J. Brendel, B. Gisin, T. Herzog, H. Zbinden, and N. Gisin. Experimental Demonstration of Quantum-Correlations over More Than 10 Kilometers. *Phys. Rev. A* **57**, 3229 (1998).

[88] G. Weihs, T. Jennewein, C. Simon, H. Weinfurter, and A. Zeilinger. Violation of Bell's inequality under strict Einstein locality conditions. *Phys. Rev. Lett.* **81**, 5039–5043 (1998).

[89] M. A. Rowe, D. Kielpinski, V. Meyer, C. A. Sackett, W. M. Itano, C. Monroe, and D. J. Wineland. Experimental violation of a Bell's inequality with efficient detection. *Nature* **409**, 791–794 (2001).

[90] D. N. Matsukevich, P. Maunz, D. L. Moehring, S. Olmschenk, and C. Monroe. Bell inequality violation with two remote atomic qubits. *Phys. Rev. Lett.* **100**, 150404 (2008).

[91] J. B. Altepeter, E. R. Jeffrey, and P. G. Kwiat. Photonic state tomography. *Adv. At. Mol. Opt. Phys.* **52**, 105–159 (2005).

[92] G. G. Stokes. On the composition and resolution of streams of polarized light from different sources. *Trans. Cambridge Philos. Soc.* **9**, 399–416 (1852).

[93] M. B. Plenio and S. Virmani. An introduction to entanglement measures. *Quant. Inf. Comp.* **7**, 1–51 (2007).

[94] S. Hill and W. K. Wootters. Entanglement of a pair of quantum bits. *Phys. Rev. Lett.* **78**, 5022–5025 (1997).

[95] W. K. Wootters. Entanglement of formation of an arbitrary state of two qubits. *Phys. Rev. Lett.* **80**, 2245–2248 (1998).

[96] W.Wootters. Entanglement of Formation and Concurrence. *Quant. Inf. Comp* **1**, 27–44 (2001).

[97] S. Kuhr, W. Alt, D. Schrader, I. Dotsenko, Y. Miroshnychenko, A. Rauschenbeutel, and D. Meschede. Analysis of dephasing mechanisms in a standing-wave dipole trap. *Phys. Rev. A* **72**, 023406 (2005).

[98] T. Wilk, S. C. Webster, A. Kuhn, and G. Rempe. Single-atom single-photon quantum interface. *Science* **317**, 488–490 (2007).

[99] C. Simon and W. T. M. Irvine. Robust long-distance entanglement and a loophole-free Bell test with ions and photons. *Phys. Rev. Lett.* **91**, 110405 (2003).

[100] S. Bose, P. L. Knight, M. B. Plenio, and V. Vedral. Proposal for Teleportation of an Atomic State Via Cavity Decay. *Phys. Rev. Lett.* **83**, 5158–5161 (1999).

[101] T. Pellizzari, S. A. Gardiner, J. I. Cirac, and P. Zoller. Decoherence, Continuous Observation, and Quantum Computing: A Cavity QED Model. *Phys. Rev. Lett.* **75**, 3788–3791 (1995).

[102] Y. Miroshnychenko, W. Alt, I. Dotsenko, L. Förster, M. Khudaverdyan, D. Meschede, D. Schrader, and A. Rauschenbeutel. An atom-sorting machine. *Nature* **442**, 151 (2006).

Publications

- B. Weber, H.P. Specht, T. Müller, J. Bochmann, M. Mücke, D.L. Moehring and G. Rempe.
  Entanglement distribution between a trapped atom and two photons.
  in preparation.

- J. Bochmann, M. Mücke, G. Langfahl-Klabes, C. Erbel, B. Weber, H.P. Specht, D.L. Moehring and G. Rempe.
  Fast excitation and photon emission of a single-atom-cavity system.
  accepted for publication in Physical Review Letters.

- M. Hijlkema, B. Weber, H.P. Specht, S.C. Webster, A. Kuhn and G. Rempe.
  A single-photon server with just one atom.
  Nature Physics **3** 253-255 (2007).

- K. Murr, S. Nußmann, T. Puppe, M. Hijlkema, B. Weber, S.C. Webster, A. Kuhn, and G. Rempe.
  Three-dimensional cavity cooling and trapping in an optical lattice.
  Phys. Rev. A, **73**, 063415 (2006).

- S. Nußmann, K. Murr, M. Hijlkema, B. Weber, A. Kuhn and G. Rempe,
  Vacuum-stimulated cooling of single atoms in three dimensions.
  Nature Physics **1**, 122-125 (2005).

- S. Nußmann, M. Hijlkema, B. Weber, F. Rohde , G. Rempe and A. Kuhn.
  Submicron Positioning of single atoms in a microcavity.
  Physical Review Letters, **95**, 173602 (2005).

Acknowledgements

The new achievements with the experiment presented in this thesis are the result of good teamwork and many people's contribution of brilliant ideas. I want to take the opportunity to thank all those who helped on the realization of this thesis. I first want to say that I definitely enjoyed working with all of you. Each of you had his own contribution to the experiment, so I would like to thank:

- *Gerhard Rempe* for the opportunity to work on the realization of this project and for making me curious about quantum optics in one of his lectures at the university.
- My former colleagues. *Axel Kuhn* always had good ideas whenever we had none. *Stefan Nußmann* set up the experiment. We still benefit from his careful planning. *Markus Hijlkema* developed the imaging system. Now we can see the atoms at work. *Felix Rohde* built and characterized the cavity. We still believe, the dust particle we found on the mirror was not his fault. *Tobias Müller* set up the new detectors and took the first single-atom pictures with me. *Tatjana Wilk* set the benchmark for my measurements with her pioneering work.
- My current co-workers. I really enjoyed *David Moehring's* companionship during the long measurements. The results would not be the same without his good ideas. *Holger Specht* was my partner in the lab during the long time we prepared and performed the entanglement measurements. As an expert on the field, he was always the man in charge when the cavity lock had to be optimized again. It is also on his account that you will probably find more cameras in our lab than in a typical TV studio, but I must admit, it helped. *Jörg Bochmann* and *Martin Mücke* set up a new apparatus which already produced very nice data. I always enjoyed seeing it grow and to be able to contribute from time to time. *Karim Murr* was responsible for theoretical background of the experiments and the distribution of good vibrations.
- All current and former colleagues in the Rempe group. I always enjoyed the collegiality concerning the daily problems at the institute and all the common activities at Ringberg, Rechtegg and on Barbecues and Skiing-days. I want to specially mention *Peter Maunz* for his patience with the adaptation of Maestro to the requirements of our experiment.
- The technicians. Without their work the experiment simply would not exist. While *Joseph Bayerl* planned and designed all the complex things, *Franz Denk* and *Helmuth Stehbeck* were always at hand for spontaneous, but nevertheless perfect solutions. *Tom Wiesmeier* is responsible for numerous electronic devices in our laboratory and rescued the experiment from an invasive electromagnetic attack by the neighbor experiment.

I thank *David*, *Holger*, *Jörg* and my wife *Melanie* for all the valuable input and for proofreading this thesis.